MAGLAB REPORTS

THE 2014 HIGHLIGHTS ISSUE

Discover the lab's 58 best research reports from the year.

GLOBAL USERS

See where our 1,442 users came from.

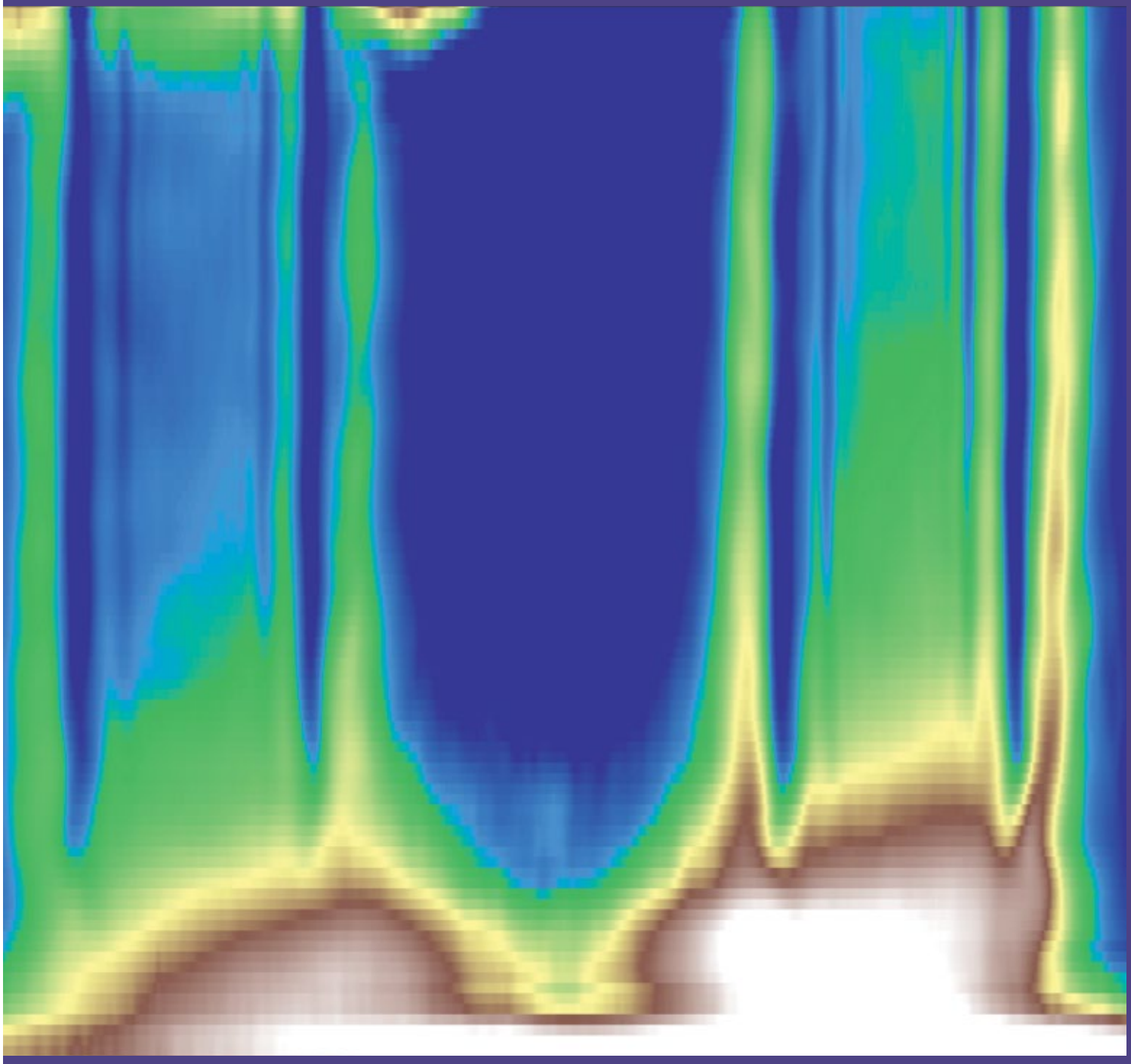

Volume 22 No. 2 • Summer 2015

CONTENTS

IN EVERY ISSUE

RESEARCH

ON THE COVER

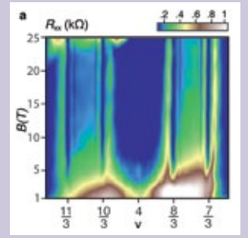

Several fractional quantum Hall states in mono- and bilayer graphene have been observed for the first time.

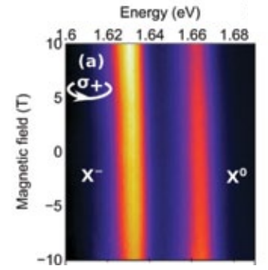

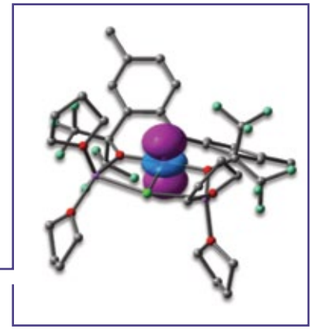

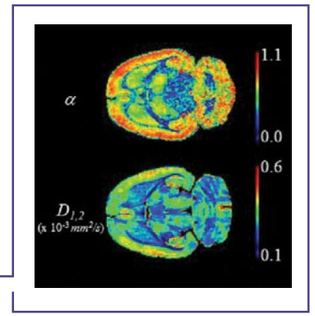

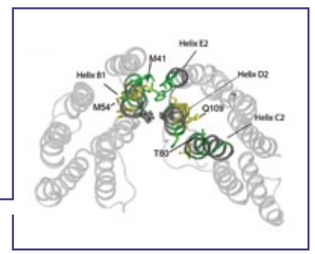

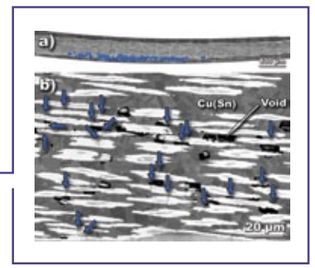

DIRECTOR'S DESK

Twenty years after launching our user program, the National MagLab continues to offer new instruments and experimental techniques for users to produce high magnetic field research results that further our understanding of materials, energy and life.

In 2014, the National MagLab continued to grow our user community, hosting more than 1,440 researchers from over 276 universities, institutions and businesses around the world (page 68 illustrates the directions and distances traveled by our users). MagLab users are both new and diverse with nearly 23 percent of 2014's users self-identifying as women (5 percent chose not to identify) or minorities (9.5 percent chose not to identify) and a quarter of the 368 principal investigators (PI) being first-time-ever PIs for National MagLab experiments.

Perhaps the best measure of the quality of the research performed at the National MagLab is in the 450 articles published in peer-reviewed journals in 2014, many in the scientific community's most prestigious journals like *Nature, Science, Physical Review Letters, Analytical Chemistry, Energy Fuels,* and *The Proceedings of the National Academy of Sciences.* To see a full list of our publications, visit **NationalMagLab.org/research/publications-all/publications-search.**

Each user who conducts research at our lab submits a research report. The 452 reports from 2014 span the breadth of research performed at our interdisciplinary laboratory. The results from 20 percent of these reports are already published, another 11 percent have generated manuscripts that are submitted or accepted for publication, and another 46 percent have manuscripts in preparation.

The 58 highlights featured in this issue represent some of the most exciting research, selected by the MagLab's Science Council and myself. They feature the diverse capabilities of our magnets, techniques, and instrumentation and showcase the power of high magnetic field research in condensed matter physics, materials science, chemistry, magnet science and technology, and the life sciences.

Research at the National MagLab is supported primarily by the U.S. National Science Foundation, the State of Florida and the U.S. Department of Energy. The U.S. National Institutes of Health, U.S. Department of Defense, U.S. Air Force Office of Scientific Research, U.S. Army, U.S. Navy and numerous universities across the country and around the world also funded research performed at the lab this past year.

The MagLab itself continues to invest in scientific partnerships between in-house scientists and users to advance science and introduce new experimental techniques into the user program through the User Collaboration Grants Program. This year, 41 of the year's research reports were supported by this effort, as were 5 of the highlights presented here.

With this highlights issue completed, Year 2 of our current grant is now officially "in the books." If you are interested in learning more about this past year's successes, take a look at our Year In Review at **NationalMagLab.org/about/print-media/at-a-glance.**

The National MagLab is looking to the future to develop our 2018-2022 renewal proposal. We look forward to working with our External Advisory Committee, our User Advisory Committee and our entire user community to articulate a shared vision for high magnetic field science in the coming years.

MAGLAB REPORTS

Volume 22 No. 2 • Summer 2015

PUBLISHED BY
The National High Magnetic Field Laboratory
1800 East Paul Dirac Drive
Tallahassee, FL 32310-3706

PHONE NUMBER
(850) 644-0311

LAB DIRECTOR
Gregory Boebinger

EDITOR
Kristin Roberts

GRAPHIC DESIGNER
Caroline McNiel

This document is available in alternate formats upon request. Contact Public Affairs for assistance. If you'd like to be added to our mailing list, please visit:
NationalMagLab.org/about/print-media

The MagLab is supported by the National Science Foundation (DMR – 1157490) and the State of Florida.

@NationalMagLab

NationalMagLab.org

Condensed Matter Science

Photos by: Dave Barfield

CM Technique Development

Measuring the critical current of REBCO coated conductors at high magnetic fields is vital for both applications, such as the NHMFL 32 T superconducting magnet project as well as for understanding the physics of pinning so as to engineering a commercial production process. Recent 4 mm wide conductors achieve huge critical current in excess of 4 kA at low temperature.

To avoid problems with high current measurements at cryogenic temperatures, in the limited diameter of a magnet bore, the authors have developed a contact-less method based upon usual vibrating sample magnetization measurements. The novelty of the design is that to facilitate in situ sample rotation the coil not the sample is vibrated facilitating angle dependent measurements in resistive magnets up to 31 T.

Vibrating Coil Magnetometer for REBCO Coated Conductor Characterization

Constantinescu, A.M.; Jaroszynski, J.; Hu, X.; Santos, M. (NHMFL)

Introduction

The recent progress in (RE)$Ba_2Cu_3O_{7-x}$ (RE = rare earth) coated conductors resulted in superior high critical currents achieving > 4 kA in 4 mm wide tapes. This high supercurrent and its anisotropy are very difficult to measure in high magnetic fields due to space and cooling limitations. REBCO conductor characterization is needed for such applications as NHMFL 32 T magnet project, understanding the physics of pinning, and improvement of the commercial production process. To avoid problems with high currents, we develop a contactless method based on vibrating sample magnetization (VSM) measurement.

Experimental

We successfully tested a new version of the device. We rebuilt the VSM to be a VCM (vibrating *coils* magnetometer) shown in **Figure 1a**. That makes it possible to rotate the sample *in situ*, and determine temperature and angle with higher accuracy. The cryogenic piezoelectric actuator drives the device. The noise remains at a low level and measurements are possible in resistive magnet up to 31 T in cell 7.

Conclusions

As **Fig. 1c** shows, there is a good correspondence between results achieved by means of magnetization and the usual transport method. That proves the method as a useful tool for the REBCO conductor. It can be also used for other magnetization experiments.

Acknowledgements

This work was performed as UCGP project at the National High Magnetic Field Laboratory, which is supported by National Science Foundation Cooperative Agreement No. DMR-1157490, the State of Florida, and the U.S. Department of Energy.

Figure 1

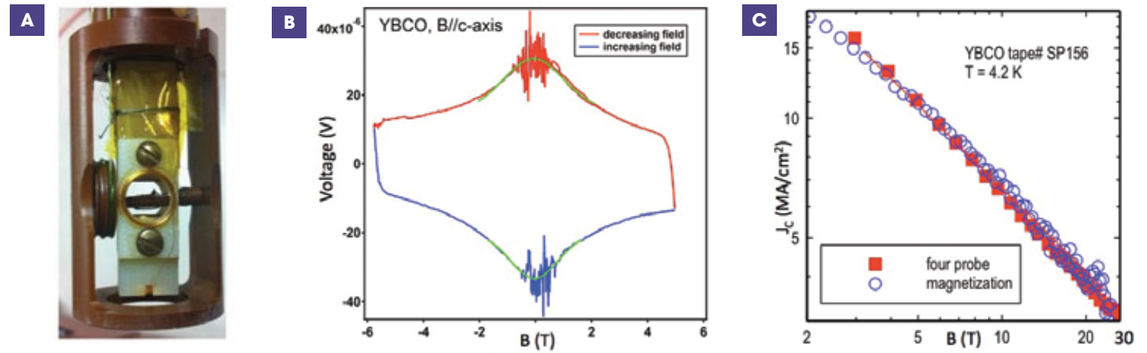

(A) Photograph of vibrating coils magnetometer.
(B) Magnetization loop in YBCO conductor.
(C) Comparison of critical current results obtained by magnetization and four probe measurements.

CM Technique Development

Cantilever magnetometers have sensitivities rivaling commercial SQUID magnetometers, which combined with their fast response (~100kHz) makes them particularly suitable for pulsed and DC magnetic field measurements. The torque response to magnetic anisotropy requires that samples are precisely aligned with both the bending mode of the cantilever and the applied magnetic field. In transient magnetic fields small samples (~10s μm) are required so as not to overly slow the mechanical response of the cantilever. Furthermore, when the magnetic anisotropy of a sample is very large, the torque generated by the sample has the potential to the break the lever. To address both these issues the authors have used Focused Ion Beam lithography to cut and attach oriented single crystals for pulsed field magnetometry studies of highly anisotropic materials: the susceptibility of Li_2IrO_3 has greater than an order of magnitude anisotropy at low temperature.

Focused Ion Beam Lithography for Torque Magnetometry Measurements

Modic, K. (NHMFL); Ramshaw, B.; Maiorov, B.; Shehkter, A. (NHMFL); Analytis, J. (UC Berkeley); McDonald, R. (NHMFL)

Introduction

The focused ion beam (FIB), commonly used in the semiconductor industry for imaging, deposition, and ablation of materials, can also be used for precision cutting. Recently, FIB was used to significantly reduce the size of a single crystal for cantilever torque magnetometry measurements. Sensitivities of a fraction of a picoNewton-meter can be achieved in the pulsed field magnet, which has a 10 ms rise time. This corresponds to a sensitivity of 10^9 spins at a field of 60 T, rivaling the sensitivity of commercial SQUID magnetometers, which cannot be used in pulsed magnetic fields. However, when the magnetic anisotropy of a sample is very large, the torque generated by the sample often has the potential to the break the lever during a magnetic field pulse.

Experimental

Li_2IrO_3 experiences an order of magnitude anisotropy with field orientation at low temperature resulting in a very large torque signal. All previous attempts to complete an angular dependence of torque measurements on the smallest Li_2IrO_3 single crystals available have resulted in broken levers. The FIB was utilized to remove the top 10 microns of the sample **(Figure 1)**, mount it on the cantilever, and deposit platinum to hold the crystal in place. A complete angular dependence of the magnetic torque of Li_2IrO_3 was successfully completed in the 65 tesla pulsed field magnet **(Figure 2).**

Acknowledgements

This work was performed at the National High Magnetic Field Laboratory, which is supported by National Science Foundation Cooperative Agreement No. DMR-1157490, the State of Florida, and the U.S. Department of Energy.

References

1. Modic, K.A., et al., Nat Commun, **5**: 4203, 2014. Doi:10.1038/ncomms5203

Figures

1

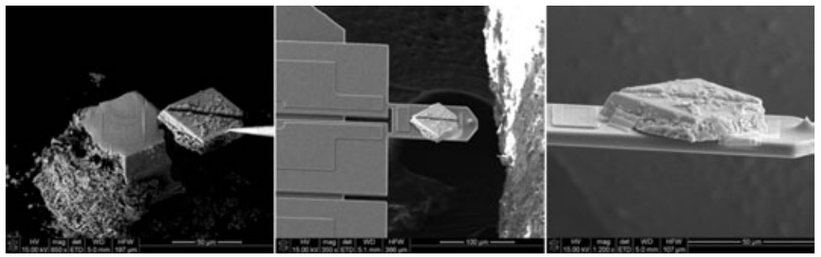

Left panel: small(~40μm³) single crystal of Li_2IrO_3 with a thin slice cut from the top surface using the FIB. Middle panel: crystal mounted on the cantilever. Right panel: close-up of the crystal on the cantilever with Pt deposited on the edges to hold the crystal in place.

2

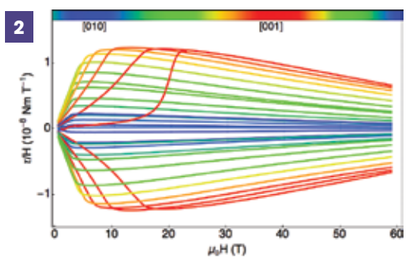

Magnetic torque τ of Li2IrO3 divided by magnetic field H at 1.75K. The colored curves correspond to rotation of the crystal in the b-c plane with respect to the applied magnetic field.

CM Technique Development

The authors present a very nice development for the 25 T split that will allow users to study spin depend-ent phenomena using ultrafast optics. This will impact research in many areas that deal with quantum computing and could be used to highlight one of the science drivers for the recompetition.

Fluorescence Line Narrowing (FLN) Experiments Revisited in the Florida Helix

Rawat, N.; K. N. Hua.; Furis, M. (University of Vermont, Materials Science); Bishop, M.; Semenov, D.; McGill, S. (NHMFL-FSU)

Introduction

The recently commissioned HELIX magnet and its split-coil design represent not only a premiere in magnet technology but also an unprecedented opportunity to fully implement the latest ultrafast techniques into the high magnetic field environment towards new discoveries of spin-dependent phenomena in large variety of systems. We revisited Fluorescence Line Narrowing (FLN) in CdSe nanocrystals, a system where the interplay between bright and dark exciton states and exciton spin dynamics [1,2] can now be studied on the sub-nanosecond scale with the new free-space optics setup and the tunable ultrafast OPERA Solo parametric amplifier.

Experimental

In an FLN experiment a narrowband laser is carefully tuned to a wavelength resonant to the tail of the ensemble absorption spectrum in order to create excitons only in the largest nanocrystals within the ensemble, thus effectively probing only a subset of nanocrystals sizes. The narrowband ultrafast excitation (~ 1nm) is now obtained from the 30nm broadband output of the 1KHz Coherent OPERA Solo parametric amplifier using a grating and slit setup.

Results and Discussion

Figure 1 (a) shows some of our representative PL spectra and lifetimes. We clearly observe the expected narrow luminescence spectra from different nanocrystals sizes within an ensemble. We also observe a significant amount of polarization that varies as a function of size in agreement with previous CW luminescence experiments performed in the resistive magnets.[3] The T = 15 K long recombination lifetimes are also in agreement with previous measurements. The big news in this experiment is that we can now resolve the fast spin-dependent dynamics component of the decay. (Inset of Fig 1(b)) There are unanswered questions in the fast component of spin-dependent exciton dynamics in virtually every electronic material because of the limitations imposed by fibers experiments. All of those questions can now be answered using state of the art polarization optics and picosecond electronics.

Acknowledgements

This work was supported by NSF DMR # 1229217 and the NHMFL Visiting Scientist program. A portion of this work was performed at the National High Magnetic Field Laboratory, which is supported by National Science Foundation Cooperative Agreement No. DMR-1157490, the State of Florida, and the U.S. Department of Energy.

References

1. M. Furis et al, Phys. Rev. B **2006**, 73, 241313.
2. M. Furis et al. Phys. Rev B **2008**, 77, 035328.
3. M. Furis et al, *J. Phys. Chem.* B **2005,** 109, 15332-15338.

Figure 1

A

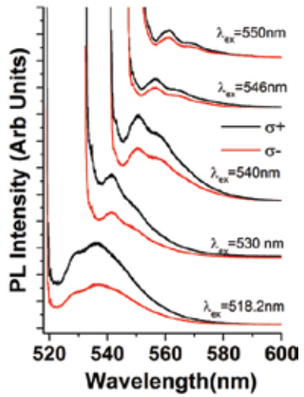

B

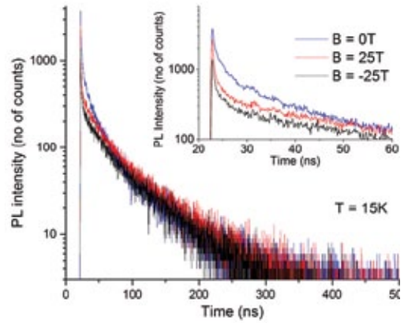

(A) Spin-resolved FLN spectra from five different CdSe nanocrystal sizes within two different ensembles exhibit the expected amount of spin-polarization at B = 25T and T = 15K **(B)** The sub-nanosecond fast component of exciton spin dynamics (inset) is now revealed for the first time in the HELIX free space optics experiments

CM Technique Development

The authors report a proof-of-principle X-ray capability for cryogenic studies in magnetic fields of 25 T using the split magnet. This will allow for simple structural studies of materials, but one can envision future studies on single crystals, polycrystals and powders.

X-ray Diffractometer for the Florida Split Coil 25 T Magnet

Wang S.; Kovalev A.; Suslov A. (FSU; NHMFL); Siegrist T. (FSU; NHMFL, Chemical & Biomedical Engineering)

Introduction

We designed, built, and tested a small proof-of-concept X-ray diffractometer for the 25 T Florida Split Helix Magnet [1], with measurement capability at cryogenic temperatures. This setup provides unique opportunities to perform X-ray diffraction studies in DC magnetic fields in excess of 20 T, thus, positioning NHMFL as the only place in the world to perform this kind of studies.

Experimental Results

The diffractometer as previously described in Ref. [2] was developed further and its performance was improved. Tests on standard samples, specifically LaB_6 and Si powders **(see Fig.1)**, were carried out to prove operation of the diffractometer in high magnetic fields. Low temperature measurements were performed in a custom-designed cryostat (Janis Research Co,[3]) incorporated with the magnet, in the temperature range of 15-295 K. Samples were mounted on a cold finger of a home-made probe that could be rotated about its z-axis for sample alignment and θ-2θ measurements. In addition to the image plate, a pixel array detector (Dectris Pilatus) was also successfully tested. Initial investigations using the diffractometer and high fields were carried out on: Terfenol-D [4] **(see Fig.2)**; Invar [5]; MP35N alloy; austenitic stainless steel 301**(see Fig.3)**; and iron-based superconductor crystal $Fe_{1.12}Te$.

Conclusions

We have shown the feasibility of X-ray diffraction in high DC fields in excess of 20 T, using the Florida Split Helix magnet. So far, experiments are time consuming using the image plate detector and a sealed tube source. At present, the X-ray diffractometer is unsuitable for full deployment in the user program due to extensive data acquisition times. However, simple experiments are possible, where data acquisition times are of the order of 10s of minutes, such as the confirmation of a material' s structural changes resulting from variations of temperature and/or magnetic field.

Acknowledgements

This project is supported by NSF-EAGER grant DMR-1257649. Authors are thankful to Dr. I. Zaliznyak for providing the $Fe_{1.12}Te$ sample, and to Dr. K. Han for supplying samples of MP35N and stainless steel 301.

References

1. http://www.magnet.fsu.edu/usershub/scientificdivisions/dc-field/cell5/index.html
2. Wang, S., *et al.*, NHMFL Annual Report, 395 (2013)
3. http://www.janis.com
4. http://www.etrema-usa.com/documents/Terfenol.pdf
5. http://www.goodfellowusa.com

Figures

1

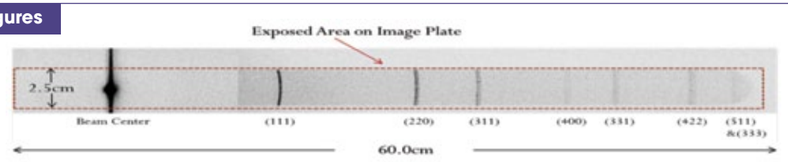

Indexed diffraction pattern from a Si powder sample (image plate).

2

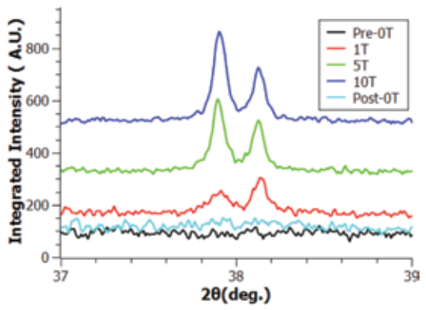

The (533) and (622) reflections appear in magnetic fields of 1, 5 and 10 T, in Terfenol-D at room temperature. Data acquisition was 60 min for each field.

3

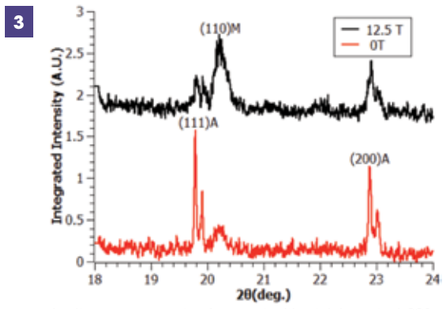

In-situ measurements of an austenitic stainless steel 301 sample at room temperature using the Dectris PILATUS 100 K-S detector. Data acquisition was 9 min for each field.

Graphene

The Kim Group observe a range of FQHE phases in bilayer graphene fabricated with top and bottom gates, so as to be tunable with both magnetic and electric fields. The gate electric field and magnetic field is shown to drive transitions between different spin and valley orderings in bi layer graphene including different FQHE phases. This enables the study of phase transi-tions between different topologically ordered states.

Published in *Science*, **345**, 61-64 (2014).

Tunable Fractional Quantum Hall Phases in Bilayer Graphene

Maher, P.; Forsythe, C.; Kim, P. (Columbia U., Physics); Gao, Y.; Hone, J. (Columbia U., Mechanical Engineering); Wang, L. (Columbia U., Electrical Engineering); Taniguchi, T.; Watanabe, K. (National Institute for Materials Science); Dean, C.R. (City College of New York, Physics); Abanin, D.; Papic, Z. (Institute for quantum computing); Cadden-Zimansky, P. (Bard College, Physics)

Introduction

Under strong magnetic fields, a two dimensional electron gas can form correlated many-body states via strong Coulomb interactions, giving rise to the fractional quantum Hall effect (FQHE). In addition to electron spin, the existence of a valley degree of freedom in graphene allows the formation of FQHE states within an SU(4) symmetry space. In bilayer graphene (BLG), the gate electric field and magnetic field can drive transitions between different spin and valley orderings including different FQHE phases, making it an ideal system to study phase transitions between different topologically ordered states.

Using the recently developed van der Waals transfer technique, we fabricated high quality BLG devices encapsulated in hexagonal boron nitride. We demonstrated different FQHE phases in the device tunable with magnetic and electric field.

Experimental

Dual-gated bilayer graphene devices encapsulated in hexagonal boron nitride were measured in the 31 tesla resistive magnet in cell 9 at the NHMFL in a sample-in-vapor He^3 refrigerator.

Results and Discussion

Fig. 1A shows longitudinal conductance as a function of top and bottom gate voltages at B = 14 T and T = 1.8 K. All broken-symmetry integer states are visible (multiple of 4 filling factors are marked with white dashed lines), indicative of high device quality.

Fig. 1B shows longitudinal conductance as a function of filling factor (in the range of $1.2 < \nu < 1.8$) and displacement field (in the range of $-50 < D < 50$ mV/nm) at 300 mK for three different magnetic fields. Different FQHE phases have been clearly demonstrated, which are tunable with magnetic and displacement field.

Acknowledgements

A portion of this work was performed at the National High Magnetic Field Laboratory, which is supported by US National Science Foundation cooperative agreement no. DMR-1157490,the State of Florida and the US Department of Energy. This work is supported by AFOSR MURI. P.K. acknowledge sole support from the US Department of Energy (DE-FG02-05ER46215).

References

1. D. C. Tsui *et al.*, Phys. Rev. Lett. **48,** 1559–1562 (1982).
2. P. Maher *et al.*, Science, **345**, 61-64 (2014).

Figure 1

A

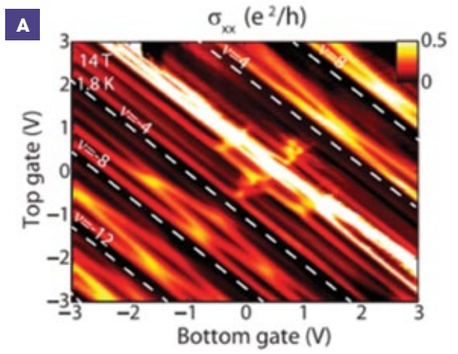

B

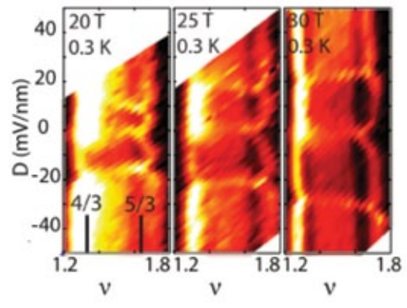

Graphene

This report describes the first observation of several fractional quantum Hall (FQH) states states in mono- and bilayer graphene, made possible by the combination of low-disorder devices and high magnetic fields. The nature of FQH states was probed by temperature and field-dependent studies.

Fractional Quantum Hall Effect in Monolayer Graphene

Amet, F. (Stanford); Bestwick, A. (Stanford); Diankov, G. (Stanford); Williams J.R. (U Maryland); Taniguchi, T. (NIMS, Japan); Watanabe, K. (NIMS, Japan); Goldhaber-Gordon, D. (Stanford)

Introduction

In a large magnetic field the kinetic energy of two-dimensional electrons becomes quantized as a discrete set of highly degenerate Landau levels. In a partially filled Landau level, electron interactions determine the ground state and yield new incompressible phases known as fractional quantum Hall (FQH) states.

In graphene, FQH states are characterized by their spin and valley internal degrees of freedom **[1]**. Phase transitions **[2]** between ground states of different polarizations result from the competition between electron repulsion, Zeeman splitting, and interactions with the boron nitride substrate.

The observation of this rich phase diagram in transport has so far been limited to the most robust FQH states due to their extreme sensitivity to disorder. However a larger set of FQH states are now within reach thanks to progress in the fabrication and design of graphene/boron nitride heterostructures, combined with the high fields available at the NHMFL.

Experimental

Monolayer and bilayer graphene multiterminal devices with graphite back gates were measured in ^{3}He cryostats in cells 9, 12 and 15 at magnetic fields up to 45 T.

Results and Discussion

Figure 1a shows the filling factor and field dependence of the longitudinal resistance Rxx(ν,B) in the first Landau level of monolayer graphene. Between each integer filling factor, vanishing Rxx indicates fractional quantum Hall states when ν follows the sequence ν=p/2p+1 , with p an integer, as predicted by composite fermion theory. At only 14T, delicate states such as 17/7 and 18/7 are already well defined **[Fig. 1b].** The activated temperature dependence of Rxx was used to determine fractional quantum Hall gaps at each filling factor and as a function of the magnetic field **[3]**.

Interactions with the boron nitride substrate break the sublattice symmetry in some graphene flakes, which opens an energy gap at zero field [4,5]. In the zeroth Landau level, this results in our observation of FQH states at ν=-5/3 and -7/5. Such states are stabilized by the broken valley symmetry, which prevents low-lying valley-textured excitations from destroying odd numerator fractions between ν=-2 and -1.

In the first Landau level, we observe robust fractional quantum Hall states, many of which disappear in a strong in-plane field **[Fig. 1c]**. This suggests these states are not yet spin-polarized in that level, rather surprising given the already large Zeeman splitting.

Conclusions

We have observed FQH states in high quality graphene devices on boron nitride with a graphite back gate. These follow the two-flux composite fermion sequence up to denominator 11, with unexpected patterns of stability and spin polarization.

Acknowledgments

A portion of this work was performed at the National High Magnetic Field Laboratory, which is supported by National Science Foundation Cooperative Agreement No. DMR-1157490, the State of Florida, and the U.S. Department of Energy. In addition, this work was funded by the Center for Probing the Nanoscale, an NSF NSEC, under grant No. PHY-0830228 and by Office of Naval Research Graphene MURI, topic # 9.

References

1. Dean, C. R. *et al.* Nature Phys. **7**, 693–696 (2011).
2. Feldman, B. *et al.* PRL **111**, 076802 (2013).
3. Amet, F. *et al.* Nature Comm. **6**, 5838 (2015).
4. Hunt, B., *et al.* Science, **340,** 1427-1430 (2013).
5. Amet, F. *et al.* PRL **110**, 216601 (2013).

Figure 1

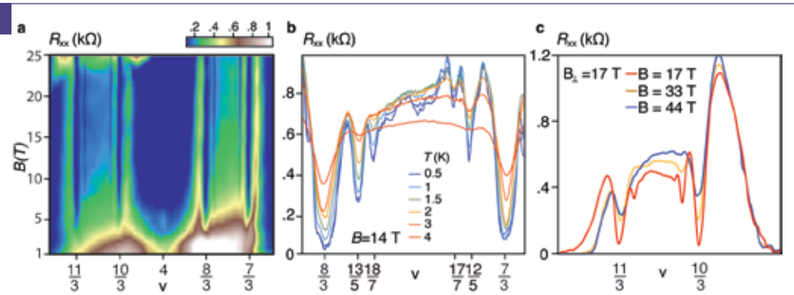

A. R_{xx} (ν, B) measured at 300mK around half filling in 1LL. Vertical blue stripes indicate incompressible phases. **B.** Temperature dependence of R_{xx} between ν=2 and ν=3, measured at 14T. Activated behavior indicates the emergence of Fractional Quantum Hall gaps. **C.** In-plane field-dependence of fractions between ν= 3 and ν = 4, the out-of-plane field is held constant at 17 T.

Graphene

This report describes capacitance measurements in dual-gated bilayer graphene devices, which allow for the first time a direct probe of the layer degree of freedom, in particular the density of states and the charge distribution on the two layers. Tuning of the top and bottom gates in fixed magnetic fields up to 18 T reveals a checkerboardlike pattern in the layer polarization (charge imbalance between the layers) and the lifting of the orbital degeneracy in the lowest Landau level. Measurements in higher magnetic fields will be important to understand the nature of these broken-symmetry states.

Direct Measurement of the Layer Polarization of Bilayer Graphene

Young, A.F. (MIT, Physics); Hunt, B. (MIT, Physics); Wang, L. (Columbia, Physics), Hone, J. (Columbia, Mech. Eng.); Dean, C.R. (Columbia, Physics); Ashoori, R.C. (MIT, Physics)

Introduction

The lowest Landau level of bilayer graphene (BLG) is a rich platform for investigating the physics of interacting electrons because each electron carries *three* separate spin-1/2-like degrees of freedom - real spin, layer isospin, and orbital isospin - and thus there are many possibilities for ground-state ordering in this eight-dimensional space when interactions lift this degeneracy. Moreover, the relative importance of these degrees of freedom can be tuned with electric and magnetic fields, as has been shown in several new papers that have taken advantage of unprecedentedly high sample quality of bilayer graphene [1,2,3]. There are several ways to probe the spin degree of freedom, such as tilted-field magnetotransport [4], but a *direct* probe of the layer degree of freedom has so far been absent.

Experimental

We employ capacitance measurements of a bilayer graphene sample with both a top gate and a bottom gate, allowing us to tune both the displacement field and the density, as well as enabling measurement of the capacitance of the bilayer to the top gate and to the bottom gate, C_T and C_B; this is crucial, in BLG capacitance measurements can probe not just the density of states but also the distribution of electrons on the two layers that comprise the bilayer, a direct measurement of the layer-isospin texture of these interacting ground states. We used these capacitance techniques in SCM-1 at 18T and millikelvin temperatures.

Results and Discussion

Our results are shown in Fig. 1. The top, checkboard pattern is a measurement of C_T-C_B, which is proportional to the layer polarization $\partial(n_T\text{-}n_B)/\partial(\mu_T+\mu_B)$ in our device. In Fig. 1, at bottom, is a measurement of the density of states at 18T in which we begin to glimpse the lifting of the orbital degeneracy, a feature only recently observed in BLG (Ref. [1] and [2]). Phase transitions at different displacement fields, marked by closing of the gaps are accompanied by diagonal features in the layer polarization map (Fig. 1 top) whose origin is currently not understood.

Conclusions

We plan to measure capacitance of BLG in higher fields at the NHMFL, where we expect to be able to resolve the electron states associated with the lifting of the orbital degeneracy and study their layer distribution in these newly-discovered broken-symmetry states.

Acknowledgements

A portion of this work was performed at the National High Magnetic Field Laboratory, which is supported by National Science Foundation Cooperative Agreement No. DMR-1157490, the State of Florida, and the U.S. Department of Energy.

We acknowledge support from the Gordon and Betty Moore Foundation, the Department of Energy under award DE-FG02-08ER46514, and the National Science Foundation under award 1351337.

References

1. Lee et al. Science **345**, 58 (2014)
2. Maher et al. Science **345,** 61 (2014)
3. Kou et al. Science **345**, 55 (2014)
4. Maher et al., Nature Physics **9**, 154 (2013)

Figure 1

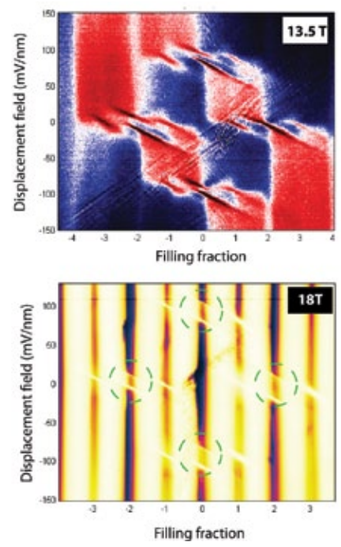

Layer polarization of the lowest Landau level (LLL) of bilayer graphene. Red: charge added to top layer; blue: charge added to bottom layer.

Top gate capacitance measurement of a similar device in SCM-1. The green circles mark the appearance of the lifting of the orbital degeneracy in the LLL. Color scale: dark, incompressible states (gaps) between Landau levels; light, compressible Landau levels (high density of states).

Graphene

The Dean group report magnetoresistance measurements of graphene–boron nitride hetrostructures, which address the fundamental question of whether composite fermion theory applies to fractionally filled Hofstadter bands.

The lattice mismatch between graphene and boron nitride forms a moiré pattern that provides a periodic potential with a length scale comparable to the magnetic length at high magnetic fields. For a single particle description, this is known to give rise to the recursive Hofstader spectrum of Landau levels. This work demonstrates that Hofstadter bands can support fractional quantum Hall states, but that they evolve in magnetic field in a unconventional way due to interplay with the Hofstadter mini-gaps. Surprising new QHE features are also observed, corresponding to fractional Bloch band index, but with integer Hall plateaus.

Hofstadter Butterfly in the Strongly Interacting Regime

Wang, L.; Gao, Y.; Han, Z.; Wen, B.; Hunt, B.; Shih, E.-M.; Hone, J. (Columbia U., Mechanical Engineering); Taniguchi, T.; Watanabe, K. (National Institute for Materials Science); Dean, C.R. (Columbia U., Physics)

Introduction

The moiré pattern that develops in graphene/BN heterostructures act as a periodic potential, providing a nearly ideal system to study the effect of superlattice patterning on 2D systems. Under large magnetic fields, interplay between the moiré and magnetic length scales gives rise to a self-similar recursive energy spectrum, known as Hofstadter's butterfly. The Hofstadter spectrum arises in a purely single particle picture, and in fact the role of electron-interactions has received only limited theoretical attention. For example it remains unclear whether fractionally filled Hofstadter bands will support FQHE states. Does the composite Fermion (CF) picture continue to hold and if so do the CF states also exhibit fractal structure? The possibility of anomalous orbital magnetism under certain conditions has been theorized.

Experimental

Very high mobility monolayer and bilayer graphene/hexagonal boron nitride heterostructure samples were measured utilizing a combination of the SC magnet facilities for fields ranging between 0-18T, and the resistive magnet facilities at fields up to 45 T.

Results and Discussion

We report measurement of the Hofstadter butterfly in ultra-high mobility graphene superlattices in the high magnetic field regime **(Figure 1).** A complete discussion of our results can be found in Ref. [2].

Acknowledgements

A portion of this work was performed at the National High Magnetic Field Laboratory, which is supported by National Science Foundation Cooperative Agreement No. DMR-1157490, the State of Florida, and the U.S. Department of Energy. C.R.D was supported by the US National Science Foundation under grant no. DMR-1462383.

References

1. Dean et al., "Hofstadter's Butterfly and the fractal quantum Hall effect in Moiré superlattices " Nature, **497**, 598 (2013).
2. Wang et al, "Fractional fractal quantum Hall effect in graphene superlattices", arXiv:1505.07180 (2015)

Figure 1

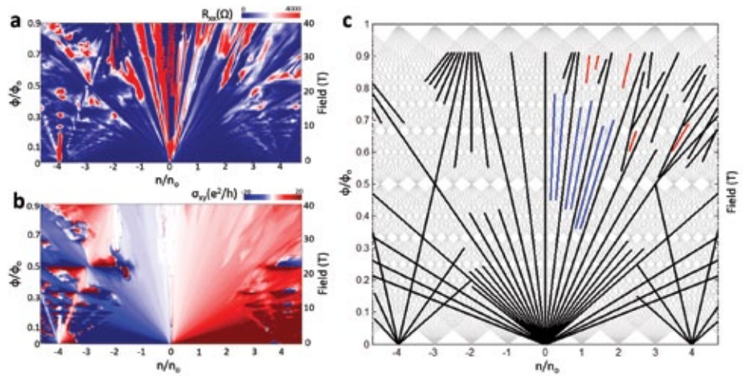

(A) and **(B)** show a plot of longitudinal resistivity and transverse Hall resistivity, respectively, as a function of normalized carrier density and normalized flux. A summary of the observed states is plotted in the simplified Wannier diagram, shown in **(C).** The exceptional device exhibits clear signatures of interaction-driven integer symmetry broken states within the conventional QHE hierarchy and within the Hofstadter mini-fans (black lines). Simultaneously, we observe signatures of the fractional quantum Hall effect at filling fractions 1/3, 2/3, 4/3, 5/3, 7/3 and 8/3 (blue lines). As the magnetic field is increased above 30 Tesla, the FQHE states give way to mini-band states associated with the Hofstadter spectrum, in agreement with recent theoretical predictions. Finally, at under large magnetic fields we observe a series of new features characterized by integer Hall quantization but corresponding to fractional Bloch band index. These fractional Bloch band QHE states are not anticipated by existing theoretical pictures and may point towards a new type of many body state[2].

Graphene

This report describes capacitance measurements in dual-gated bilayer graphene devices, which allow for the first time a direct probe of the layer degree of freedom, in particular the density of states and the charge distribution on the two layers. Tuning of the top and bottom gates in fixed magnetic fields up to 18 T reveals a checkerboardlike pattern in the layer polarization (charge imbalance between the layers) and the lifting of the orbital degeneracy in the lowest Landau level. Measurements in higher magnetic fields will be important to understand the nature of these broken-symmetry states.

Competition Between Spontaneous Symmetry Breaking & Single Particle Gaps in Trilayer Graphene

Lee, Y.; Tran, D.; Myhro, K.; Velasco Jr., J.; Gillgren, N.; Barlas, Y.; Lau, C.N. (UC Riverside Physics); Poumirol, J.M.; Smirnov, D. (NHMFL); Guinea, F. (CSIC Spain)

Introduction

Many physical phenomena can be understood by single particle physics, i.e. treating particles as non-interacting entities. When this fails, many-body interactions leads to spontaneous symmetry breaking and phenomena such as fundamental particles' mass generation, superconductivity and magnetism. Competition between single-particle and many-body physics leads to rich phase diagrams. Trilayer graphene (TLG) offers an exciting platform for study of such interplay, as the relative magnitudes of single particle effect and electronic interactions can be tuned by external parameters such as density, electric field and magnetic fields.

Experimental Results and Discussion

Using low temperature transport measurements, we investigate high mobility dual-gated ABC TLG devices. At the charge neutrality point, we observe a giant interaction-induced gap Δ~41meV, suggesting a spontaneous layer antiferromagnetic ground state with broken time reversal symmetry. This state is suppressed by a critical temperature T_c~35K, by an in-plane magnetic field, and by an interlayer potential U that facilitates a single-particle gap. The most likely candidate for this state is the layer antiferromagnetic state, where electrons in the top and bottom layers have opposite spin polarization[1]. These results reflect the interplay between externally induced and spontaneous symmetry breaking whose relative strengths are tunable by external fields, and provide insight into other low dimensional systems.

Conclusions

The thermodynamic ground state of ABC-stacked TLG is most likely a layer antiferromagnetic state, which is expected to transition into a layer polarized state and a canted ferromagnetic state upon the application of external electric and magnetic fields, respectively.

Acknowledgements

A portion of this work was performed at the National High Magnetic Field Laboratory, which is supported by National Science Foundation Cooperative Agreement No. DMR-1157490, the State of Florida, and the U.S. Department of Energy.

YL and KM acknowledges the support by DOE BES Division under grant no. ER 46940-DE-SC0010597. FZ is supported by DARPA Grant No. SPAWAR N66001-11-1-4110. AHM is supported by the Welch Foundation under Grant No. TBF1473 and by the DOE Division of Materials Sciences and Engineering under grant No. DE-FG03- 02ER45958.

References

1. Y. Lee, D. Tran, K. Myhro, J. Velasco. Jr., N. Gillgren, C. N. Lau, Y. Barlas, J. M. Poumirol, D. Smirnov, and F. Guinea, Competition Between Spontaneous Symmetry Breaking and Single Particle Gaps in Trilayer Graphene, *Nature Communications* **5**, 5656 (2014).

Figure 1

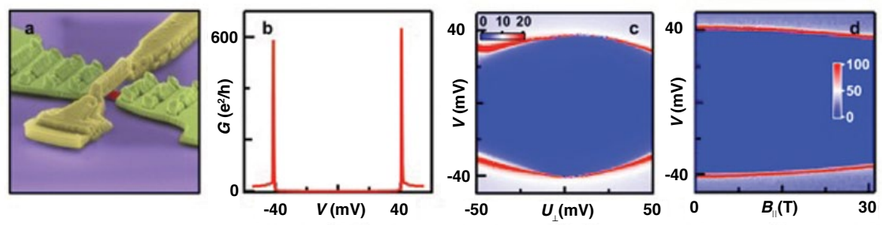

Transport data from dual-gated suspended trilayer graphene device. **(a)**. Device image. **(b)**. *G(V)* at n= $U_\perp$=0 and *T*=300 mK, showing a gap of ~41 meV. **(c)**. *G(V,* $U_\perp$*)* in units of e^2/h. The gapped region (dark blue) is reduced by interlayer potential $U_\perp$. **(d)**. *G(V,* $B_{||}$*)* at n=$U_\perp$=0 in units of e^2/h. The gap is reduced by large $B_{||}$.

Kondo / Heavy Fermion Systems

Phase transitions between different states of matter (for example, solid-liquid-gas) are quite common in everyday experiences, and for the most part, these phenomena are fundamentally understood in terms of classical theory. On the other hand, the phases transitions between different states of matter governed by quantum mechanical theory are less widely understood. More specifically, since the quantum me-chanical characteristics are developed in the temperature regime close to absolute zero, the phase changes are induced by tuning a parameter other than temperature. For example, variations in the exter-nal magnetic field may cause a material to change its magnetic and/or conducting state by traversing a quantum critical point. To gain insight about these new quantum states of matter, experimental studies of model systems are required to test theoretical descriptions. Indeed, a team lead by L. Balicas have explored the quantum critical regime of $CeCu_2Ge_2$, which possesses a quantum critical point near 30 Tesla.

$CeCu_2Ge_2$: Challenging our Understanding of Quantum Criticality

Zeng, B.; Zhang, Q.R.; Rhodes, D. (NHMFL); Shimura, Y. (U.Tokyo); Watanabe, D. (Kyoto U.); Baumbach, R.R. (NHMFL); Schlottmann, P. (FSU); Ebihara, T. (Shizuoka U.); Balicas, L. (NHMFL)

Introduction

In the zero temperature limit, quantum criticality may appear by suppressing a second-order phase transition. One example is the f -electron heavy-fermions, where quantum criticality (QC) is ascribed to either the suppression of a spin-density wave (SDW) ground state or the Kondo effect. Here, we unveil evidence for magnetic field-induced quantum criticality in $CeCu_2Ge_2$. In all directions, the field suppresses the second order transition from SDW state to paramagnetic state, and leads to some small Fermi surfaces (FSs). For the H//c axis, no evidence for QC is observed, and the effective mass (μ) of these small FSs is very small. But as H is rotated towards the a-axis, the effective mass increases considerably, and becomes undetectable for θ > 56°. Along a-axis, and at $H \sim 30$T, the resistivity becomes $\propto T$ which, coupled to the divergence of μ, indicates the existence of a field-induced QC point. We also show that the complexity of its magnetic phase diagram(s) makes $CeCu_2Ge_2$ an ideal system to explore field-induced quantum tricritical and QC end points.

Experimental

Oriented single crystals of $CeCu_2Ge_2$ were measured in resistive magnets, using a combination of torque and transport techniques, at ^{3}He and dilution fridge temperatures.

Conclusions

$CeCu_2Ge_2$ shows a complex phase diagram as a function of temperature, field, and angle. The quantum critical point appears along the a-axis, where the second order transition from SDW to PM state is suppressed by magnetic field. It also shows several first-order metamagnetic transitions. A tricritical point should exist in the phase diagram, where the first- and second-order transitions meet.

Acknowledgements

This work is supported by the National Science Foundation Cooperative Agreement No. DMR-1157490. L.B. is supported by DOE-BES through award DE-SC0002613. T. E. acknowledges CASIO science promotion foundation.

References

B. Zeng, Q. R. Zhang, D. Rhodes, Y. Shimura, D. Watanabe, R. E. Baumbach, P. Schlottmann, T. Ebihara and L. Balicas. Phys. Rev. B 90, 155101 (2014).

Figure 1

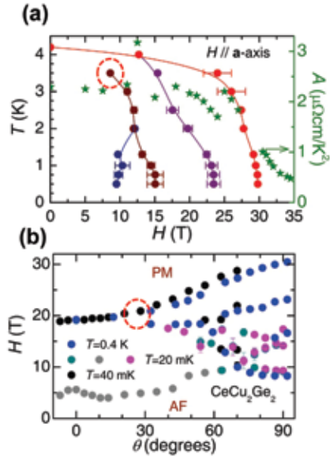

(A) *T-H* phase diagram along a-axis. There are several transitions in the phase diagram. The red line indicates the phase boundary between SDW and paramagnetic state. All the others are first-order metamagnetic transitions. **(B)** *H*-θ phase diagram near the base temperatures. θ is the angle between magnetic field and c-axis. The upper most line indicates the phase boundary between SDW and PM state. All the others are first-order metamagnetic transitions. Note that the red circle indicates an area where a first-order transition line meets the second-order one. A tricritical point should exist here.

CONTINUED ON NEXT PAGE

Figure 1 (Continued)

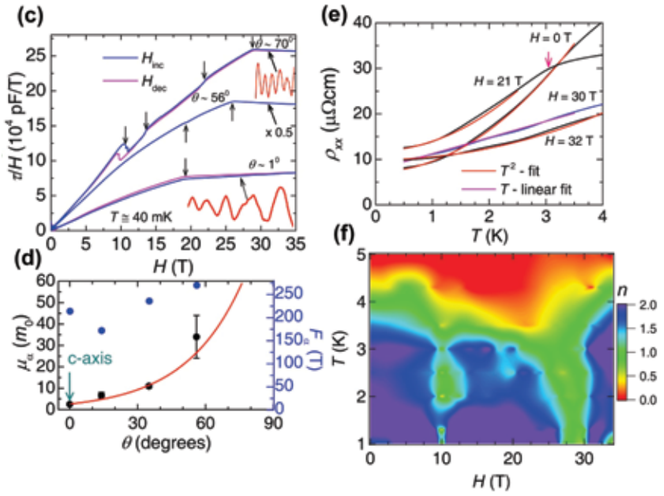

(C) The torque data measured by a capacitive cantilever at different angles. The oscillatory components are extracted in the PM state. Blue and magenta lines indicates field up and down sweep, respectively. **(D)** Effective masses extracted from the quantum oscillations for different angles. When the field rotates from c-axis to a-axis, the effective mass increases considerably. When θ>56°, the effective mass is so heavy that it becomes undetectable. The divergence of effective mass indicates the proximity to a quantum critical point along a-axis. **(E)** Resistivity as a function of the temperature for several fields applied along the a-axis. The red and pink lines are *T*-square and *T*-linear fits, respectively. One can see that at 30 T, the *T*-dependence becomes linear, suggesting the proximity to a quantum critical point. **(F)** Contour plot of the exponent $n = \partial ln[\rho(T) - \rho_0]/\partial ln(T)$ built from a complete set of $\rho(T,H)$ curves.

Kondo / Heavy Fermion Systems

Sometimes there are experimental observations that are just simply puzzling, and a phase transition in URu_2Si_2 at 17 Kelvin has been a head scratching result since 1985. Since the nature of the broken-symmetry phase proved so illusive, it was dubbed "Hidden Order". Recently, new experimental approaches have shed light on this rather extraordinary material. A team lead by Professor Ian Fisher of Stanford University has pioneered a novel "elastoresistance" technique, which they use to reveal new features associated with the Hidden Order phase in high magnetic fields.

Evidence for a Nematic Component to the Hidden Order Parameter in URu_2Si_2 in High Magnetic Fields

Shapiro, M.C.; Chu, J.-H.; Fisher, I.R. (Stanford University, Applied Physics); Riggs, S.C.; Baumbach, R.E. (NHMFL); Bauer, E.D. (LANL)

Introduction

URu_2Si_2 is an unconventional, heavy fermion superconductor with $T_c \sim 1.5$ K; however, prior to the onset of superconductivity, the material undergoes a phase transition to a novel "Hidden Order" state which has defied comprehensive understanding for over 30 years. Ongoing experimental efforts have focused on studying the nature of the Hidden Order parameter (which can be suppressed with chemical substitution, pressure, and magnetic field) and characterizing its symmetry.

With a novel piezo actuator technique, our previous zero field measurements used the differential elastoresistance (a quantity which relates normalized resistivity changes to applied strain) to probe the nematic susceptibility of URu_2Si_2, revealing that the Hidden Order parameter is a two-component vector that breaks four-fold rotational symmetry and couples to nematic fluctuations in the [110] direction [1]. Our most recent experiments at the Magnet Lab have explored the extent to which these nematic fluctuations persist in high field, particularly in the quantum critical regime where the Hidden Order state is suppressed to 0 K ($H_c \sim 35.1$ T).

Experimental

Magnetotransport measurements under strain were performed in the 31 T resistive and 45 T hybrid magnets at the NHMFL in a He^4 refrigerator.

Results and Discussion

The temperature dependence of the differential elastore-

CONTINUED ON NEXT PAGE

sistance in the [110] direction at different magnetic fields is presented in **Fig. 1b**, which are extracted from the slope of the normalized change in resistance to strain **(Fig. 1a).** There are two salient features of these data: 1) a pronounced downward anomaly at the Hidden Order transition temperature T_{HO}, which shifts downward in increasing field and scales as the heat capacity singularity; and 2) an extended regime above T_{HO} for which there is a large susceptibility which persists even as the phase transition goes from second to first order. The elastoresistance also diverges at fixed temperature while sweeping field (**Fig. 1c)**—the elastoresistance in orthogonal directions is large and opposite in sign for $H<H_c$, diverges at the critical field, and is essentially unresolvable at higher fields (high uncertainties due to the material's very small magnetoresistance in this field range). These data reveal that four-fold rotational symmetry is broken at the Hidden Order thermal phase transition even in a magnetic field. Furthermore, the nematic susceptibility appears to diverge towards the quantum phase transition.

Acknowledgements

A portion of this work was performed at the National High Magnetic Field Laboratory, which is supported by National Science Foundation Cooperative Agreement No. DMR-1157490, the State of Florida, and the U.S. Department of Energy. Work at Stanford was supported by the U.S. DOE, Office of Basic Energy Sciences, under contract DEAC02-76SF00515. Work at Los Alamos National Laboratory was performed under the auspice of the U.S. DOE, OBES, Division of Materials Sciences and Engineering.

References

1. Riggs, Scott C., et al., *Nature Comm.* **6**, 6425 (2015).

Figure 1

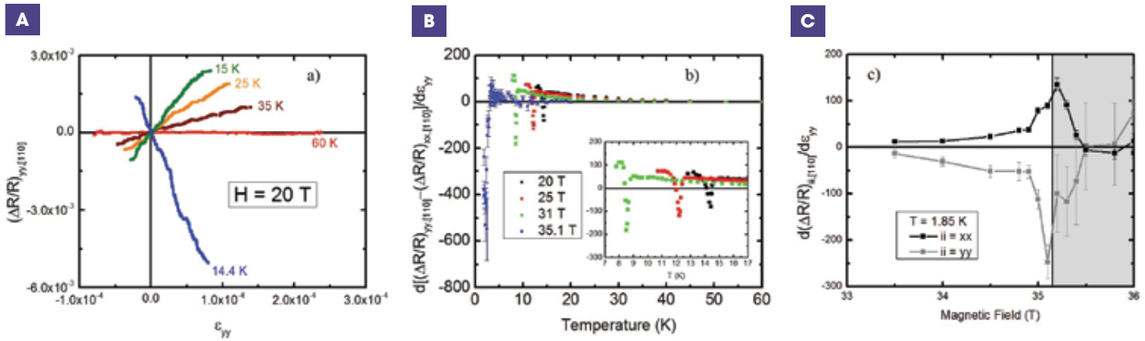

A) Temperature dependence of the resistive response to strain at $H = 20$ T. The slopes increase with decreasing temperature but then abruptly change sign at T_{HO}. **B)** Temperature dependence of the differential elastoresistance at different magnetic fields. Inset: Expanded view near the Hidden Order anomaly, which scales as the heat capacity singularity. **C)** Field dependence of the elastoresistance at 1.85 K. The resistive response diverges from below at the critical field. Vertical line marks the critical field associated with the quantum phase transition. Data for fields greater than H_c suffer from a poorer signal to noise due to the smaller magnetoresistance in this regime, but the divergence of the elastoresistance for $H<H_c$ is clear.

Kondo / Heavy Fermion Systems

The relationship between superconductivity and other correlated phases is an intriguing puzzle in a wide class of materials. The electron interactions that cause superconductivity often lead to other phases such as magnetism or density-waves when they are slightly tuned by pressure or strong magnetic fields. Using focused-ion beams, a single-crystal of $CeRhI_5$ was machined into a micrometer-scaled geometry to reach extreme current densities that are impossible to achieve in a macroscopic crystal. With this microscopic sample, an ETH-Zurich group teamed with NHMFL staff to explore the non-linear response under extreme conditions of magnetic field, temperature and current-densities. The results shed light onto the intricate interplay between superconductivity and other correlated phases, and these findings may impact the understanding of a wider class of similar systems.

Published in *Nature Communications* **6**, 6663 (2015)

Field-Induced Density Wave in the Heavy-Fermion Compound $CeRhIn_5$

Moll, P.J.W.; Galeski, S. (ETH Zurich, Switzerland); Zeng, B.; Balicas, L. (NHMFL, Tallahassee); Balakirev, F.F.; Bauer, E.D.; Ronning, F. (LANL, Los Alamos)

Introduction

$CeRhIn_5$ has attracted significant interest [1] due to its rich phase diagram involving 4f local moment anti-ferromagnetism and d-wave superconductivity under pressure. We found evidence for another ground state in the system, a magnetic field induced state akin to a density-wave (DW). The DW state is signaled by a hysteretic anomaly in the in-plane resistivity accompanied by the appearance of non-linear electrical transport at high magnetic fields (>27T), which are the distinctive characteristics of density-wave states.

Experimental

The experiment relies on transport experiments in microstructures carved from a $CeRhIn_5$ single crystal by the Focused Ion Beam technique[2]. We have thereby prepared single crystal bars with μm^2 cross-section, which enables us to apply significant current densities (>500kA/cm²) by applying only small currents in the mA range. This was the key to identify the density wave through the observation of non-linear transport due to its sliding motion. This collective excitation appears above a threshold electric field on the order of 10mV/cm. Sustaining such large electric fields in very good metals such as $CeRhIn_5$ is impractical in macroscopic single crystals.

Results and Discussion

A key signature of the transition in high fields is a large and strongly hysteretic jump of the in-plane resistivity. This large hysteresis enables us to directly investigate the Fermi surface of a supercooled electronic system and the appearance of additional quantum oscillation frequencies to clearly associate a Fermi surface reconstruction with the transition. Intriguingly, both the magnetization as well as the out-of-plane resistivity remain featureless across the transition field.

Conclusions

The absence of strong features in the magnetization points towards a negligible change in the density of states. Clearly just a small number of charge carriers are affected by the emergent high-field order, yet at the same time the in-plane resistivity is doubled. This implies that strong electronic correlations may lead to subtle orders, which nonetheless may significantly alter the systems properties. Such subtle orders might be a common feature among correlated electron systems, and its clear observation in the d-wave superconductor $CeRhIn_5$ adds a new perspective on the similarly subtle CDW state in the cuprates[3].

Acknowledgements

FIB and SEM work was supported by EMEZ and ScopeM at ETH Zurich. L.B. is supported by DOE-BES through award DE-SC0002613. Work at Los Alamos was supported by the U.S. Department of Energy, Office of Science, Basic Energy Sciences, Materials Sciences and Engineering Division. The NHMFL facility is funded through the US NSF Cooperative Grant No. DMR-1157490, the DOE, and the State of Florida.

References

1. T. Park et al., Nature **440**, 65-68 (2006)
2. P.J.W. Moll et al., Nature Materials **9**, 628-633 (2010)
3. P.J.W. Moll et al., Nature Communications **6**, 6663 (2015)

Figures

1

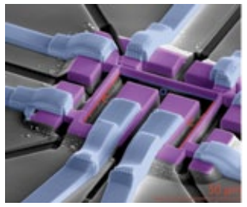

Fig.1 – FIB-cut single crystal microstructure of $CeRhIn_5$(purple) and FIB-deposited Pt contacts (blue).

Fig.2 – (A) Resistivity across the transition for fields along c at 380mK. A hysteretic transition is observed in the in-plane resistivity, while the c-axis resistivity and **(B)** magnetization under same conditions remain featureless.

2

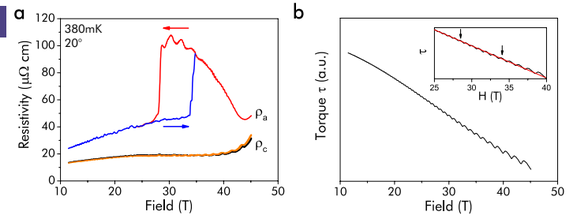

Magnetism & Magnetic Materials

The report by Bertaina et al., demonstrates the feasibility of coherently manipulating the spin states asso-ciated with solitons in a one-dimensional antiferromagnetic spin chain. High field EPR studies show that a narrow (<0.01 mT) signal assigned to solitons that are pinned to defects has exactly the same gyromag-netic ratio as the broader main signal, confirming that it is due to a spin state that is delocalized over many molecules. This makes it relatively robust with respect to local magnetic perturbations such as nu-clear spin flops, while the extended wavefunction provides a pathway to coupling and control, thereby suggesting new approaches to spin-based quantum information processing.

Rabi Oscillations of Pinned Solitons in Spin Chains: a Route to Quantum Computation & Communication

Bertaina, S.(IM2NP & CNRS) ; Dutoit, C.-E. (IM2NP & Aix Marseille U., France,); Van Tol, J. (NHMFL); Dressel, M. (U. Stuttgart, Germany, Physics); Barbara, B. (I. Néel & CNRS); Stepanov, A. (IM2NP & CNRS)

Introduction

We provide evidence for the coherence and Rabi oscillations of spin solitons pinned by the local breaking of translational symmetry in isotropic Heisenberg chains (simple antiferromagnetic Néel or spin Peierls).We show that these correlated spin systems that are made of hundreds of coupled spins bear an overall spin S = 1/2 and can be manipulated as a single spin. This is clearly contrary to known spin qubits which are paramagnetic centers, highly diluted to prevent decoherence. These results offer an alternative approach for spin qubits, paving the way for the implementation of a different type of quantum computer.

Experimental

Electron paramagnetic resonance is the main tool used in this study. Low frequency EPR in continuous wave and pulse mode has been performed on conventional Bruker X band spectrometer. High field EPR was performed on the quasi optical superheterodyne spectrometer of the NHMFL EMR Facility using its 12.5 T SC magnet.

Results and Discussion

The system used for this project, $(TMTTF)_2PF_6$ has been extensively studied in the last decades and is considered as a model of quantum spin chain with a strong isotropic Heisenberg interaction. Above 30 K a single Lorentzian-shaped EPR line is observed (CL in **Fig. 1**), displaying an anisotropy of the g factor, associated with different orientations of H. This anisotropy and the temperature dependence are typical of uniform quantum Heisenberg spin chains were intensively studied in the past. Below about 30 K a second EPR line, a very sharp one (PSL), appears at the same magnetic field as the main line. Using HF EPR, we found that the g-factors and the anisotropy are the same in the limit of resolution of the spectrometer. This result proves that the sharp signal is correlated to the spin chain and not an extrinsic defect. The defect is a break in the translational symmetry of the chain which polarizes the surrounding spins creating a “soliton-qubit”.

Rabi experiments were performed on the sharp line showing a long coherence time, comparable to other magnetic ion diluted systems. Due to an isotropic interqubit exchange interaction, the observed EPR lines are homogeneous and narrowed, eliminating the usual decoherence mechanisms such as the one associated with imperfectly identical qubits and dipolar interactions.

Conclusions

Defects in quantum spin chain provide a new kind of potential qubit. The strongly correlated nature of this system protects the soliton qubit from the decoherence of the environment. Moreover it has been theoretically shown that two qubits belonging to a spin chain are by nature entangled. The observation of coherence in pinned soliton paves the way for the implementation of a different type of quantum computer.

Acknowledgements

A portion of this work was performed at the National High Magnetic Field Laboratory, which is supported by National Science Foundation Cooperative Agreement No. DMR-1157490, the State of Florida, and the U.S. Department of Energy. We thank the city of Marseille, Aix Marseille University and IR RENARD FR3443 for financial support.

References

1. Bertaina, S., et al. Phys. Rev. B, 90, 060404 (2014).

Figures

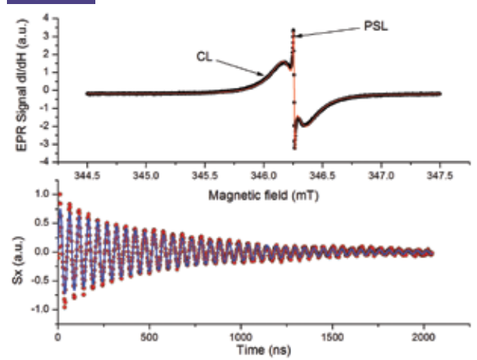

Fig. 1. EPR signal of (TMTTF)2PF6. Top: CW-EPR showing the chain line (CL) and the pinned soliton line (PSL). Bottom: Rabi oscillations of the PSL at T = 4 K.

Magnetism & Magnetic Materials

Permanent magnets are ubiquitous in everyday life. Strong permanent magnets, however, use rare-earth or precious metals that are not stable in their price and supply chains. Searching for alternate materials with useful magnetic properties is therefore important. Here, a new material with large coercitivity useful for applications in permanent magnets has been fabricated using ball-milling techniques and its magnetic properties have been characterized.

Published in: *J. Appl. Phys.* **115** (17) A723

Fabrication and Characterization of Bulk $Mn_{1-x}Ga_x$ Permanent Magnetic-Material

Brown, D.R. (FSU, NHMFL); Han, K. (NHMFL); Siegrist, T. (FAMU-FSU, NHMFL); Besara, T. (NHMFL)

Introduction

Permanent magnet materials (PM) are important components in many products [1]. Up to date, rare earth metals, such as Nd, Dy and Sm, or precious metals are key elements in the strongest PM for most of our magnetic applications [2, 3]. Typical rare-earth PM materials are $Nd_2Fe_{14}B$ and $SmCo_5$, which have coercivity of 12-20 kOe and 15-25 kOe, respectively. Recently, researchers are seeking alternative PM materials that need less rare earth or precious metals because of the issues of their supplies [3]. In this report, we outline our effort in making bulk PM materials that contain neither rare earth nor precious metal elements.

Experimental

We prepared the PM materials by high-energy ball-milling and heat treatments. The milled powders were pressed, sealed in evacuated quartz tubes and heat-treated at temperatures ranging between 280 °C and 350 °C. Magnetic properties were investigated by a vibrating sample magnetometer (VSM) in a physical property measurement system (PPMS, Quantum Design Model 6000) in magnetic fields up to 7.5 T (H_a) at a temperature of 30 °C.

Results and Discussion

We found that the annealing temperatures significantly affect both the coercivity (H_c) and overall shape of the magnetization curves, as shown in Fig. 1. However, between 325 °C and 350 °C, the H_c remains almost the same and the average value of Hc is18.8 kOe. This value is close to the values obtained from $Nd_2Fe_{14}B$ and $SmCo_5$. Our alloys have major phases with structure similar to $Mn_{0.85}Ga_{0.15}$ (space group of 213 (P4132)), and Mn_3Ga (space group of 139 (I4/mmm), as shown by X-Ray diffraction data in Fig. 2. An oxide was also identified as MnO, as well as a small amount of a Mn(α) phase.

Conclusions

In summary this effort has allowed us to create rare-earth and precious-metal free magnets with coercivities that are competitive with Nd-Fe-B magnets.

Acknowledgements

The work was undertaken at the NHMFL that is supported by Florida State, DOE and NSF with grant number of DMR 1157490. T.B. and T.S. acknowledge support by the Department of Energy, Office of Basic Energy Sciences, Division of Materials Sciences, under award DE-SC0008832.

References

1. KHJ Buschow. New Developments in Hard Magnetic-Materials. Rep. Prog. Phys. 54, 1123, (1991).
2. J.F. Herbst, Reviews of Modern Physics 63, 819 (1991).
3. L. H. Lewis, Metallurgical & Materials Transactions A 44, 2 (2012)
4. Brown, D.R.; Han, K. and Siegrist, T., Hard magnetic properties observed in bulk Mn1-xGax, *J. Appl. Phys.*, 115 (17), 17A723 (2014)

Figures

1

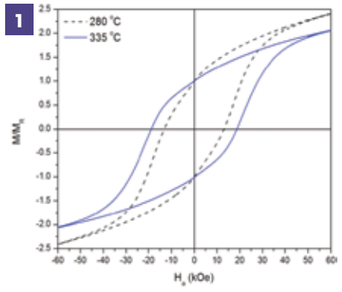

Fig. 1 Hysteresis loops of samples heat treated at varying temperatures.

2

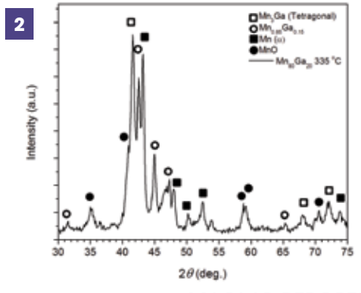

Fig. 2 X-ray diffraction plot of high coercivity Mn-Ga.

Magnetism & Magnetic Materials

In iridium oxide materials, the 5d magnetic orbitals have been predicted to show strong exchange anisot-ropy (as opposed to single-ion anisotropy) due to their extended size and strong spin-orbit coupling. This enables new physics such as frustrated Kitaev models where only the spin components that point along an exchange bond couple to each other. This work explores the magnetic anisotropy of Li_2IrO_3 by torque magnetometry in DC and pulsed fields. The results are consistent with exchange anisotropy since the anisotropy far exceeds what should occur in this crystal structure due to single-ion anisotropy, and moreover the anisotropy is strongly temperature and magnetic field dependent, quintupling in size at high fields

High Field Magnetic Properties of Li_2IrO_3

Modic, K.; Ramshaw, B.; Shehkter, A. (NHMFL); Analytis, J. (UC Berkeley); McDonald, R. (NHMFL)

Introduction

Li_2IrO_3 has a three-dimensional honeycomb structure with the same local connectivity as the layered honeycomb. Such materials are expected to host Kitaev-like physics and a spin-liquid ground state. To sensitively probe the magnetic anisotro-py of small single crystals, torque magnetometry was performed using a piezo-resistive micro-cantilever. Previous torque mag-netometry measurements in the 20 T superconducting magnet revealed that two of the principal components of susceptibility reorder upon lowering temperature [1], with an order of mag-nitude increase in the crystallographic b component of suscep-tibility at low temperature. With a high temperature g-factor anisotropy that is constrained by the crystal structure and no evidence for lattice distortions upon cooling, such behavior is believed to be due to spin-anisotropy of exchange interactions.

Experimental

The pulsed field torque measurements in Figure 1 represent magnetic anisotropy in the crystallographic b-c plane with magnetic field applied almost parallel to the b axis. The change of sign of the torque signal with small applied fields confirms the reordering of the principal components of susceptibility to occur at approximately 70K. More interestingly, the change of sign is accompanied by an anisotropy at high fields that is five times larger than that observed at low fields, as illustrated by the magnitude of the torque response. The torque remains finite and continues to grow up to the largest measureable mag-netic field, indicating that the induced moment is not co-linear with the applied field. Larger magnetic fields are required to saturate the torque signal.

Results and Discussion

To explore the possibility of new magnetically ordered phases at high fields, an angle dependence of torque measurements is necessary. However, Li_2IrO_3 experiences an order of magnitude change in anisotropy with field orientation at low temperature resulting in a very large torque. During the final pulse at 70K in Figure 1, the large magnetic response resulted in a broken lever near maximum field. The data in Figure 1 was taken on a fixed angle probe and the orientation of the crystal with respect to the applied field was chosen to minimize the torque signal by aligning the field with a principal magnetic direction. As the sample is rotated away from these directions, the torque signal is likely to increase, making it difficult to do an angle dependence. Future work will explore alternate methods for minimizing the torque signal to measure Li_2IrO_3 at high fields.

Acknowledgements

This work was performed at the National High Magnetic Field Laboratory, which is supported by National Science Foundation Cooperative Agreement No. DMR-1157490, the State of Florida, and the U.S. Department of Energy.

References

1. Modic, K.A., et al., Nat Commun, 5: 4203, 2014. Doi:10.1038/ncomms5203

Figure 1

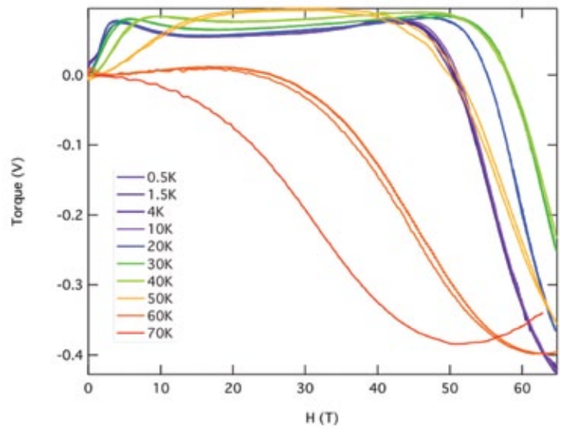

Torque magnetometry with magnetic field aligned with the crystallographic b direction. The torque signal shows the magnetic anisotropy in the crystal-lographic b-c plane at temperatures ranging from 0.5 to 70K.

Magnetism & Magnetic Materials

Spin liquids are materials that are prevented from exhibiting traditional static magnetic order down to zero temperature despite strong magnetic interactions -- because these interactions are geometrically frustrat-ed. The kagome lattice material Herbertsmithite has been extensively investigated for spin liquid behavior but progress has been slowed by its tendency to form free Cu spins between magnetic layers. This work explores the torque magnetometry to high magnetic fields where free spins saturate, and so finds the intrinsic behavior of the frustrated lattice. Behavior consistent with a gapless spin liquid is ob-served, in contrast with theoretical predictions for a gapped spin liquid.

High Field Magnetic Ground State of Kagome Lattice Spin Liquid Herbertsmithite

Asaba, T.; Li, G.; Lawson, B.J.; Yu, F.; Tinsman, C.; Li, L. (Univ. Michigan); Han, T.-H. (Univ. Chicago); Lee, Y.S. (MIT)

Introduction

An exciting field of modern condensed matter physics is the quantum spin liquid. The strong frustration leads to the lack of magnetic ordering and the emergence of novel physical phe-nomena in the ground state. Herbertsmithite $ZnCu_3(OH)_6C_{l2}$ is a kagome lattice antiferromagnet with 1/2 spin and has been demonstrated to be a likely candidate of spin liquid by recent neutron scattering measurements [1]. However, the direct determination of the magnetic ground state at extremely low temperature has always been challenging because of two rea-sons: (1) The direct magnetization measurement is difficult to perform at extremely low temperatures; and (2) In the Zn plane there are extra free Cu moments whose Curie-like paramagnetic signal dominates the magnetic response at low temperature. To solve the problem, we applied torque magnetometry on single crystalline Herbertsmithite using high-resolution cantilever setups [2].

Experimental

High-resolution torque magnetometry was used to measure the magnetic moment of the samples [3-8]. Torque is measured as the change of the capacitance between the metal cantilever and a fixed metal plate.

Results and Discussion

We measured the angular dependence of the magnetic torque and the magnetization of Herbertsmithite at 20 mK < T < 40 K and in intense magnetic field. The intrinsic magne-tization from the kagome lattice turns out to be linear with magnetic field, and the magnetic susceptibility is independent of temperature at 20 mK < T < 5 K.

Conclusions

Our results show that the high magnetic field phase of Her-bertsmithite exists as a gapless spin liquid state. Such a state is not affected by the field-driven anomalies at 7 T – 15 T, which possibly originate from the interlayered Cu spins. Far from the gapped spin liquid state expected by theorists, this result is the first demonstration of the gapless spin liquid ground state in Kagome-lattice quantum magnets [2].

Acknowledgements

A portion of this work was performed at the National High Magnetic Field Laboratory, which is supported by National Sci-ence Foundation Cooperative Agreement No. DMR-1157490, the State of Florida, and the U.S. Department of Energy. The material is based on work supported by the Department of Energy under Award number DE-SC0008110. Asaba thanks the support from the Nakajima Foundation.

References

1. T. H. Han, et al., *Nature* **492**, 406 (2012).
2. T. Asaba, et al., *Phys. Rev. B,* **90**, 064417 (2014).
3. Lu Li, et al., *Nature Physics,* **3,** 311-314 (2007).
4. Lu Li, et al., *Nature Physics,* **7**, 762-766 (2011).
5. Lu Li, et al., *Science,* **321**, 547-550 (2008).
6. B. J. Lawson, Y.S. Hor, Lu Li, *Phys. Rev. Lett.* **109**, 226406 (2012).
7. B. J. Lawson, et al., *Phys. Rev. B* **90**, 195141 (2014).
8. G. Li, et al., *Science,* **346**, 1208 (2014).

Figure 1

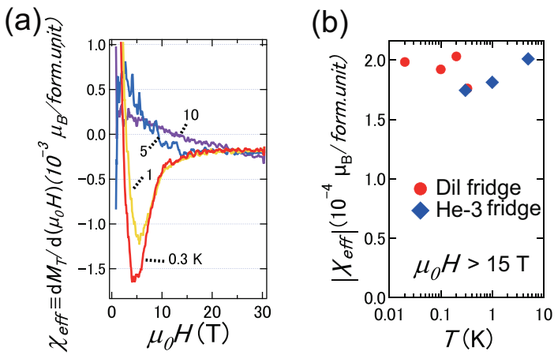

Fig. 1 (a) Effective magnetic susceptibility χ_{eff} is plotted as function of field H up to 31 T for single crystal Herbersmithite **(b)** The temperature T dependence of the absolute value of the high-field χ_{eff} of the kagome lattices.

Magnetism & Magnetic Materials

The multiferroic material Ni_3TeO_6 shows a record large non-hysteretic magnetoelectric coupling. This occurs at a magnetic field-induced spin flop transition. The magnetic, electric and structural properties to high magnetic fields in combination with ab-initio modeling yield a microscopic model to explain the source of magnetic field-induced changes in the electric polarization.

Colossal multiferroic behavior in Ni_3TeO_6 explained through high-field measurements and ab-initio calculations

Kim, J.W.(Rutgers University); Mun, E.D.(Simon Fraser University); Jaime, M.; Harrison, N.; (NHMFL-PFF); Oh, Y.; Yang, J.J.; Cheong, S.W.; Artyukhin, S.; Vanderbilt, D. (Rutgers University); Zapf, V. (NHMFL-PFF)

Introduction

Multiferroic behavior is the coexistence of magnetic and electric order in the same material. Coupling between them can result from several interesting physical phenomena, and has applications to magnetic sensing, high-frequency tunable electronic devices and data storage. The challenge is to find large, couplings with low hysteresis. Ni_3TeO_6 shows record large non-hysteretic magnetoelectric coupling at low magnetic fields. Using magnetic fields up to 92 T at NHMFL-PFF, we discovered an additional phase transition at 52 T, accompanied by a colossal change in polarization (3 mC/m^2), among the largest magnetically induced polarization changes known. The comprehensive magnetic, electric, and structural data to high fields in combination with density-functional calculations and previous elastic neutron diffraction data at zero field allow us to construct a microscopic model. Thereby we clarify the origin of the multiferroic behavior.

Experimental

We measured the magnetization M, electric polarization change ΔP, and magnetostriction ΔL/L in 65 T and 92 T pulsed magnets, and calibrate against data taken in DC superconducting magnets.

Results

Fig. 1 shows the high field data in (a-f) and the simulations in (g) and (h). Two successive field-induced transitions are observed for H || c, and one for H || ab. **Fig. 2** shows a model of exchange interactions among the three Ni sites, and a sketch of the calculated field-induced magnetic ordering for two crystalline unit cells.

Conclusions

This material is a 'type I' multiferroic – an existing polar crystal structure is modified by magnetostriction. The magnetically frustrated magnetic structure traverses several field-induced phase transitions, and the resulting magnetostriction in canted Ni-O-Ni bonds modifies the electric polarization.

The origin of the non-hysteretic magnetoelectric coupling at Hc1 is an unusual non-hysteretic spin flop to a canted spin structure, while the even larger magnetoelectric coupling at the high-field transition results from the flipping of two Ni spins and a halving of the magnetic unit cell. Similar behavior in molybdates and other related compounds is being explored to find even larger magnetoelectric coupling effects.

Acknowledgements

This work is funded by the D.O.E. BES project "Science at 100 Tesla". The NHMFL facility is funded by the NSF through cooperative grant DMR-1157490, by the DOE and by the State of Florida.

References

1. Y. S. Oh, Sergey Artyukhin, Jun Jie Yang, Vivien Zapf, Jae Wook Kim, David Vanderbilt, and Sang-Wook Cheong, *Nature Commun.* **5**, 3201 (2014).
2. Jae Wook Kim, S. Artyukhin et al. PRL under revision.
3. I. Zivkovic et al, *J. Phys. Cond. Matter* **22**, 056002 (2010)

Figures

1 **A-F:** Magnetization (M), electric polarization change (ΔP) and magnetostriction (ΔL) up to 92 Tesla for different temperatures T and crystalline directions.

G-H: Theoretical simulations of the magnetization and magnetostriction.

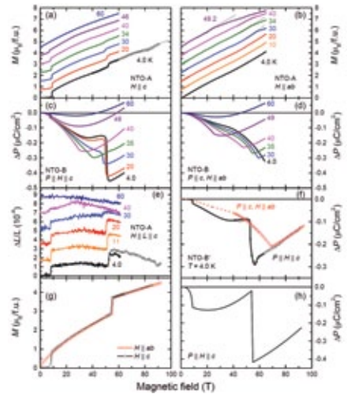

2 **A:** Magnetic exchange interactions J1-J5 among the three Ni sites (red, green and blue).

B-E: Predicted evolution of the magnetic structure (two unit cells of the crystal structure).

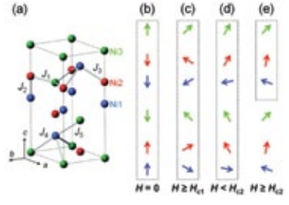

Magnetism & Magnetic Materials

A record large coercive field of 55 tesla has been observed in Sr_3NiIrO_6 using pulsed fields up to 60 T. This large coercive field is thought to originate in the overlap of extended Ir 5d-orbitals with Ni 3d orbitals and O 2p orbitals, producing a large magnetocristalline anisotropy. This mechanism is different from that in traditional hard ferromagnets, and may be tailored for other systems.

55 Tesla Coercive Magnetic Field in Frustrated Sr_3NiIrO_6

Singleton, J.; Wook Kim, J.; Hansen, A.; Mun, E.-D.; Zapf, V.S. (NHMFL-PFF); Goddard, P. (Warwick U.); Luo, X.; Oh, S.; Cheong. S.-W. (Rutgers U.)

Introduction

We have measured extremely large coercive magnetic fields of up to 55 T in Sr_3NiIrO_6. As far as we are aware, this is the largest coercive field observed thus far.

Experimental

The pulsed-field magnetization experiments used a 1.5 mm bore, 1.5 mm long, 1500-turn compensated-coil susceptometer, constructed from 50 gauge high-purity copper wire. The pulsed-field data were calibrated using a commercial vibrating-sample magnetometer.

Results and Discussion

Hysteresis loops and large coercive fields: The Figure shows magnetization *M* as a function of magnetic field in a series of pulses using a capacitor-bank-driven 65 T pulsed magnet. Sample numbers (S = single-crystals, P = polycrystals), field directions and measurement temperatures are given in each section of the Figure; the vertical jumps in *M* occur at the coercive field. In (b), (f) no hysteresis is observed in the **H** perpendicular to **c** configurations. In (a), (b), and (d), absolute magnetization values, measured in commercial SQUID and vibrating-sample magnetometers, were used to calibrate the pulsed- field data.

Conclusions

This extraordinarily hard magnetism has a completely different origin from that found in conventional ferromagnets. Instead, it is due to the evolution of a frustrated antiferromagnetic state in the presence of strong magnetocrystalline anisotropy due to the overlap of spatially-extended Ir^{4+} 5d orbitals with oxygen 2p and Ni^{2+} 3d orbitals. This work highlights the unusual physics that can result from combining the extended 5d orbitals in Ir^{4+} with the frustrated behaviour of triangular lattice antiferromagnets.

Acknowledgements

A portion of this work was performed at the National High Magnetic Field Laboratory, which is supported by National Science Foundation Cooperative Agreement No. DMR-1157490, the State of Florida, and the U.S. Department of Energy. Work at Rutgers is supported by NSF-DMR 1233349.

References

1. J. Singleton, *et al.*, under review (2014).

Figure 1

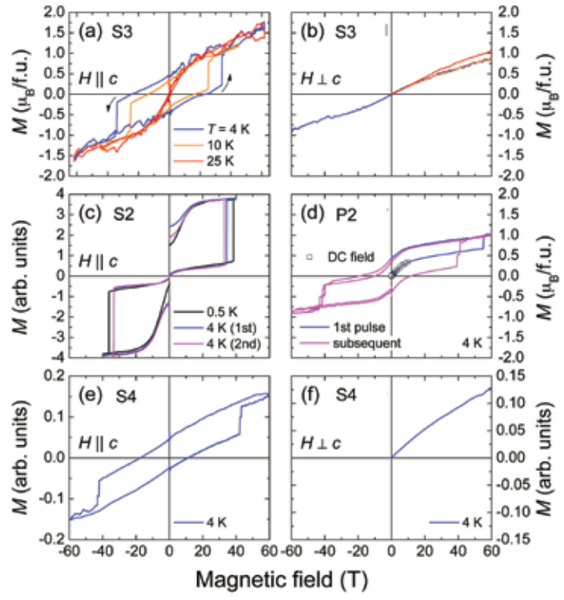

Semiconductors

MilliKelvin magnetotransport of strongly interacting 2D holes in high mobility, gated, GaAs quantum wells has been used to investigate possible anisotropy in the field-induced re-entrant insulating phase. The lat-ter phase was observed in the resistivity at a magnetic field that depended on hole density but that was independent of current direction. This shows that the re-entrant insulating phase is not due to a proposed anisotropic stripe order, but is instead caused by Wigner crystallization.

Isotropic vs. Anisotropic Transport in the Field Induced Wigner-Crystal State in 2D Holes

Gao. X.P.A.; Goble, N.J. (Case Western Reserve University); Serafin, A.; Yin, L.; Xia, J.S.; Sullivan, N.S. (NHMFL, UF Physics); Pfeiffer, L.N.; West, K.W. (Princeton University).

Introduction

Strong Coulomb interactions are expected to drive two-dimensional (2D) carriers in semiconductor hetero-interface into a crystal ground state in the ultra-low density regime. A perpendicular magnetic field can stabilize this Wigner crystal (WC) state at higher carrier densities such that the disorder effect is weak. Besides 2D Wigner crystal and metallic liquid, a number of isotropic or anisotropic states were predicted in theories: stripe, WC bubble in liquid etc. [1] We studied transport of strongly interacting 2D holes in high mobility GaAs quantum wells (QWs) to investigate the effects of current transport direction on the magnetic field induced WC state in low fields which is shown as a reentrant insulating phase (RIP) in the magneto-transport data [2].

Experimental

Low frequency magneto-transport measurements using lock-in technique were primarily performed on high mobility GaAs QW samples from wafers grown on (311)A GaAs. $Al_{0.1}Ga_{0.9}As$ barriers and Si delta doping layers were placed symmetrically at a distance of 195 nm away from the 10 nm thick GaAs QW. All the samples have density p ~ $1.3 \times 10^{10}/cm^2$ and mobility $\mu = 5 \times 10^5$ cm^2/Vs without gating. A back gate was placed approximately 0.3mm underneath the sample and used to tune the hole density. Current was applied along two perpendicular directions: [233] and [011] to compare if the insulating behavior in the RIP (or WC) state is isotropic or not.

Results and Discussion

The RIP due to WC formation at low *B* has been observed [2] as related to the strongly interacting character of the dilute 2D hole system and high sample quality. This RIP was found to exist in both current directions. Due to the corrugation of GaAs's (311)A surface, the mobility along [233] is a few times higher than the [011] direction, causing the resistance values to be different for these two current flow configurations. However, a clear insulating peak is found around ~0.3 Tesla for both directions, indicating that the RIP is isotropic, not due to orientation order like one expects in stripe phases.

Conclusions

By measuring the magneto-transport along two different current flow directions, we found that the RIP phase in dilute 2D holes in GaAs QWs is not related to anisotropic stripe phase, confirming its relation to the WC with quasi-long range position order.

Acknowledgements

A portion of this work was performed at the National High Magnetic Field Laboratory, which is supported by National Science Foundation Cooperative Agreement No. DMR-1157490, the State of Florida, and the U.S. Department of Energy. Work at CWRU was supported by NSF (grant number DMR-0906415).

References

1. B. Spivak and S. A. Kivelson, Annals of Physics 321, 2071 (2006).
2. R. L. J. Qiu, X. P. A. Gao, L. N. Pfeiffer, K. W. West, Phys. Rev. Lett. 108, 106404 (2012).

Figure 1

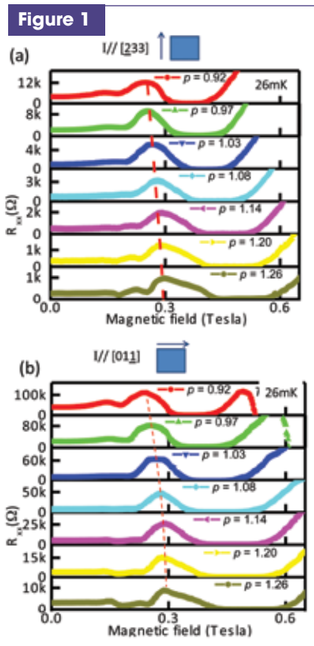

Magneto-resistance of a square shaped 2D hole GaAs QW sample measured with current along two perpendicular directions. The density ρ is in units of $10^{10}/cm^2$. Experimental temperature was 26mK. The red dashed line in both **(A)** and **(B)** indicate the location of reentrant insulating phase due to WC.

Semiconductors

The micro-photoluminescence optical probe and superconducting magnet in Cell 3 were used to study $MoSe_2$ monolayers prepared by mechanical exfoliation. Under a perpendicular magnetic field, the energy of the circularly polarized luminescence from the the K and K' valleys of the monolayers shifts in opposite directions, and at the same time the emission strength is shifted from one valley to the other. These observations shows unambiguously that the applied magnetic field induces a splitting of the valley energy and a polarization of the valley occupation.

Published in: *Phys. Rev. Lett.* **113**, 266804 (2014)

Valley Splitting and Polarization by the Zeeman Effect in Monolayer $MoSe_2$

Li, Y.; Low, T.; Chernikov, A.; Cui, X.; Arefe, G.; Kim, Y.D.; van der Zande, A.; Rigosi, A.; Hill H.M.; Kim S.H.; Hone, J.; Heinz T.F. (Columbia U., Physics); Ludwig, J.; Li, Z.; Smirnov, D. (NHMFL)

Introduction

Monolayer $MoSe_2$ crystals feature two inequivalent valleys at the K and K' points of its Brillouin zone. Since the valleys are linked by time-reversal symmetry, they are energetically degenerate, while the magnetic moments of the corresponding valley states are of the same magnitude, but have opposite sign. Coupling to the valley magnetic moments by a magnetic field thus presents new opportunities for the study of the fundamental physical properties of the valley electronic states, as well as for the development of new approaches to valleytronic control.

Experimental

The monolayer $MoSe_2$ samples were prepared by mechanical exfoliation of the bulk crystal. To study the magnetic response of the valleys in these monolayers, we measured their photoluminescence (PL) spectrum in the presence of an out-of-plane magnetic field. The measurements were performed using a micro-PL optical probe and the superconducting magnet in cell #3.

Results and Discussion

Our main result is summarized in Fig. 1. Here we present PL spectral maps from a monolayer $MoSe_2$ crystal with a perpendicular magnetic field varying from -10 T to +10 T. The two peaks in the PL spectra correspond to emission from neutral and charged excitons, with the neutral exciton emission lying at higher energy. The two panels correspond to the detection of two different circular polarization states, arising, respectively, from the K and K' valleys in the Brillouin zone. [1] The PL energies of the two peaks shift linearly with the magnetic field and the direction of the shifts is reversed for photons with opposite circular polarization states. The linear shift corresponds to the Zeeman effect on the interband transition energy. The reversal of the shift direction demonstrates the breaking of valley degeneracy at finite magnetic field.

In addition to the shift in the peak energies, we also observe in **Fig. 1** a monotonic variation in the relative intensities of the charged and neutral exciton with magnetic field, with opposite trend for emission from the two valleys. Since the relative intensity of the two exciton species is an indicator of charge density in the valleys, the valley dependent variation of the relative intensity shows that an imbalance in charge density in the two valleys, i.e. valley polarization, has been produced.

Conclusions

Through measurements of circularly polarized photoluminescence from neutral and charged excitons in $MoSe_2$, we have demonstrated the lifting of the K/K' valley degeneracy by a magnetic field and also the creation of valley polarization. These studies provide understanding of spin-valley physics in monolayer transition metal dichalcogenides. The paper reporting these findings will appear soon in Physical Review Letters [2].

Acknowledgements

A portion of this work was performed at the National High Magnetic Field Laboratory, which is supported by National Science Foundation Cooperative Agreement No. DMR-1157490, the State of Florida, and the U.S. Department of Energy. The authors also acknowledge the U.S. Department of Energy, Office of Basic Energy Sciences for support through Columbia Energy Frontier Research Center (grant DE-SC0001085) for the preparation and characterization of samples and device structures; the National Science Foundation through grants DMR-1122594 and DMR-1124894 for support for the optical measurements and through grant DMR-1106225 for data analysis.

References

1. Mak, K.F. et al., *Nature Nanotech.* 7, 494 (2012); Zeng, H. et al., ibid. 7, 490 (2012); Cao, T. et al., ibid. 3, 887 (2012).
2. Li, Y. et al., *Phys. Rev. Lett.* 113, 266804 (2014).

Figure 1

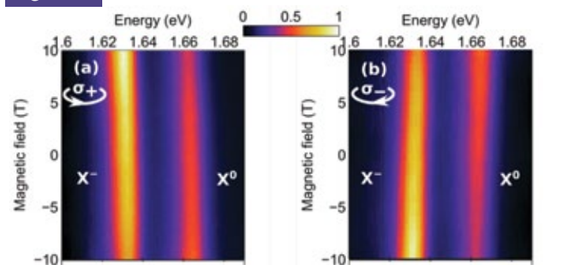

False color representation of the σ+ **(a)** and σ– **(b)** circularly polarized PL spectra for monolayer $MoSe_2$ in the low-doping regime as a function of the strength of the applied perpendicular magnetic field.

Semiconductors

Devices based on black phosphorus (BP) are good candidates for future nanoelectronic and optoelec-tronic applications. BP may be cleaved into single layers like graphene; however, by contrast, BP has an intrinsic direct band gap that approaches 2 eV in the atomic monolayer limit. High mobility carriers in BP are required for successful device applications. Here two groups report the fabrication of FETs based on BP crystals a few layer thick. 2D carrier mobilities high enough to observe Shubnikov-de Haas oscillations and to investigate the electronic transport properties of the FETs are observed.

Published: Tayari, V. et al., *Nature Communications*, **6**, 7702 (2015).

Two-Dimensional Magnetotransport in a Black Phosphorus Naked Quantum Well

Tayari, V.; Gervais, G.; Szkopek, T. (McGill University)

Introduction

Black phosphorus (bP) is the second known elemental allotrope with a layered crystal structure that can be mechanically exfoliated down to atomic layer thickness [1-3]. In contrast to graphene, bP has an intrinsic direct band gap of 0.3 eV bandgap, which approaches 2 eV in the atomic monolayer limit [1], ideal for applications in electronics and optoelectronics.

Experimental

We have fabricated bP naked quantum wells of varying thickness in a back-gated field effect transistor geometry. Using an encapsulating polymer superstrate **(Fig. 1a)**, we have protected bP from oxidation, allowing a variety of experiments to be conducted from 300 K to 300 mK. Further, using a resistive magnet with a 300 mK He^3 cryostat at the NHMFL, we have measured magnetoresistance up to 35 T.

Results and Discussion

We have observed field effect mobilities up to 900 cm^2/Vs and on/off current ratios exceeding 10^5, indicative of the high electronic quality of naked bP [3]. Shubnikov-de Haas (SdH) oscillations observed in magnetotransport measurements **(Fig. 1b)** reveal the presence of a 2D hole gas with Schrödinger fermion character (Berry phase $\beta \approx 0$) in an accumulation layer at the bP/oxide interface **(see Fig. 1c)**. The Schrödinger fermion character is expected with the band extremum located at the time invariant momentum Z in the Brillouin zone.

Conclusions

Our work demonstrates that 2-D electronic structure and 2-D atomic structure are independent. 2-D carrier confinement can be achieved in layered semiconducting materials without necessarily approaching atomic layer thickness, advantageous for materials that become increasingly reactive in the few-layer limit such as bP. Since the completion of our work, we have learned of similar and consistent results reported by the Yuanbo Zhang group [5].

Acknowledgements

A portion of this work was performed at the National High Magnetic Field Laboratory, which is supported by National Science Foundation Cooperative Agreement No. DMR-1157490, the State of Florida, and the U.S. DOE. This work was funded by NSERC, CIFAR, FRQNT, RQMP and CRC program.

References

1. L. Li, Y. *et al.*, *Nature Nanotech*, 9, 372 (2014).
2. F. Xia, *et al.*, *Nature Comm.* 5, 4458 (2014).
3. A. Favron, *et al.*, arXiv:1408.0345 [cond-mat.mes-hall].
4. V. Tayari, *et al.*, arXiv:1412.0259 [cond-mat.mes-hall].
5. L. Li, *et al.*, arXiv:1411.6572 [cond-mat.mes-hall].

Figure 1

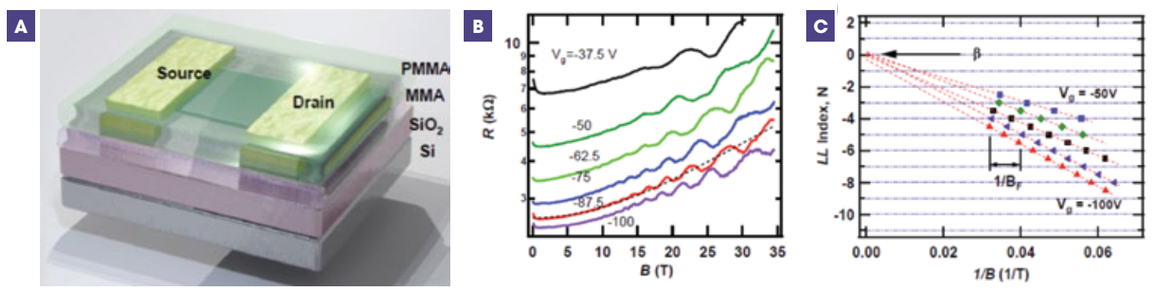

Figure 1: a, A schematic of a bP FET structure used in our work. b, The measured 2 point resistance R as a function of applied magnetic field B at different gate voltages at T=300 mK. c, The Landau fan diagram of LL index N versus 1/B at different gate voltages. The SdH frequency, BF, and Berry phase, β, are extracted from the slope and intercept of the diagram. Quantitative analysis reveals the holes to be confined to a single 2D sub-band.

Semiconductors

Devices based on black phosphorus (BP) are good candidates for future nanoelectronic and optoelec-tronic applications. BP may be cleaved into single layers like graphene; however, by contrast, BP has an intrinsic direct band gap that approaches 2 eV in the atomic monolayer limit. High mobility carriers in BP are required for successful device applications. Here two groups report the fabrication of FETs based on BP crystals a few layer thick. 2D carrier mobilities high enough to observe Shubnikov-de Haas oscillations and to investigate the electronic transport properties of the FETs are observed.

Published: Li, L. et al. *Nature Nanotechnology*, **10**, 608–613 (2015)

Quantum Oscillations in Black Phosphorus Two-dimensional Electron Gas

Li, L.; Chen, G. (Fudan University); Jun Ye, G.; Hui Chen, X. (University of Science and Technology of China); Tran, V.; Fei, R.; Yang, L. (Washington University in St. Louis); Wang, H.; Wang, J. (Peking University); Watanabe, K.; Taniguchi, T. (National Institute for Materials Science); Zhang, Y. (Fudan University)

Introduction

Black phosphorus has recently emerged as a new member in the family of two-dimensional (2D) atomic crystals[1,2]. It is a semiconductor with a tunable bandgap and high carrier mobility – material properties that are important for potential optoelectronic and high-speed device applications.

Experimental

In this work, we achieve a record-high carrier mobility in black phosphorus by placing it on hexagonal boron nitride (h-BN) substrate **(Fig. 1a)**. 2D electron and hole gas is induced at the black phosphorus/h-BN interface by the gate electric field. The exceptional mobility of the 2D electron gas created at the interface allows us to observe quantum oscillations for the first time in this material **(Fig. 1b** and **Fig. 1c)**. The transport data was taken at Cell 9 in NHMFL.

Results and Discussion

We extract crucial information about the black phosphorus 2D electron and hole gas from the observed quantum oscillations. Specifically, we obtain a hole effective mass of $0.34m_0$ and an electron effective mass of $0.47m_0$, which are larger than the values measured in the bulk[3], possibly due to quantum confinement. The quantum life time of the carrier is determined to be ~0.1ps.

Conclusions

Our experimental results introduce black phosphorus 2D electron gases to the elite family of high quality electron systems, and open the door to future research on quantum transport in black phosphorus.

Acknowledgements

A portion of this work was performed at the National High Magnetic Field Laboratory, which is supported by National Science Foundation Cooperative Agreement No. DMR-1157490, the State of Florida, and the U.S. Department of Energy. L.L., G.C. and Y.Z. acknowledge financial support from the National Basic Research Program of China (973 Program) under the grant Nos. 2011CB921802 and 2013CB921902, and NSFC under the grant No. 11034001. G.J.Y and X.H.C. acknowledge support from the 'Strategic Priority Research Program' of the CAS under the grant No. XDB04040100 and the NBRP of China (973 Program) under the grant No. 2012CB922002. V.T., R.F. and L.Y. are supported by NSF DMR-1207141. H.W. and J.W. are supported by NBRP of China under the grant No. 2013CB934600, and NSFC under the grant No. 11222434.

References

1. Li, L. et al. *Nature Nanotechnology* **9**, 372–377 (2014).
2. Liu, H. et al. *ACS Nano* **8**, 4033–4041 (2014).
3. Narita, S. et al. *J. Phys. Soc. Jpn.* **52**, 3544–3553 (1983).

Figure 1

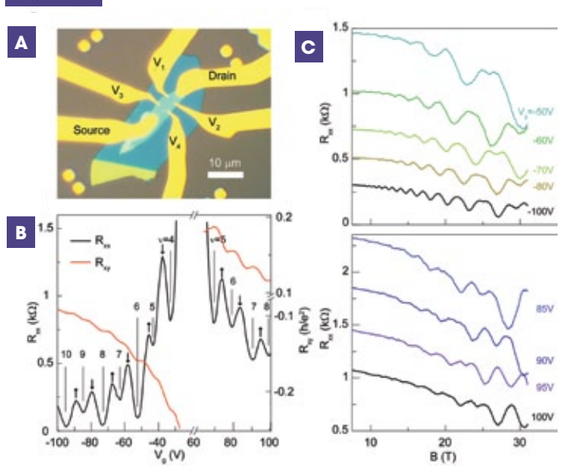

A, Optical image of our black phosphorus device with h-BN substrate. **B,** R_{xx} (black) and R_{xy} (red) measured as a function of V_g with magnetic field fixed at B = 31 T. LL index of each peak is indicated in the figure. Spin degeneracy is lifted at each LL and the arrows indicate the spin-up and spin-down LLs. **C,** R_{xx} as a function of magnetic field measured at varying gate voltages. SdH oscillations are observed for both holes (upper panel) and electrons (lower panel). Temperature is fixed at 0.3 K during the measurement.

Semiconductors

Earlier work on a 2D hole gas by Shayegan's group demonstrated that a parallel magnetic field which induces anisotropy in the hole Fermi contour also makes the Fermi contour of composite fermions (CFs) anisotropic. The reason for the Fermi contour anisotropy in both the hole and hole-flux CFs cases is the nonzero thickness of the quasi-2D system and the coupling of the carriers' out-of-plane motion to parallel field. The new experiment by the same group, which is described in this report, demonstrates the same effect in a 2D electron system and *electron*-flux CFs.

Fermi Contour Anisotropy of GaAs Electron-Flux Composite Fermions in Parallel Magnetic Fields

Kamburov, D.; Mueed, M.A.; Shayegan, M.; Pfeiffer, L.N.; West, K.W.; Baldwin, K.W. (Princeton U., Electrical Engineering)

Introduction

The composite fermion (CF) formalism elegantly describes the properties of interacting particles at high magnetic fields. In this picture, each electron pairs up with an even number of flux quanta to form CFs, which at even-denominator Landau level filling factors occupy a Fermi sea with a well-defined Fermi contour. The existence of a CF Fermi contour raises the question whether fermionization preserves any low-field Fermi contour anisotropy. To answer this fundamental question we determined, via measurements of commensurability oscillations, the $\nu = 1/2$ CF Fermi contour anisotropy induced by the application of in-plane magnetic field $B_{||}$.

Experimental

We studied 2D electrons confined to GaAs quantum wells (QWs) flanked on each side by undoped $Al_{0.24}Ga_{0.76}As$ barrier layers and Si δ-doped layers. Each sample has two perpendicular Hall bars covered with periodic gratings of negative electron-beam resist which, through the piezoelectric effect in GaAs, induce a periodic density modulation. We used SCM2 and the 31 T resistive magnets for measurements.

Results and Discussion

The magnetoresistance of patterned samples, shown in **Fig. 1(a)** exhibits a minimum whenever the $\nu = 1/2$ CF cyclotron orbit diameter becomes commensurate with the period of the density modulation. We deduce the effect of $B_{||}$ on the CF Fermi wave vector k^*_F by measuring the shift in the positions of the commensurability resistance minima along the two perpendicular arms of the L-shaped Hall as $B_{||}$ is applied. When transport is parallel to $B_{||}$ (along the [110] direction), the positions of the minima move away from $\nu = 1/2$ (Fig. 1(b)) while perpendicular to $B_{||}$ their shift is toward 1/2 (Fig. 1(c)).

The values of k^*_F along the two Hall bar directions, deduced from the positions of the magnetoresistance minima for each QW, reveal a severe CF Fermi contour distortion as a result of $B_{||}$ and indicate that the anisotropy depends on the QW width. Furthermore, they indicate that the Fermi contour areas remain nearly elliptical up to $B_{||} = 26$ T.

The strong quantitative dependence of the distortion on $B_{||}$ and on the QW width implies that the origin of this anisotropy is the coupling between $B_{||}$ and the out-of-plane motion of the CFs. It further suggests that besides its thickness, other parameters of the quasi-2D carrier system, such as the details of the band structure and effective mass, as well as the character of the Landau level where the CFs are formed, play important roles in determining the anisotropy of the CF Fermi contour in a strong $B_{||}$.

Acknowledgements

A portion of this work was performed at the National High Magnetic Field Laboratory, which is supported by National Science Foundation Cooperative Agreement No. DMR-1157490, the State of Florida, and the U.S. Department of Energy. We thank S. Hannahs, T. Murphy, and A. Suslov for technical help.

This work was supported by NSF, DOE, the Gordon and Betty Moore Foundation, and Keck Foundation.

References

1. Kamburov *et al.*, Phys. Rev. B **89**, 085304 (2014).
2. Kamburov *et al.*, Phys. Rev. Lett. **113**, 196801 (2014).
3. Kamburov *et al.*, Phys. Rev. B **90**, 235108 (2014).

Figure 1

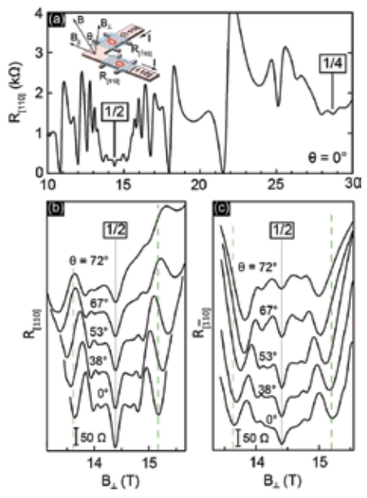

(A) Magnetoresistance without tilt showing strong commensurability features around $\nu = 1/2$ and 1/4.

(B), (C) With increasing $B_{||}$ (higher tilt angles θ) the commensurability minima move outward from $\nu = 1/2$ in the [110] direction and inward in the perpendicular direction.

Superconductivity – Basic

Here, the authors study the geometry of the Fermi surface of FeSe through Shubnikov de Haas oscillations, finding remarkable discrepancies with band structure calculations; namely, much smaller Fermi surface cross sectional areas and concomitant electron and hole counts. This indicates either a very pronounced role for the electronic correlations or Fermi surface reconstruction.

Anomalous Fermi Surface in FeSe Seen by Shubnikov-De Haas Measurements

Terashima, T.; Kikugawa, N.; Uji, S. (NIMS); Kiswandhi, A.; Choi, E.S.; Brooks, J.S.; (NHMFL); Kasahara, S.; Watashige, T.; Ikeda, H.; Shibauchi, T.; Matsuda, Y. (Kyoto Univ.); Wolf, T.; Böhmer, A.E.; Hardy, F.; Meingast, C.; Löhneysen, H.v. (KIT); Suzuki, M.-T.; Arita, R. (RIKEN)

Introduction

FeSe is an intriguing material. Despite the fact that FeSe is isoelectronic with $(FeAs)^{-1}$ planes of LaFeAsO or $BaFe_2As_2$, it does not order magnetically but becomes superconducting below T_c ~ 8 K [1]. Detailed research into its electronic structure is highly desirable, but such research was obstructed by difficulties in crystal growth. Recently, Böhmer et al. [2] have succeeded in growing single crystals of unprecedented quality. Using those crystals, we have performed Shubnikov-de Haas (SdH) measurements [3].

Experimental

We have performed standard four-contact resistance measurements using a 35-T resistive magnet and a ^{3}He or ^{3}He/^{4}He dilution refrigerator at the NHMFL, Tallahassee. The four measured samples have T_c of 8.9 – 9.2 K and RRR evaluated at 11 K of 28 – 32.

Results and Discussion

Figure 1(a) shows the magnetoresistance (red curve) for B // c and its oscillatory part (blue curve). Clear SdH oscillations are seen. **Figure 1(b)** shows Fourier transforms of SdH oscillations for B // c and two other field directions. We see four fundamental frequencies α, β, γ, and δ, and two harmonics 2α and 2β. We note that the observed frequencies are very small, corresponding to the orbit areas of 0.2 – 2.3 % BZ. The associated effective masses are in a range between 1.9 (α) and 7.2 me (γ) for B // c. These values result in very small effective Fermi energies 3.6 – 18 meV, which are to be compared with k_BT_c = 0.78 meV. Detailed analyses suggest that α and γ are the minimum and maximum frequencies of the quasi-two-dimensional electron cylinder, while β and δ are those of the hole one. The two cylinders are estimated to give a Sommerfeld coefficient of ~6 mJ/molK^2, which is in agreement with reported specific heat data [4] and hence suggests that the entire Fermi surface has been observed. The carrier number is estimated to be ~0.01 carriers per Fe. Those observations are in stark contrast to results of an LDA band-structure calculation, which predicts two electron and three hole cylinders and a carrier number of 0.17 carriers per Fe.

Conclusions

We have observed SdH oscillations in FeSe for the first time. The observed Fermi surface differs significantly from that predicted by the LDA calculation, which clearly needs further investigations.

Acknowledgements

A portion of this work was performed at the National High Magnetic Field Laboratory, which is supported by National Science Foundation Cooperative Agreement No. DMR-1157490, the State of Florida, and the U.S. Department of Energy. This work has been supported by Japan-Germany Research Cooperative Program, KAKENHI from JSPS and Project No. 56393598 from DAAD, and the "Topological Quantum Phenomena" (No. 25103713) KAKENHI on Innovative Areas from MEXT of Japan. JSB acknowledges support from NSF-DMR 1309146.

References

1. Hsu, F.-C., *et al.*, PNAS, **105**, 14262 (2008).
2. Böhmer, A.E., *et al.*, Phys. Rev. B **87**, 180505(R) (2013).
3. Terashima, T., *et al.*, Phys. Rev. B **90**, 144517 (2014).
4. Lin, J.-Y., *et al.*, Phys. Rev. B **84**, 220507(R) (2011).

Figure 1

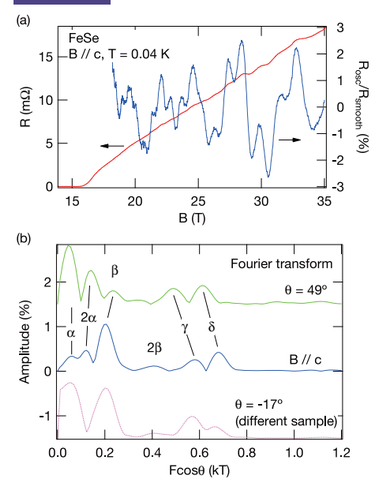

(A) Resistance in FeSe (red) and its normalized oscillatory part (blue) as a function of magnetic field for B // c. **(B)** Fourier transforms of SdH oscillations in FeSe.

Superconductivity – Basic

Through Nernst and Seebeck coefficient measurements the authors find evidence for a previously undetected hole-like Fermi surface (FS) pocket which would be consistent with an underlying charge density wave state.

Evidence for a Small Hole Pocket in the Fermi Surface of Underdoped $YBa_2Cu_3O_y$

Doiron-Leyraud, N.; René de Cotret, S.; Laliberté, F.; Hassinger, E.; Taillefer, L. (Université de Sherbrooke and CIFAR); Badoux, S.; LeBoeuf, D.; Vignolles, D.; Vignolle, B.; Proust, C. (LNCMI Toulouse); Ramshaw, B.J.; Bonn, D.A.; Hardy, W.N.; Liang, R. (University of British Columbia); Park, J.-H. (NHMFL)

Introduction

The phase diagram of the cuprates is shaped by ordered states and their identification is essential for understanding high temperature superconductivity. Evidence for a new state in cuprates recently came from two major developments. The observation of quantum oscillations and negative Hall effect in underdoped $YBa_2Cu_3O_y$ (YBCO) [1] showed that the Fermi surface is reconstructed at low temperature, implying a state with broken translational symmetry. More recently, charge-density-wave (CDW) modulations were observed in YBCO first by NMR [2], and then by x-ray diffraction [3]. Fermi-surface reconstruction and CDW modulations are two universal properties of underdoped cuprates, which begs the following question: Is the Fermi surface of YBCO compatible with a reconstruction by the observed CDW order?

Experimental

At the NHMFL, we have measured the Seebeck *(S)* and Nernst *(N)* coefficients of YBCO up to 45 T. As seen in Fig. 1a, at T = 2 K both *S* and *N* exhibit giant quantum oscillations (QO). At 18 K, these QO are damped, which reveals additional slow oscillations (Fig. 1b). In Fig. 1c, we see that the oscillations at 18 K are periodic in 1/*B*, with a frequency F_b = 95 T. The fast QO at 2 K have a main frequency F_a = 540 T, consistent with prior reports.

Results and Discussion

This slow frequency F_b was subsequently observed in the c-axis resistivity at the LNCMI in Toulouse. It was shown to bear all the key signatures of QO from a small, quasi-2D Fermi pocket: it obeys the Lifshitz-Kosevitch temperature dependence with a light mass of 0.45 m_0, and the field-angle dependence of F_b is close to 1/cosθ [4]. We therefore ascribe F_b to a hitherto overlooked part of the Fermi surface of YBCO, distinct from the larger electron pocket. To be consistent with the measured Seebeck coefficient in the field-induced normal state of YBCO as a function of doping [5], this Fermi pocket must be hole-like.

Conclusions

Our measurements show that the reconstructed Fermi surface of YBCO includes both electron and hole pockets. Calculations based on the measured CDW in YBCO [6] predict the Fermi surface shown in the inset of **Fig. 1b**, with one electron and two hole pockets whose sizes are consistent with our measurements. This agreement strongly supports the CDW scenario.

Acknowledgements

We acknowledge support from CIFAR, NSERC, FRQNT, CFI, and a Canada Research Chair. A portion of this work was performed at the National High Magnetic Field Laboratory, which is supported by National Science Foundation Cooperative Agreement No. DMR-1157490, the State of Florida, and the U.S. Department of Energy.

References

1. N. Doiron-Leyraud *et al.*, Nature 447, 565 (2007); D. LeBoeuf *et al.*, Nature 450, 533 (2007).
2. T. Wu *et al.*, Nature 477, 191 (2011).
3. G. Ghiringhelli *et al.*, Science 337, 821 (2012); J. Chang *et al.*, Nature Physics 8, 871 (2012).
4. N. Doiron-Leyraud *et al.*, Nature Communications 6, 6034 (2015).
5. F. Laliberté *et al.*, Nature Communications 2, 432 (2011).
6. A. Allais *et al.*, Nature Communications 5, 5771 (2014).

Figure 1

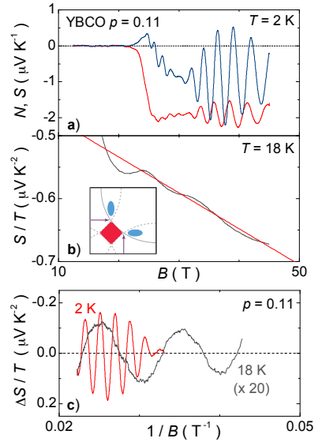

(A) Seebeck *(S)* and Nernst *(N)* coefficients of YBCO at a doping *p* = 0.11 for a temperature *T* = 2 K as a function of magnetic field. **(B)** *S/T* as a function of field at *T* = 18 K. Inset: Fermi surface reconstruction by CDW, showing one electron (red) and two hole (blue) pockets [6]. (C) Oscillatory part of *S/T* at *T* = 2 and 18 K, versus *1/B*.

Superconductivity – Basic

These specific heat experiments in YBCO extend measurements begun in previous years to lower dopings, confirming the existence of a residual linear-in-temperature electronic contribution to the specific heat in the superconducting phase at zero magnetic field throughout the underdoped regime of YBCO. This result is in sharp contrast to the popular belief in the literature that an electronic pocket emerges only in the charge-ordered phase, as the latter is destroyed at onset of superconductivity. Two significant experimental results directly evident in the data are: (1) this low-temperature electronic specific heat in the superconducting phase is confirmed to increase as the square root of magnetic field at two new dopings, consistent with prediction and previous reports for the d-wave superconducting state in YBCO; and (2) for the first time, there is observed a quantum phase transition at H'~10 tesla to a new superconducting phase deep in the zero-resistance regime (i.e. H' << Hc2) at these dopings. The nature of this transition is yet to be determined.

High Field Heat Capacity of Two Dopings of YBCO

Kemper, J.B.; Boebinger, G.S. (FSU, NHMFL/Physics); Bonn, D.; Hardy, W.N.; Liang, R. (CIAR and UBC, Physics)

Introduction

The experiments for 2014 focused on the field dependence of the absolute values of the low temperature heat capacity in the cuprate superconductors known as YBCO ($YBa_2Cu_3O_{6+\delta}$) δ=0.43 and 0.67. The goal was to explore the effect of field on the low-lying electronic excitations of the superconducting state. YBCO has been studied extensively in magnetic field, but specific heat is unique in tracking the total electronic density of states.

Experimental

All experiments took place at the DC field facility in the 35 tesla magnet in Cell 12, using the system D cryostat. The experimental instrumentation and technique were developed in-house. The measurement determines the heat capacity of a sample using thermometers that are calibrated at the NHMFL pulsed field facility to ensure high accuracy in all magnetic fields to 35T.

Results and Discussion

Over the course of three weeks of magnet time we confirmed the previous year's result that very underdoped YBCO (δ=0.40-0.49) shows an unexpected linear-in-field specific heat at low temperatures and highest fields. For δ=0.67, we observed specific heat well above the resistive transition, with new levels of precision for this material. Data analysis continues on data at this doping.

Conclusions

Specific heat measurements have found an unanticipated phase transition deep in the zero-resistance state of very underdoped YBCO. Measurements in 2014 have confirmed this transition at a second doping.

Acknowledgements

These measurements were made at the National High Magnetic Field Laboratory, which is supported by National Science Foundation Cooperative Agreement No. DMR-1157490, the State of Florida, and the U.S. Department of Energy. Work at the University of British Columbia was supported by the Natural Science and Engineering Research Council of Canada and the Canadian Institute for Advanced Research.

Figures

1

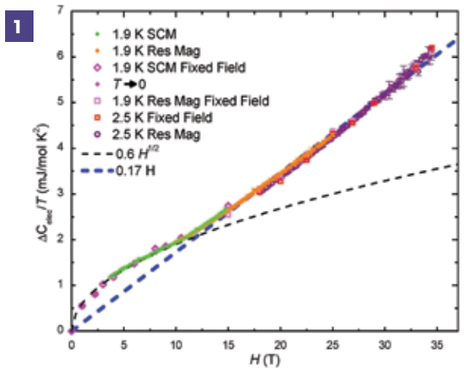

Previous year's result for δ=0.47 showing linear-in-field *(H)* electronic *C/T,* which is specific heat divided by temperature

2

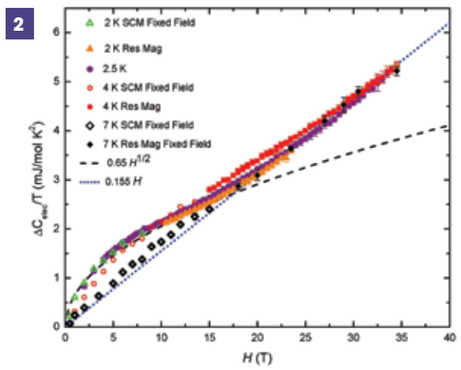

2014 result demonstrating a similar onset of linear-in-field behavior for δ=0.43.

Topological Matter

There has been enormous recent interest in materials which show three-dimensional Dirac-like disper-sions within the bulk, in contrast to topological insulators and graphene where the Dirac dispersions exist in only two dimensions. Xiong and co-authors measure the topological Dirac semimetal Na_3Bi and discover a large magnetoresistance that spans five decades without saturation all the way to 60 tesla. The magnetoresistance could potentially be linked to the lifting of the degeneracy of the Dirac node and the possible production of two Weyl nodes in strong magnetic fields.

Magnetotransport of the Dirac Semimetals Na_3Bi and Cd_3As_2

Xiong, J.; Liang, T.; Hirschberger, M.; Ong, N.P. (Dept of Physics, Princeton University)

Ultrahigh Mobility and Giant Magnetoresistance in Dirac Semimetals

We have investigated high-field transport in the two Dirac semimetals Na_3Bi and Cd_3As_2. In the Dirac semimetal, the bulk Dirac nodes are protected against gap formation by crystalline symmetry and time-reversal symmetry (TRS). An applied magnetic field is predicted to break TRS and split each Dirac node into Weyl nodes with opposite chirality, resulting in novel transport features. We have uncovered several anomalies in the magnetotransport properties of both Dirac semimetals. In related research, we have also investigated the dichalcogenide WTe_2 which has matched electron and hole pockets. At 4 K, the observed magnetoresistance (MR) is exceptionally large. In pulsed fields (60 T), the MR ratio attains values exceeding 10^5 without evidence of saturation.

Experiments

Hall and MR measurements on both Na_3Bi and Cd_3As_2 were performed in the 33 Tesla DC magnet at selected tilt angles of the field **H**. Using the pulsed field facilities at Los Alamos, we extended measurements in Cd_3As_2 to 65 T. In addition, the MR in WTe_2 was measured in pulsed fields to show the absence of saturation up to 65 T.

Results and Conclusions

1) A surprising result in the Dirac semimetal Cd_3As_2 is the observation1 that its mobility can reach values as high as 9 million cm^2/Vs in zero field (nearly comparable to MBE grown GaAs heterostructures). In applied **H**, the mobility is rapidly degraded, resulting in either an H-linear MR or H2 MR in ultrahigh-mobility samples. The high-field experiments confirmed the MR behavior. We were also able to reach the quantum limit (last Landau level) in a field of 40 Tesla.

2) In the Dirac semimetal Na_3Bi, we observed[2] a striking *H*-linear MR that extends up to 34 T. We also found that the Hall angle shows a step-function profile vs. *H*, which supports our inference that, in Dirac semimetal, the Dirac electrons are protected against backscattering in zero *H*. A finite *H* kills the protection presumably by breaking TRS.

3) In WTe_2, we showed[3] using pulsed fields that the giant MR ratio (~4,500 at 15 T) increases to values as high as 145,000 in pulsed fields up to 65 T (Fig. 1). Unlike in pure Bi or graphite, the MR shows no signs of saturation at large *H*.

Acknowledgements

A portion of this work was performed at the National High Magnetic Field Laboratory, which is supported by National Science Foundation Cooperative Agreement No. DMR-1157490, the State of Florida, and the U.S. Department of Energy.

The research is also supported by the Army Research Office (ARO W911NF-11-1-0379), a MURI grant on Topological Insulators (ARO W911NF-12-1-0461) and a MRSEC grant from the National Science Foundation (DMR 0819860).

References

1. Tian Liang, *et al.*, "Ultrahigh mobility and giant magnetoresistance in the Dirac semimetal Cd_3As_2," *Nature Materials*, in press. DOI: 10.1038/NMAT4143

2. Jun Xiong *et al.*, "Anomalous Conductivity Tensor in the Dirac semimetal Na_3Bi, arXiv:1502.06266

3. Mazhar N. Ali, *et al.* "Large Magnetoresistance in WTe_2," *Nature* **514**, 205 (2014). doi:10.1038/nature13763

Figure 1

A

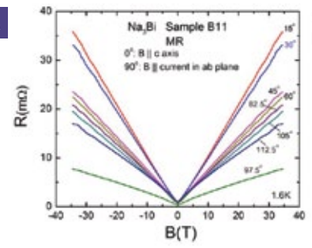

Striking H-linear MR observed in Na_3Bi.[2]

B

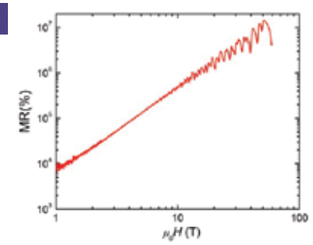

Non-saturating MR in WTe_2.[3]

Topological Matter

Despite the enormous theoretical and experimental interest in topological insulators, in which a single Dirac cone exists at the surface, obtaining a material with a true insulating bulk has proven to be an immense challenge. Here the authors claim that single crystals of $BiSbTeSe_2$ come very close to exhibiting a true insulating bulk. Importantly, the authors succeed in measuring quantum Hall plateaux characteristic of a two-dimensional electron gas of Dirac fermions without significant bulk contamination.

Observation of Topological Surface State Quantum Hall Effect in an Intrinsic Three-Dimensional Topological Insulator

Xu, Y. (Purdue Univ., Physics); Chen, Y.P. (Purdue Univ., Physics & ECE)

Introduction

A three-dimensional (3D) topological insulator (TI) is a novel quantum matter system with a gapped insulating bulk and a conducting surface hosting topologically-protected gapless surface states, where charge carriers are spin-helical massless Dirac fermions [1]. One of the most iconic electronic transport signatures predicted for such topological surface states (TSS) is a well-defined half-integer quantum Hall effect (QHE) in a magnetic field, where the surface Hall conductivities become quantized in units of $(1/2)e^2/h$ (e being the electron charge, h the Planck constant) concomitant with vanishing resistance.

In this work, we report observations of well-developed TSS QHE in $BiSbTeSe_2$ (BSTS), an intrinsic TI material where the bulk is highly insulating with negligible conductance [2].

Experimental

BSTS single crystal were synthesized in Purdue and then fabricated into bulk or thin flake devices for transport measurements, which were mostly performed in cell 9 with base temperature down to 350 mK and magnetic fields up to 31 T.

Results and Discussion

At low temperatures and high magnetic fields perpendicular to the top and bottom surfaces, we observe well-developed integer quantized Hall plateaus, where the two parallel surfaces each contribute a half integer e^2/h quantized Hall (QH) conductance, accompanied by vanishing longitudinal resistance. When the bottom surface is gated to match the top surface in carrier density, only odd integer QH plateaus are observed, representing a half-integer QHE of two degenerate Dirac gases.

Conclusions

Our intrinsic TI with TSS exhibiting half-integer QHE provides an excellent platform to pursue a plethora of exotic physics and novel device applications predicted for TIs, ranging from magnetic monopoles and Majorana particles to dissipationless electronics and fault-tolerant quantum computers.

Acknowledgements

A portion of this work was performed at the National High Magnetic Field Laboratory, which is supported by National Science Foundation Cooperative Agreement No. DMR-1157490, the State of Florida, and the U.S. Department of Energy. We also acknowledge support from DARPA MESO program (Grant N66001-11-1-4107).

References

1. Hasan, M.Z. & Kane, C.L., *Rev. Mod. Phys.*, **82**, 3045-3066 (2010).

2. Xu, Y., et al., *Nature Physics*, **10**, 956-963 (2014).

Figures

1

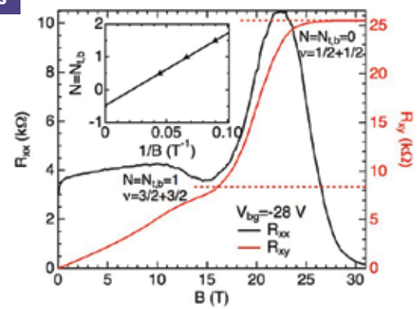

Magnetic field (B) dependence of R_{xx} and R_{xy} measured when top and bottom surfaces have the same carrier density. Inset shows the corresponding Landau level (LL) fan diagram. A linear fit gives intercept -0.5 on the N-axis, a signature of Dirac fermion.

2

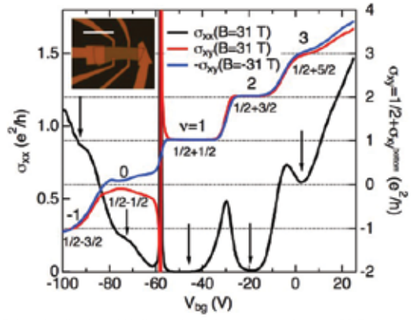

Extracted 2D longitudinal and Hall conductivities (σ_{xx} and σ_{xy} at 31 T along with $-\sigma_{xy}$ at -31T), in units of e^2/h. σ_{xy} shows well-developed integer QH plateaus where total filling factor equals 1/2 (from top surface) plus a half integer (from bottom surface). Inset shows a typical optical image of device on SiO_2/Si substrate with scale bar 25 μm.

Chemistry

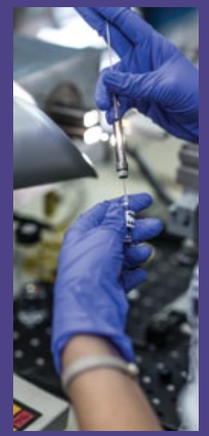

Life Sciences

Photos by: Dave Barfield

Chemistry

Iron is arguably the most important metal on the Earth, and also the most prevalent. It may exist in several oxidation states; in this case it was the +2 oxidation state that was investigated by HFEPR and Mossbauer. The magnetic results on new and original square-planar coordination geometry of Fe(II) will enrich our knowledge about the role iron plays in various chemical reactions.

A High-Spin Square-Planar Fe(II) Complex Stabilized by a Trianionic Pincer-Type Ligand

Pascualini, M.E.; Di Russo, N.V.; Thuijs, A.E. (UF, Chemistry); Ozarowski, A.; Stoian, S.A. (NHFML); Abboud, K.A.; Christou, G.; Veige, A.S. (UF, Chemistry)

Introduction

Molecular compounds featuring a central iron metal ion connected to four neighboring atoms that define a square and hold the metal in an essentially flat environment are rare. These compounds are of high interest not only because they have unique properties but also because they exhibit unexpected chemical behavior enabling them to mediate difficult chemical transformations. We have prepared such a compound using a pincer-like organic molecule that binds tightly to iron just like a crab grips its prey. Its electronic structure, i.e., the precise arrangement of electrons within the molecule, was determined using both Electron Paramagnetic Resonance (EPR) and nuclear gamma-resonance (Mössbauer) spectroscopy in magnetic fields of varying strengths and at different temperatures.

Experimental

High-frequency EPR spectra were recorded using a home-built spectrometer at the EMR facility of NHMFL. The instrument is a transmission-type device for which the microwaves were generated by a phase-locked oscillator. A superconducting magnet capable of reaching a field of 17 T was employed. Mössbauer spectra were recorded using an instrument fitted with a flow-type cryostat that had a built in 8 T superconducting magnet. This spectrometer allowed for recording variable-temperature spectra from 4.2 to 250 K in applied fields parallel to the incident γ-radiation from 0 to 8 T.

Results and Discussion

This investigation indicated the presence of an excess of electron density along the normal to the square formed by the four near-neighbors of the iron (see top Figure). Although such an electron density distribution at the iron site typically translates into a large electric field gradient (EFG) at the nucleus, the big surprise was the discovery of essentially no EFG. A theoretical investigation using Density Functional Theory (DFT) enabled a rationalization of this observation by showing that the large EFG generated by the iron electrons is essentially quenched by that generated by the four neighbors. This investigation also established only five populated spin states, i.e., the compound has a spin S = 2 ground state.

Conclusions

This work extends the set of known Fe(II) square-planar high-spin compounds beyond the limited FeO_4 motif, and presents the first high-field EPR and variable field/temperature Mössbauer characterization of this class of compounds.

Acknowledgements

ASV acknowledges UF and the NSF (CHE-1265993), for providing funding for this research. GC acknowledges the NSF (DMR-1213030). KAA acknowledges the NSF (CHE-0821346) for the purchase of X-ray equipment. Computational resources were provided by the University of Florida HPC Center. NVD is an HHMI International Student Research fellow. SAS is an NHMFL Jack E. Crow postdoctoral fellow.

Figures

1

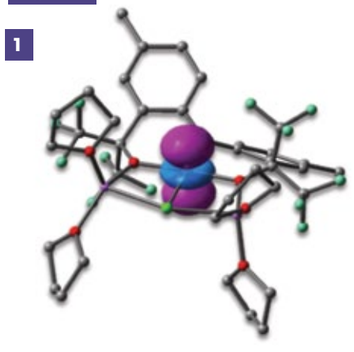

DFT predicted doubly-occupied orbital that determines the spatial arrangement of the excess electron density at the iron site.

2

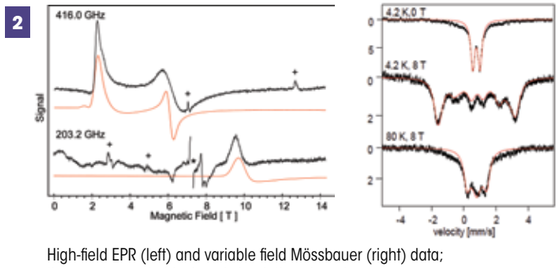

High-field EPR (left) and variable field Mössbauer (right) data; the spectra are in black and simulations in red.

Chemistry

Oxygenated compounds are formed when crude oil is environmentally modified after an oil spill. These compounds are problematic with gas chromatography, the traditional benchmark oil analytical method. Here, Fourier transform ion cyclotron resonance mass spectrometry reveals the scope of oxygenated modifications to the Macondo well-head oil after the Deepwater Horizon oil spill, and directs a targeted analyses by next generation two-dimensional gas chromatography.

Targeted Petroleomics: Analytical Investigation of Macondo Well Oil Oxidation Products from Pensacola Beach

Ruddy, B.M. (NHMFL, FSU, Chemistry); Huettel, M. (FSU, EOAS); Kostka, J.E. (Georgia Tech., Biology, Earth & Atmospheric Sciences); Lobodin, V.V.; Bythell, B.J.; McKenna, A.M. (NHMFL, Chemistry); Aeppli, C.; Reddy, C.M.; Nelson, R.K. (WHOI); Marshall, A.G. (NHMFL, FSU, Chemistry); Rodgers, R.P. (NHMFL, FSU)

Results and Discussion

Of the estimated 5 million barrels of crude oil released into the Gulf of Mexico from the Deepwater Horizon oil spill, a fraction washed ashore onto sandy beaches from Louisiana to the Florida panhandle. Here, we compare the detailed molecular analysis of hydrocarbons in oiled sands from Pensacola Beach to the Macondo wellhead oil (MWO) by electrospray (ESI) and atmospheric pressure photoionization (APPI) Fourier transform ion cyclotron resonance mass spectrometry (FT-ICR MS) to identify major environmental transformation products of polar, high molecular weight (C>25) "heavy ends" (high-boiling species) inaccessible by gas chromatography. The petrogenic material isolated from the Pensacola Beach sand displays greater than 2-fold higher molecular complexity than the MWO constituents, most notably in oxygenated species absent in the parent MWO. Surprisingly, the diverse oxygenated hydrocarbons in the Pensacola Beach sediment extracts were dominant in all ionization modes investigated, (±) ESI and (±) APPI. Thus, the molecular-level information highlighted oxygenated species for subsequent "targeted" analyses. First, time-of-flight mass spectrometry analysis of model compounds attributes the unusually large oxygen signal magnitude from positive electrospray to ketone transformation products (O1–O8 classes). Next, negative electrospray mass spectrometry reveals carboxylic acid transformation products. Two-dimensional gas chromatography with mass spectrometry analysis of anion-exchange chromatographic fractions unequivocally verifies the presence of abundant alkyl ketone fragments in sand extracts, and FT-ICR MS analysis reveals the distribution of high-boiling ketone, carboxylic, and higher numbered (3+) oxygen-containing transformation products too polar to be analyzed by gas chromatography. The results expand compositional coverage of oxygen-containing functionalities beyond the classic naphthenic acid type species to complex/mixed ketone, hydroxyl, and carboxylic acid classes of molecules that have been recently identified in produced water, emulsions, and petroleum production deposits.

Acknowledgements

The work was supported by the National Science Foundation (NSF) Division of Materials Research through DMR-11-57490, NSF Division of Chemistry through Rapid Grant CHE-1049753, the State of Florida, NSF grants OCE-1044939 and OCE-1057417, and BP/The Gulf of Mexico Research Initiative to the Deep-C Consortium.

References

1. Ruddy, B.M. et al., Energy Fuels, **28**, 4043-4050 (2014)

Figure 1

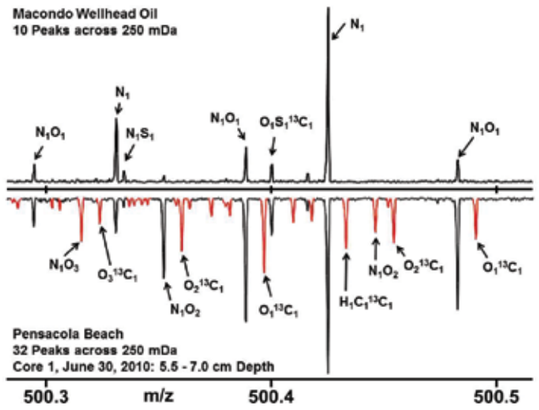

Positive ESI 9.4 T FT-ICR mass scale-expanded segment at nominal m/z 500 for (top) Macondo well oil (MWO) and (bottom) June 30, 2010 Pensacola Beach contaminant (5.5–7.0 cm depth). Contaminant species not present in MWO are shown in red. The higher compositional complexity can be more effectively visualized for high-resolution FT-ICR data through mass scale-expanded segments that span a fraction of a single nominal mass (0.2 Da at m/z 500). For positive ESI, 10 peaks are detected for the MWO (top) and 32 for the contaminated beach sediment extract (bottom), whereas no peaks ≥ 6σ are observed from either the environmental or the analytical blank across the same mass segment (data not shown). Peaks detected from the Pensacola Beach sand extracts but not detected from the MWO are highlighted in red and expose the primary source of the increased complexity as oxidation.

Chemistry

Complex mixtures, such as natural organic matter (NOM), require ultrahigh resolution mass spectrometers to resolve and identify isobaric overlaps, but are not able to differentiate between structural isomers. Here, hydrogen/deuterium exchange identifies the first gas-phase identification of isomeric separation of NOM coupled with reverse-phase chromatography prior to FT-ICR mass spectrometry.

Ion Molecule Reaction H/D exchange as a Probe for Isomeric Fractionation in Chromatographically Separated Natural Organic Matter

Stenson, A.C. (Univ.of South Alabama, Chemistry); Ruddy, B.M. (NHMFL, FSU, Chemistry); Bythell, B.J. (NHMFL)

Introduction

High-resolution mass spectrometry disperses and resolves analyte ions with far greater peak capacity than any chromatographic technique. Unfortunately, even the highest-resolution mass spectrometer cannot separate isomers. For the characterization of complex mixtures, tandem chromatography and MS techniques must be developed that combine isomeric separation with detailed compositional characterization. To develop such techniques, a means of identifying isomeric separation is required. Hydrogen/Deuterium exchange (HDX) is an attractive means to distinguish isomers because the ability to exchange hydrogen(s) depends critically on structure.

Experimental

Suwannee River Fulvic Acid was fractionated through a phenyl column [(X-BridgeTM, (3.5µm, 4.6 x 150mm)] as previously described[1]. For solution HDX experiments, both spray-solvent components were deuterated (D2O and ISP-d8). For in-cell, gas-phase HDX, isobars of interest were isolated through stored waveform inverse Fourier transform then exposed to ND3 collision gas for 120s at ≤ 3 x 10^{-7} Torr. The NHMFL's custom-built 9.4 Tesla FT-ICR mass spectrometer was used for all experiments.

Results and Discussion

As shown in **Figure 1**, isobaric resolution is maintained. Such resolution had not been possible in previous HDX studies without recent advances in FT-ICR MS.[2-3] The data furthermore show that compounds with the same elemental compositions eluting in different fractions do not necessarily exchange the same total number of H and do not have identical exchange efficiencies for any given exchange. Rather, late-eluting fractions and early-eluting fractions appear to have comparable exchange efficiencies; middle-eluting fractions, meanwhile, exchange with the highest efficiency.

Conclusions

The results encompass the first gas-phase H/D exchange results for fully resolved natural organic matter (NOM) isobars and the first direct evidence of isomeric separation of NOM through reversed-phase chromatography.

Acknowledgements

The authors would like to acknowledge John Quinn for assistance with the experimental setup and Dr. Chris Hendrickson for helpful discussions. Financial support from NSF EAR-0848635, NSF DMR-1157490, the State of Florida, and the University of South Alabama is also gratefully acknowledged.

References

1. Stenson, A.C., Environmental Science & Technology, **42**, 2060-2065 (2008).
2. Solouki, T., et al., Analytical Chemistry, **71**, 4719-4726 (1999).
3. Alomary, A., et al., Environmental Science & Technology, **34**, 2830-2838 (2000).

Figure 1

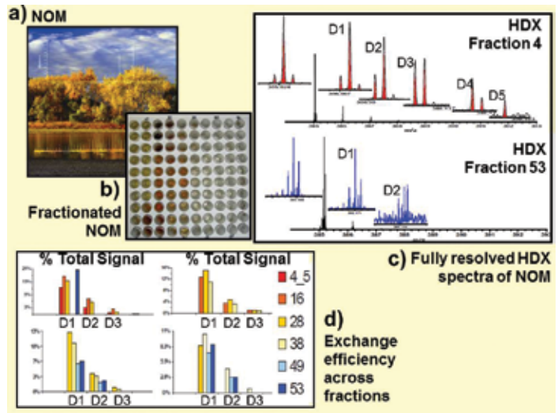

Chemistry

Low-barrier hydrogen bonds (LBHB) are hydrogen bonds where the potential energy barrier for translational proton transfer between two atoms is less than or equal to the zero-point energy. A low barrier hydrogen bond implies a very strong hydrogen bond compared to a regular hydrogen bond, based on decades of gas and condensed phase research centered on high-level theoretical computations. Here, ^{17}O NMR is used to directly measure the energetic in LBHB molecules (nicotinic acid) in the 900 MHz NMR coupled to the 3.2 mm custom-built MAS ^{1}H-X transmission line probe. Based on solid-state ^{17}O NMR, LBHB in nictonic acid is not particularly strong, and this observation challenges decades of research focused on the role of LBHB in enzyme catalysis.

Solid-State ^{17}O NMR Reveals Energetics of Breaking a Low-Barrier Hydrogen Bond

Lu, J. (Queen's U., Chemistry); Hung, I.; Gan, Z. (NHMFL); Kong, X.; Wu, G. (Queen's U., Chemistry)

Introduction

A low-barrier hydrogen bond (LBHB) refers to a HB in which the potential energy barrier for translational proton transfer between the two heavy atoms is close to or lower than the zero-point energy [1]. In general, the hydrogen atom in a LBHB is located near the mid-point between the two heavy atoms (e.g., O···H···O or O···H···N). A LBHB is commonly associated with a very short HB length (r_{OO} < 2.5 and r_{ON} < 2.6 Å) and thus in the literature a LBHB automatically implies a very strong HB. Although the existence of LBHBs in both gas and condensed phases has been firmly established, their role in enzyme catalysis has remained a controversy in the past 20 years [2]. The central issue is whether a LBHB is particularly strong as compared with a regular HB [3]. As direct experimental measurement of HB strength in condensed phases is rather difficult, most arguments are based on high-level computations. In this work, we used solid-state ^{17}O NMR to examine the hydrogen bonding energetics in nicotinic acid (NA) crystals.

Experimental

[1,2-$^{17}O_2$]NA was synthesized at the ^{17}O enrichment level of 20%. Variable-temperature (VT) ^{17}O MAS NMR spectra were obtained at 21.1 T (NHMFL) with a 900 MHz Bruker Avance console and a 3.2 mm home-built MAS ^{1}H-X transmission line probe. The sample temperatures under the 20-kHz MAS condition were calibrated using solid $Pb(NO_3)_2$.

Results and Discussion

The intermolecular HB in NA is shown in **Fig. 1.** While the O···N distance of 2.652 Å is relatively long in NA, the Fourier difference map clearly shows that the location of the H1 atom is shifted considerably towards the mid-point of the two heavy atoms, indicative of a LBHB. Both the 1D ^{17}O VT MAS and 2D EXSY spectra suggest that the carboxylate group of NA undergoes a rapid 180º-flip motion in the solid state, which interchanges the chemical environment of O1 and O2. An Arrhenius analysis of the VT ^{17}O NMR data yielded an activation energy (Ea) of 10.3 kcal mol^{-1} for this dynamical process. Interestingly, in order for the carboxylate group to flip, the LBHB must break. Our DFT calculations suggest that, in the absence of any HB, the rotational barrier of the carboxylate group in NA is 3.8 kcal mol^{-1}. Therefore, breaking the LBHB in NA requires as low as 6.5 kcal mol^{-1}. This value falls into the category of weak HBs (2-10 kcal mol^{-1}) [1].

Conclusions

We have shown that the LBHB in NA is not particularly strong. This observation provides strong experimental evidence challenging the concept that a LBHB must be a strong HB. The solid-state ^{17}O dynamic NMR approach provides unique information about HB energetics that are difficult to obtain with other experimental techniques.

Acknowledgements

This work was supported by NSERC of Canada. A portion of this work was performed at the National High Magnetic Field Laboratory, which is supported by National Science Foundation Cooperative Agreement No. DMR-1157490, the State of Florida, and the U.S. Department of Energy.

References

1. Jeffrey, G.A., An Introduction to Hydrogen Bonding, Oxford University Press, New York (1997).
2. Cleland, W.W., Biochemistry, **31**, 317-319 (1992); b) Gerlt, J.A., et al., J. Am. Chem. Soc., **115**, 11552-11568 (1993).
3. Perrin, C.L., Acc. Chem. Res., **43**, 1550-1557 (2010).

Figure 1

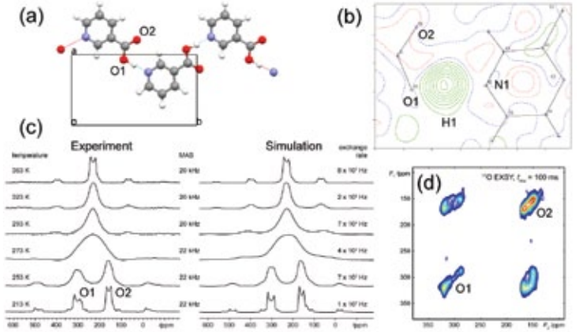

(A) NA molecules form hydrogen bonded zig-zag ribbons along the crystallographic *b* axis. **(B)** Electron density difference map of NA. **(C)** Experimental and simulated ^{17}O MAS spectra of [1,2-$^{17}O_2$]NA. **(D)** 2D EXSY spectrum of [1,2-$^{17}O_2$]NA at 236 K.

Chemistry

Metallofullerenes are part of the carbon family, and kin to what's popularly known as buckyballs. Buckyballs, or fullerenes, are hollow, soccer-ball-shaped, spherical cages that represent a basic form of carbon. The empty spaces in the fullerenes can trap metal atoms, resulting in metallofullerenes. Here, the ICR facility's 9.4 tesla FT-ICR mass spectrometer is applied to endohedral metallofullerenes, a highly valuable nanomaterial, to probe the mechanism of formation from metal-doped graphite.

Bottom-Up Formation of Endohedral Metallofullerenes is Directed by Charge Transfer

Dunk, P.W. (FSU, Chemistry); Mulet-Gas, M. (Universitat Rovira i Virgili, Spain, Physical & Inorganic Chemistry); Nakanishi, Y. (Nagoya University, Japan, Chemistry); Kaiser, N.K. (NHMFL, Chemistry); Rodríguez-Fortea, A. (Universitat Rovira i Virgili, Spain, Physical & Inorganic Chemistry); Shinohara, H. (Nagoya University, Japan, Chemistry); Poblet, J.M. (Universitat Rovira i Virgili, Spain, Physical & Inorganic Chemistry); Marshall, A.G.; Kroto, H.W. (FSU, Chemistry)

Introduction

An understanding of chemical formation mechanisms is essential to achieve effective yields and targeted products. One of the most challenging endeavors is synthesis of molecular nanocarbon. Endohedral metallofullerenes are of particular interest because of their unique properties that offer promise in a variety of applications, for example, biomedicine and photovoltaics. Nevertheless, the mechanism of formation from metal-doped graphite has largely eluded experimental study because harsh synthetic methods are required to obtain these metal-bearing nanoscale carbon cages.

Experimental

Here, we report bottom-up formation of monometallofullerenes under core synthesis conditions.

Results and Discussion

We find that charge transfer is a principal factor that guides formation, based on characterization of metallofullerenes with virtually all available elements of the periodic table. **Figure 1** shows that formation distributions of "magic numbered" cage sizes for endohedral metallofullerenes can differ substantially from those for empty cages. These results could enable production strategies that overcome long-standing problems that hinder current and future applications of metallofullerenes.

Acknowledgements

A portion of this work was performed at the National High Magnetic Field Laboratory, which is supported by National Science Foundation Cooperative Agreement No. DMR-1157490, the State of Florida, and the U.S. Department of Energy. P.W.D and H.W.K gratefully acknowledge support from the Florida State University Research Foundation. Additional support from the Spanish Ministerio de Ciencia e Innovación (CTQ2011-29054-C02-01) and Generalitat de Catalunya (2014SGR-199 and XRQTC) is acknowledged. M.M.-G. thanks the Spanish Ministerio de Ciencia e Innovación for a predoctoral fellowship (BES-2012-054018)

References

1. Dunk, P.W., *et al.*, Nature Commun., **5**, 5844 (8 pp.) (2014). DOI: 10.1038/ncomms6844 |www.nature.com/naturecommunications.

Figure 1

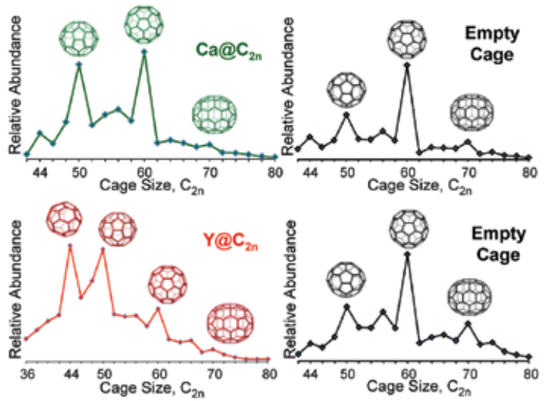

Cluster cations formed by laser evaporation of metal-doped graphite for selected elements of Group II (top) and Group III (bottom) metals with corresponding $M@C_{2n}$ and C_{2n} distributions. Positive ions are representative of neutral distributions. $M@C_{44}$ (M = metal) contains four sets of triple sequentially fused pentagons, $M@C_{50}$ exhibits five sets of double fused pentagons, and all pentagons are isolated for $M@C_{60}$.

Chemistry

This report describes a way to estimate giant axial anisotropy that occurs in certain high-spin nickel(II) coordination complexes. These complexes are of importance because of single-molecule magnet behavior expected from them, and a determination of their magnetic anisotropy is crucial for understanding and modeling their properties.

High-Field EPR Studies of Single-Ion Magnets with Giant Axial Magnetic Anisotropy

Marriott, K. (University of Glasgow, Chemistry); Bhaskaran, L. (MagLab and FSU, Physics); Hill, S. (MagLab and FSU, Physics); Murrie, M. (University of Glasgow, Chemistry)

Introduction

The motivation behind this project involves designing new single-ion single-molecule magnets (SI-SMMs) with giant magnetic anisotropies, particularly trigonal bipyramidal (TBP) Ni^{II} complexes with orbitally degenerate ground states.[1] However, such species are highly susceptible to Jahn-Teller-type distortions that lift the orbital degeneracy, thereby ultimately limiting the anisotropy. To this end, $[Ni(Hdabco)(dabco)Cl_3]$ and $[Ni(Me\text{-}dabco)_2Cl_3]$ were synthesized using the rigid dabco (= 1,4-diazabicyclo[2.2.2]octane) ligand in the hope of suppressing these Jahn-Teller effects.[2] High-field EPR studies then play a crucial role for precise elucidation of the spin Hamiltonian parameters which describe the magnetic anisotropy.

Experimental

Multi-frequency, low temperature EPR measurements based on a cavity perturbation technique were performed in the EMR and DC facilities in magnetic fields to 35 T. The sample was first placed in a rotating cavity to obtain the required orientation of the single-crystal with respect to the applied field.

Results and Discussion

Oriented single-crystal high-field EPR measurements were successfully performed at 4.2 K on the spin S = 1 trigonal bipyramidal (TBP) $[Ni(Me\text{-}dabco)_2Cl_3]$ complex. Multiple resonances were observed at a frequency of 81 GHz, of which a single peak shifts rapidly to magnetic fields of 35 T and beyond over a very narrow angle range, as seen in **Fig. 1(a)**. An analysis of the frequency dependence of this peak with the field applied in the hard plane [**Fig. 1(b)**] suggests a huge easy-axis anisotropy with a zero-field-splitting (zfs) parameter, $|D| > 300\ cm^{-1}$, associated with first order spin-orbit coupling. This value is considerably larger than previously reported for a Ni^{II} TBP complex,[1] and is thought to be due to the rigidity of the ligand that prevents Jahn-Teller type effects that can reduce D. This is confirmed by a small value of the rhombic parameter, $|E| = 0.15\ cm^{-1}$ [**Fig. 1(b)**, low-field intercept].

Conclusions

High-field EPR measurements provide very strong spectroscopic evidence for a huge easy-axis anisotropy in the TBP $[Ni(Me\text{-}dabco)_2Cl_3]$ complex, which maintains an orbitally degenerate ground state. These studies are important in terms of realizing the ultimate goal of molecular Ni^{II} nanomagnets with increased magnetic anisotropies and, therefore, higher blocking temperatures.

Acknowledgements

The UK Engineering and Physical Sciences Research Council are thanked for financial support (grant # EP/K033662/1). Work performed at the MagLab was supported by the NSF (DMR-1157490 and DMR-1309463) and the State of Florida.

References

1. Ruamps, R., *et al.*, J. Am. Chem. Soc., **135**, 3017-3026 (2013).
2. Gruden-Pavlovic, M., *et al.*, Chem. Sci., **5**, 1453-1462 (2014).

Figure 1

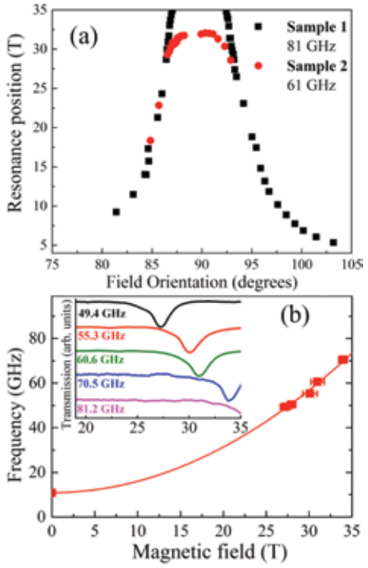

(A) Angle dependence plots of the EPR peak position for two samples at the indicated frequencies. **(B)** Frequency vs field plot, with the field in the molecular hard plane; the inset shows represented transmission spectra.

Geochemistry

This presents the first study of molecular transformations that occur to oil contamination that was released into the environment. Here, samples collected from the parent spilled heavy oil and rock scrapings collected up to 617 days later were analyzed by ultrahigh resolution FT-ICR MS to catalogue the chemical transformations that occur with extent of weathering. Specifically, this study reveals the formation of highly condensed, aromatic oxygen-containing compounds that remain environmentally persistent.

Molecular Evidence of Heavy-Oil Weathering Following the M/V *Cosco* Busan Spill: Insights from Fourier Transform Ion Cyclotron Resonance Mass Spectrometry

Lemkau, K.L. (MIT/WHOI); McKenna, A.M.; Podgorski, D.C.; Rodgers, R.P. (NHMFL, Chemistry); C.M. Reddy (WHOI)

Results and Discussion

Recent studies have highlighted a critical need to investigate oil weathering beyond the analytical window afforded by conventional gas chromatography (GC). In particular, techniques capable of detecting polar and higher molecular weight (HMW; > 400 Da) components abundant in crude and heavy fuel oils (HFOs) as well as transformation products. Here, we used atmospheric pressure photoionization Fourier transform ion cyclotron resonance mass spectrometry (APPI FT-ICR MS) to identify molecular transformations in oil-residue samples from the 2007 M/V Cosco Busan HFO spill (San Francisco, CA). Over 617 days, the abundance and diversity of oxygen-containing compounds increased relative to the parent HFO, likely from bio- and photodegradation. HMW, highly aromatic, alkylated compounds decreased in relative abundance concurrent with increased relative abundance of less alkylated stable aromatic structures. Combining these results with GC-based data yielded a more comprehensive understanding of oil spill weathering. For example, dealkylation trends and the overall loss of HMW species observed by FT-ICR MS has not previously been documented and is counterintuitive given losses of lower molecular weight species observed by GC. These results suggest a region of relative stability at the interface of these techniques, which provides new indicators for studying long-term weathering and identifying sources.

Acknowledgements

This work was supported by WHOI academic program funds, the Coastal Ocean Institute, the Richard and Rhoda Goldman Fund, the Ocean Ventures Fund and NSF grants EAR-0950670 and OCE-0960841. National High Magnetic Field Laboratory work was supported by NSF Division of Materials Research through DMR-06-54118, NSF CHE-10-49753 (RAPID), and the State of Florida, BP/Gulf of Mexico Research Initiation through the Deep-C Consortium.

References

1. Lemkau, K.L., *et al.*, Environ. Sci. Tech., **48,** 3760-3767 (2014)

Figure 1

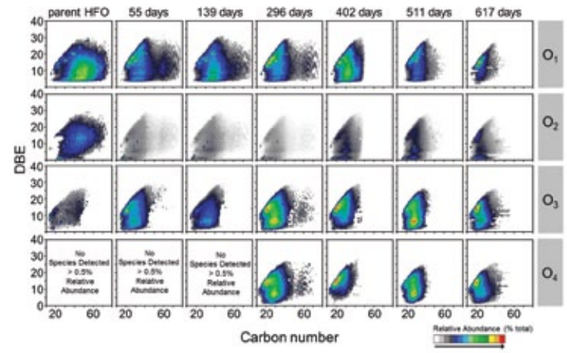

Isoabundance-contoured plots of double bond equivalents (DBE) versus carbon number for the O_1 – O_4 heteroatom classes (shown on right) for the parent HFO and field samples collected from 55 to 617 days postspill. Each compositional image is normalized to the most abundant species within that heteroatom class for that sample. Compounds that contain one oxygen atom (O_1) showed no overall shift in average DBE (14 in both the parent and HFO and after 617 days) but carbon number decreased by an average of 19 carbons per molecule. A bimodal distribution was observed in the O2 class with compounds with 2 DBE corresponding to naphthenic acids (naturally occurring alkyl-substituted saturated cyclic and noncyclic carboxylic acids). The decrease in average carbon number is less prominent in the O_3 and O_4 classes than in other classes, with average carbon number decreasing only by 5 for the O_3 class. These newly formed, highly oxygenated compounds are relatively resistant to degradation, comprised of mixed phenol, ketone and carboxylic acid species, and likely correspond to compounds formed through the biotic and abiotic oxidation of native HFO compounds.

Geochemistry

The more than 85,000 resolved and identified mass spectral peaks in a single mass spectrum of natural oil seep deposition represent the most extensive molecular deconvolution of an organic mixture to date, and establish a new world record for the ICR user facility. The highest achieved broadband resolving power ($m/\Delta m_{50\%}$ at m/z 500) and parts-per-billion mass error combined with isotopic fine structure confirm the first direct molecular characterization of vanadyl and nickel porphyrins in the same sample.

Unprecedented Ultrahigh Resolution FT-ICR Mass Spectrometry and Parts-Per-Billion Mass Accuracy Enable Direct Characterization of Nickel and Vanadyl Porphyrins in Petroleum from Natural Seeps

McKenna, A.M. (NHMFL, Chemistry); Williams, J.T. (NHMFL, Geochemistry); Putman, J.C. (NHMFL, FSU, Chemistry); Aeppli, C.; Reddy, C.M. (WHOI); Valentine, D.L. (Univ. California Santa Barbara, Earth/Marine Science); Lemkau, K.L. (Univ. California Santa Barbara, Marine Science); Kellerman, M.Y. (Univ. California Santa Barbara, Earth Science); Savory, J.J.; Kaiser, N.K.; Marshall, A.G. (NHMFL, FSU, Chemistry); Rodgers, R.P. (NHMFL, Chemistry)

Results and Discussion

The most abundant and problematic metal compounds in crude oil exist as organic complexes of vanadium and nickel in porphyrin structures derived from biological molecules (chlorophyll and heme), the first petroleum biomarkers discovered by Alfred Treibs in the early 1930s.[1] Detailed characterization of the type and structure of porphyrins is critical for development of petroleum upgrading processes, but also link crude oil to source rock conditions. Because petroporphyrins concentrate in heavy oils, direct characterization challenges routine analytical techniques due to the increased complexity associated with heavy crudes. Atmospheric pressure photoionization (APPI) Fourier transform ion cyclotron resonance mass spectrometry (FT-ICR MS) provides ultrahigh resolving power ($m/\Delta m_{50\%}$ > 1,000,000 at m/z 500) and sub-ppm mass error (<50 ppb) required to identify nickel porphyrin isotopes for unambiguous elemental composition assignment. We also report the first simultaneous identification and categorization of both vanadyl and nickel porphyrins in the same sample, without prior sample fractionation. More than 85,000 mass spectral peaks are resolved and identified in a single mass spectrum, and represent the most extensive molecular deconvolution of an organic mixture characterized to date.

Figure 1

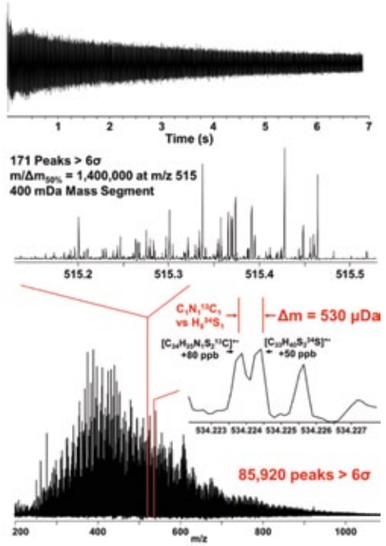

Broadband positive-ion APPI FT-ICR mass spectrum for an *Il Duomo* asphalt volcano sample. The achieved resolving power $m/\Delta m_{50\%}$ = 1,400,000 at *m/z* 515 enables resolution of 85,920 mass spectral peaks, each with magnitude greater than 6σ of baseline rms noise (*m/z* 200-1100) with a mass distribution centered at m/z 400. The mass scale-expanded segment at *m/z* 515 shows ~171 peaks. The theoretical resolving power required to separate two equally abundant species that differ in mass by ~548 μDa at 9.4 tesla is 890,000. The presently achieved resolving power ($m/\Delta m_{50\%}$ = 1,400,000 at *m/z* 515) enables separation of species that differ in mass by $C_1N_1{}^{13}C_1$ versus $H_5{}^{34}S_1$, both of nominal mass 39 Da, and differing in mass by 530 μDa—i.e., less than the mass of an electron (548 μDa). To the best of our knowledge, this mass spectrum represents the most peaks resolved and identified in a single spectrum of any kind, and represents the highest broadband resolving power for any petroleum mass spectrum, and emphasizes the need for ultrahigh resolving power achievable only by FT-ICR MS sufficient to separate isobaric overlaps prevalent in complex seep samples.

Acknowledgements

This work was supported by NSF Division of Materials Research through DMR-1157490, NSF Division of Chemistry through Rapid Grant CHE-1049753, NSF awards CHE-1016942, CHE-1019193, OCE-0961725 and EAR-0950600, BP/The Gulf of Mexico Research Initiative to the Deep-C Consortium, Florida State University and the State of Florida.

References

1. McKenna, A.M. *et al.*, Energy Fuels., **28**, 2454-2464 (2014)

Geochemistry

This report describes the effect of the Deepwater Horizon oil spill on the mercury levels in fish. Some species, like amberjack, show significant increase in Hg concentration. This increase is associated with a shift to more pelagic, higher trophic feeding regimes. Hg in amberjack closer to the DWH wellhead exhibit lower photoreduction attributable to the proximity to the Mississippi River. The significance of this study is that it shows that the oil spill had a secondary effect on mercury cycling but that the effect is not uniform for each fish species.

Using Mercury (Hg) Stable Isotopic Composition to Investigate the Deepwater Horizon Oil Spill Impact on Hg levels of Greater Amberjack *(Seriola dumerili)* and Two Species of Eels *(Ophichthus rex and Synaphobranchus oregoni)* in the Northern Gulf of Mexico

Harper, A.R. (FSU, EOAS); Perrot, V. (NHMFL); Chanton, J.P. (FSU, EOAS); Landing, W.M. (FSU, EOAS); Salters, V.J.M., (NHMFL and FSU, EOAS)

Introduction

The large input of organic material from the Deepwater Horizon oil spill resulted in local scale low-oxygen conditions [1] that could promote the formation of monomethylmercury (MMHg) and, based on our research, has increased the mercury levels in some fish **(Fig.1).** Light stable isotope analyses of carbon, nitrogen, and sulfur was employed to assess feeding ecologies of those species exhibiting higher MMHg concentrations following the oil spill. Using δ^{202}Hg and Δ^{199}Hg to distinguish Hg sources in fishes, we compared greater amberjack, an epibenthic and widely distributed fish species, from impacted and non-impacted areas in the Northern Gulf of Mexico. We also used two species of deepwater eels as geochemical indicators of mercury cycling at depth. Cutthroat eels (CTE) are common at depths greater than 1,000 meters while the larger king snake eels (KSE) are found in shallow slope habitats.

Experimental

Light stable isotopes of carbon, nitrogen, sulfur and mercury concentrations and isotopes were assessed in the muscle tissues. Carbon (δ^{13}C) and nitrogen (δ^{15}N) isotope values were obtained using a Finnigan MAT Delta PLUS XP stable isotope ratio mass spectrometer (IRMS). Mercury isotope ratios were collected using the Thermo Neptune™ multicollector inductively coupled plasma mass spectrometer (MC-ICP-MS) with a CETAC HGX-200 hydride generator as the sampling introduction system. Concentration analysis of MMHg and inorganic Hg (iHg) species was conducted using a Tekran 2700 Methyl Mercury Analysis System (EPA Method 1630). All above mentioned analysis took place at the National High Magnetic Field Laboratory in Tallahassee, Florida. Sulfur isotope (δ^{34}S) ratios were determined at the Stable Isotope Core Laboratory, Washington State University.

Results and Discussion

Reef fish species exhibiting significantly higher post-spill Hg loads rely more heavily on pelagic prey items while consuming a more restricted, less varied diet than pre-spill cohorts as indicated by muscle δ^{13}C and δ^{34}S. Enriched post-spill tissue δ^{15}N suggests higher trophic feeding, perhaps due to a limitation of smaller prey items. Mercury in amberjacks from the impacted area has undergone a lower degree of photoreduction (mean Δ^{199}Hg = 0.94 ± 0.15‰) than that from the unaffected area (Δ^{199}Hg = 1.36 ± 0.32‰; $p < 0.0001$) **(Fig. 2)**. Reduced photoreduction is likely caused by impaired photochemistry near the Mississippi River plume (close to the affected area) by the delivery of particulate and suspended organic material which limits light penetration. Both eel species maintain high mercury concentrations (KSE THg = 4.42 ± 3.42 ppm; CTE THg = 5.11 ± 2.90 ppm) despite the vast size difference between the two species (KSE total length = 145 ± 43 cm; CTE TL = 56 ± 9 cm) and apparent lower trophic feeding by the cutthroat eel, as indicated by their light δ^{13}C and δ^{15}N signatures. Mercury isotope analysis of eel muscle revealed that the mercury source at depth (+1,000) has undergone a higher degree of photodegradation than the mercury ingested by KSE **(Fig. 3)** suggesting sedimentation has transported Hg from shallow waters to the deep ocean.

Conclusions

Reef fish species exhibiting higher MMHg concentrations after the oil spill underwent and shift in feeding ecology and

CONTINUED ON NEXT PAGE

rely more heavily on larger, pelagic prey items. MMHg isotopes in amberjacks closer to DWH wellhead suggest a lower degree of photodemethylation, likely due to increased turbidity. Deep sea cutthroat eels are exposed to a MMHg source which is more photodegraded than slope dwelling snake eels, highlighting the importance of sedimentation events such as MOSSFA (Marine Oil Snow Sedimentation and Flocculent Accumulation) as a delivery mechanism of Hg to the deep sea.

Acknowledgements

This research was performed at the National High Magnetic Field Laboratory, supported by National Science Foundation Cooperative Agreement No. DMR-1157490, the State of Florida, and the U.S. Department of Energy. In addition, the Deep-Consortium, with the Gulf of Mexico Research Initiative, provided funding for this research.

References

1. Kessler, J.D., et al, Science, **331**, 312-315 (2011).

Figures

1

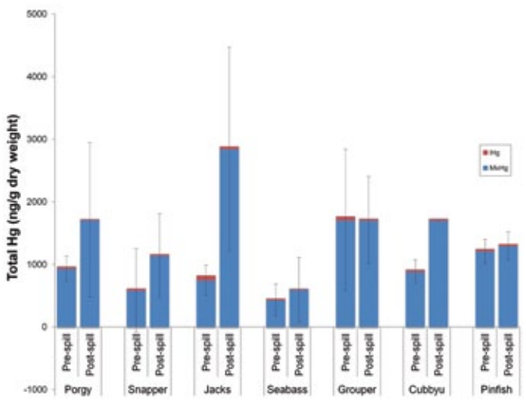

Mercury concentrations of pre-spill (collected 2007-09) and post-spill (collected 2012) fish species of similar lengths and $\delta^{13}C$, $\delta^{15}N$, and $\delta^{34}S$ signatures.

2

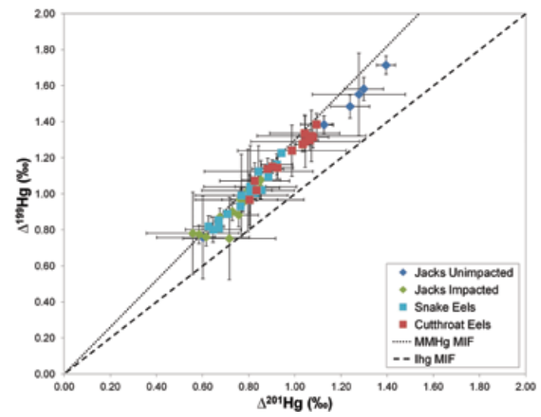

Hg isotopes in amberjacks closer to the DWH well-head has undergone a lower degree of photodemethylation.

3

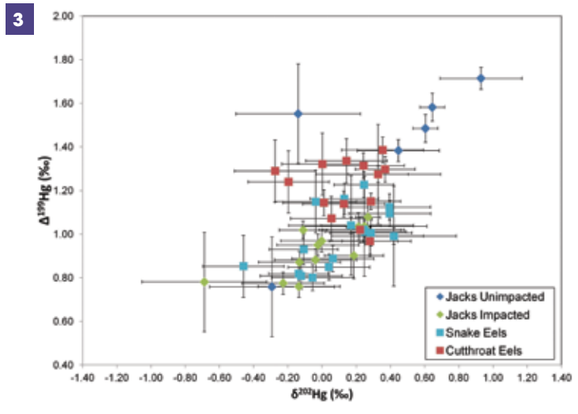

Cutthroat eel $\Delta^{199}Hg$ indicate Hg source underwent higher degree of photoreduction than shallower snake eels.

Magnetic Resonance Technique Development

In diffusion-weighted MRI studies of neural tissue, the classical diffusion model assumes the statistical features of Brownian motion and predicts a monoexponential signal decay. However, there have been numerous reports of signal decays that are not monoexponential, particularly in the white matter. Here, we extend this work via a new, fractional order diffusion model for the NMR propagator, p(q,Δ) and the spectral entropy H(q,Δ).

Entropy as a Measure of Non-Gaussian Diffusion in Fixed Rat Brain Tissues

Magin, R.L. (University of Illinois at Chicago, Bioengineering); Ingo, C. (University of Illinois at Chicago, Bioengineering); Ye, A. (University of Illinois at Chicago, Bioengineering); Colon-Perez, L. (University of Florida, Gainesville, Physics); Mareci, T.H. (University of Florida, Gainesville, Biochemistry)

Introduction

In diffusion-weighted MRI studies of neural tissue, the classical diffusion model assumes the statistical features of Brownian motion and predicts a monoexponential signal decay. However, there have been numerous reports of signal decays that are not monoexponential, particularly in the white matter. Here, we extend this work via a new, fractional order diffusion model for the NMR propagator, $p(q,\Delta)$ and the spectral entropy $H(q,\Delta)$.

Experimental

In this study we examined water diffusion in heterogenous white matter (WM) and homogenous gray matter (GM) regions of a fixed rat brain using a modified Pulsed Gradient Stimulated Echo pulse sequence on a Bruker spectrometer (17.6 T, 750 MHz, 89 mm bore) located in the Advanced Magnetic Resonance Imaging and Spectroscopy Facility of the National High Magnetic Field Laboratory at the McKnight Brain Institute of the University of Florida, Gainesville.

Results and Discussion

In white and gray matter regions, the Mittag-Leffler function (MLF) and entropy parameters demonstrated excellent contrast reflecting the specific choice of weighting on q and Δ **(Fig. 1)**. The MLF parameter, α, separated the central corpus callosum, the thalamus, the cerebellum, and the cerebral cortex more clearly and with less noise than the parameter, β. The apparent diffusion coefficient, $D_{1,2}$ and the entropy, H(q,Δ), distinguished the entire cerebral cortex, more clearly than the unit preserving parameters τ and μ.

Conclusions

We demonstrate that fractional order parameters and entropy parameters can serve as biomarkers for morphology in fixed neural tissue. We propose that these parameters, α, β and H(q,Δ), have the potential as biomarkers for morphology in neural tissue

Acknowledgements

A portion of this work was performed at the National High Magnetic Field Laboratory, which is supported by National Science Foundation Cooperative Agreement No. DMR-1157490, the State of Florida, and the U.S. Department of Energy.

References

1. Metzler, R. and Klafter, J. Phys Rep. **39(1)**:1-77 (2000).
2. Ingo, C., et al., Magnetic Resonance in Medicine, **71(2)**: 617-627 (2014).

Figure 1

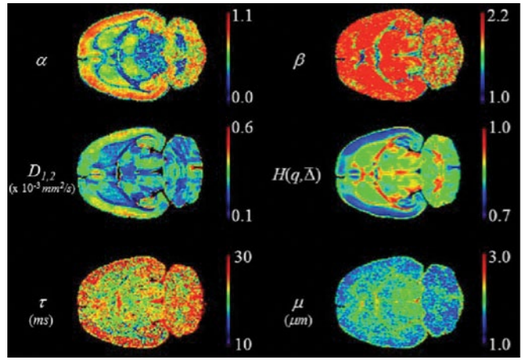

MLF and entropy parameter maps for a constant Δ = 17.5 ms experiment (q varied from 40 to 190 mm^{-1}). The α and β maps reflect temporal and topological features of the propagator, $p(q,\Delta)$, while the spectral entropy, $H(q,\Delta)$, combines both into a smooth measure of tissue complexity. The calculated apparent diffusion coefficient also shows excellent contrast, but not the unit preserving parameters τ and μ.

Magnetic Resonance Technique Development

Dynamic Nuclear Polarization (DNP) can enhance NMR sensitivity by more than an order of magnitude. Bi-radical agents such as TOTAPOL in a frozen glass matrix is usually used for enhancing nuclear polarization. This Highlight reports spin-labeled lipid molecules as a DNP enhancing agent. The new agent produces higher enhancement and is particularly useful for DNP applications with lipid and membrane proteins.

Published: Smith, A.N.; Caporini, M.A.; Fanucci, G.E. and Long, J.R. Angew. Chem. Int. Ed., 54, 5, 1542-1546 (2015)

A Method for Dynamic Nuclear Polarization Magic Angle Spinning NMR of Membrane Proteins

Smith, A.N. (U. of Florida, Chemistry); Caporini, M.A. (Bruker Biospin Corp.); Fanucci, G.E. (U. of Florida, Chemistry); Long, J.R. (U. of Florida, Biochemistry & Molecular Biology)

Introduction

Dynamic nuclear polarization (DNP) MAS ssNMR has the potential to enhance NMR signals by orders of magnitude and to enable NMR characterization of proteins which are inherently dilute, such as membrane proteins. In this work we demonstrate that spin labeled lipid molecules (SL-lipids), when utilized as the polarizing agents, lead to large and relatively homogeneous DNP enhancements throughout the lipid bilayer and to an embedded lung surfactant mimetic peptide, KL_4. Specifically, DNP MAS ssNMR experiments at 600 MHz/395 GHz on KL_4 reconstituted in liposomes containing SL-lipids reveal DNP enhancement values over two times larger for KL_4 compared to liposome suspensions containing the biradical TOTAPOL. These findings suggest an alternative sample preparation strategy for DNP MAS ssNMR studies of lipid membranes and integral membrane proteins.

Experimental

Proteoliposomes were made by mixing the lipids in chloroform (1:1 mole ratio DPPC-d_{62}:POPG) with the appropriate amount of KL_4 in metha¬nol for a 1:50 peptide to lipid ratio, evaporating the solvents, resuspending the lipid film in cyclohexane, and lyophilizing the sample to ensure a dry, solvent-free lipid powder. The SL-lipids TEMPO-PC and 5-Doxyl PC were mixed in with DPPC-d_{62} and POPG as chloroform solutions for the SL-lipid sample. Proteoliposomes were formed by hydrating the lipids in BisTris buffer pH 7.4 90:10 (v/v) D_2O:H_2O (SL-lipid sample) or 60:30:10 (v/v/v) glycerol-d_8:D_2O:H_2O containing TOTAPOL (TOTAPOL sample) followed by multiple freeze/thaw cycles. Proteoliposomes were pelleted to remove excess buffer and packed into 3.2 mm sapphire rotors via centrifugation. All ^{13}C CP MAS DNP ssNMR experiments were carried out in the NMR User Facility of the NHMFL using a Bruker 600 MHz/ 395 GHz DNP Avance spectrometer equipped with a 3.2 mm DNP MAS HCN probe. Samples were spun at 5 kHz, ~ 100 K and irradiated with ~ 11 W of gyrotron output power.

Table 1

Resonance	Measured Enhancement	
	SL-lipids	TOTAPOL
$^{13}C'$-L12 KL4 Peptide	8.9	3.7
Glycerol Backbone	6.5	3.4
Carbonyls	8.9	3.6
sp^3 Carbons of Lipid Acyl Chain	7.9	1.7
sp^2 Carbons of Unsaturation Point	6.4	2.4
Terminal Methyls	15	3.5

Results and Discussion

Figure 1 shows the ^{13}C DNP MAS ssNMR spectra of proteoliposomes with either SL-lipids or TOTAPOL as the polarization reagent. Upon inspection it is apparent that the SL-lipid system provides a higher degree of DNP enhancement when compared to the traditional TOTAPOL system. In addition, the observed DNP enhancement remains uniform throughout the lipid bilayer in the SL-lipid system. However, in the TOTAPOL system the most enhancement is observed at the periphery of the lipid bilayer and the least in the interior of the membrane. The measured enhancements of the proteoliposome samples are given in **Table 1**.

Acknowledgements

This work was performed at the National High Magnetic Field Laboratory, which is supported by National Science Foundation Cooperative Agreement No. DMR-1157490, the State of Florida, and the U.S. Department of Energy.

References

1. Metzler, R. and Klafter, J. Phys Rep. **39(1)**:1-77 (2000).
2. Ingo, C., et al., Magnetic Resonance in Medicine, **71(2)**: 617-627 (2014).

Figure 1

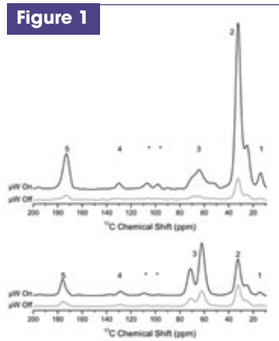

^{13}C CP MAS μW on (black) and off (grey) spectra of proteoliposomes with SL – lipids (top) or TOTAPOL (bottom) as the polarizing agent. The observed resonances are labeled as follows: 1 lipid terminal methyls, 2 sp^3 carbons of lipid acyl chain, 3 lipid glycerol backbone, 4 sp^2 carbons of unsaturation point in lipid acyl chain, 5 lipid carbonyls and $^{13}C'$-L12 enriched KL_4, * resonances from detection of material in the rotor end cap. The lipid glycerol backbone resonances were masked by the glycerol in the bulk solvent of the TOTAPOL system

Biochemistry

Furanoterpenoid accumulation in response to microbial attack in rotting sweetpotatoes has long been linked to deaths and lung edema of cattle in the world. It is not known if these toxins extend to the healthy part of the plant, which is commonly used as a food crop for many rural poor families in sub-Saharan Africa. The researchers used both MS and NMR methods to determine the presence of ipomeamarone and dehydroipomeamarone in healthy-looking parts of the plants. The authors conclude that ipomeamarone accumulation in the healthy parts of damaged sweetpotato storage roots should be considered as a potential economic problem and health threat to both the rural poor farm families and large-scale farmers worldwide.

Toxic Ipomeamarone Accumulation in Healthy Parts of Sweet Potato (Ipomoea batatas L. Lam) Storage Roots on Infection by Rhizopus Stolonifer

Wamalwa, L.N. (International Potato Center); Cheseto, X. (ICIPE, Behav. and Chem. Ecol.); Ouna, E. (ICIPE, Behav. and Chem. Ecol.); Kaplan, F. (Kaplan Schiller Research,LLC.); Maniania, N.K. (ICIPE, Behav. and Chem. Ecol.); Machuka, J. (ICIPE, Behav. and Chem. Ecol.); Torto, B. (ICIPE, Behav. and Chem. Ecol., Kenya); Ghislain, M. (International Potato Center, Kenya)

Introduction

Furanoterpenoid accumulation in response to microbial attack in rotting sweet potatoes has long been linked to deaths and lung edema of cattle (1-2). However, it is not known whether furanoterpenoid, ipomeamarone accumulates in the healthy-looking parts of infected sweet potato storage roots. This is critical for effective utilization as animal feed and assessing the potential negative impact on human health. This work was accepted by the J. Agric. Food. Chem. (3).

Experiment

We first identified the fungus from infected sweet potatoes as MI-1 *(Rhizopus stolonifer)* and then infected healthy sweet potato samples to determine furanoterpenoid content. Ipomeamarone and its precursor, dehydroipomeamarone, were isolated and purified by chromatography from fungus infected sweet potatoes in the infected and uninfected regions. The structures of the furanoterpenoids were verified using NMR.

The NMR for this work was done on the 600 MHz Bruker instrument outfitted with a 5 mm cryogenic probe in the AMRIS Facility at the University of Florida.

Results and Discussion

Dehydroipomeamarone and ipomeamarone were detected in all the samples and controls at varying concentrations. Suprisingly, ipomeamarone and dehydroipomeamarone concentration was at toxic levels in healthy-looking regions.

Conclusions

This study provides fundamental information on toxic furanoterpenoid accumulation in relation to infection site. High furanoterpenoid levels in healthy-looking tissues could cause health problems when fed to live stocks or consumed by humans.

Acknowledgements

NMR experiments of this work was performed at the National High Magnetic Field Laboratory, which is supported by National Science Foundation Cooperative Agreement No. DMR-1157490, the State of Florida, and the U.S. Department of Energy.

In addition, we would like to acknowledge the funding sources the Rockefeller Foundation, United States Agency for International Development and Bill and Melinda Gates Foundation.

References

1. Fighera, R.A. et al. (2003). Pesq. Vet. Brasil. **2003**, 23(4), 1-5.
2. Oguni, I. and Uritani, I. (1974). Plant Physiol. **1974**, 53, 649-652.
3. Wamalwa, L.N. et al. (2014). J. Agric. Food. Chem. in press.

Figure 1

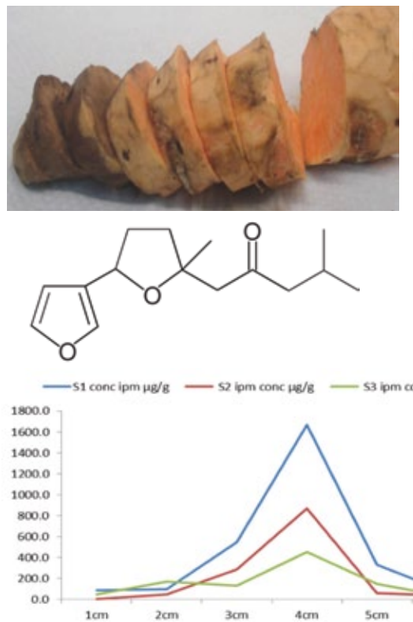

Structure of ipomeamarone and amounts in infected and uninfected tissues.

Biochemistry

Since the discovery of long-lived electronic coherence in light-harvesting proteins, there has been intense interest in understanding the mechanisms and implications of these quantum effects on energy transfer processes. There is, however, great difficulty in distinguishing vibrational coherence from electronic coherence, as they can both result in oscillatory signals of similar frequencies. A high magnetic field is expected to modify the relative energies and/or intensities of electronic (exciton) states differently than states corresponding to vibrational coherences. Progress toward differentiating and better understanding these coherent phenomena could help to resolve long-standing questions in this field.

Ultrafast Dynamics in Photosynthetic Protein Complexes

Dean, J.C. (U. of Toronto, Chemistry), Bishop, M.M. (NHMFL), McGill, S.A. (NHMFL), Scholes, G.D. (Princeton U., Chemistry)

Introduction

During the prior magnet-time period, ultrafast spectrally-resolved pump-probe (SRPP) spectroscopy was successfully implemented at the Split Florida-Helix facility at NHMFL. This technique is highly sensitive to coherent oscillations in time-resolved spectroscopic signals, and the ability to spectrally resolve pump-probe signals allows for identification of the active electronic/vibronic bands emitting the coherent signal.

Given the sensitivity of ultrafast pump-probe spectroscopy to oscillatory signals, its setup and optimization was the first subject of the prior magnet time, and immediately following, preliminary experiments were performed on the cryptophyte algae phycobiliproteins PC577 and PC645. By comparing patterns observed for coherences in pump-probe spectra at high field to zero field, we expect to discriminate between vibrational and excitonic coherences.

Experimental

Spectrally-resolved pump-probe spectroscopy was performed with a commercial optical parametric amplifier (OPA) with a spectral bandwidth of ~20 nm FWHM and 35-40 fs pulse duration. The compressed pulses were passed through a wedged beam-splitter transmitting 99% to be used as the pump beam, leaving the front-reflected beam to be used as the probe and the back-reflected as reference. The pump was aligned through a delay stage and both beams were combined in the sample cell placed in the bore of the magnet. The probe was brought into a spectrograph where it was dispersed on a CCD camera and readout. For the protein samples, a small filament stirrer was used.

Results and Discussion

Pump-probe experiments were performed through the magnet at 0 and 25 T. The first sample was the laser dye cresyl violet as a reference and those results collected at full field are summarized in Figure 1a) (single scan). Figure 1a) (middle, inset) shows the kinetic traces at 497 and 490 THz where oscillations are clearly evident. Removal of the biexponential population decay leaves only the coherent features as residuals shown at the bottom of Figure1a) along with the Fourier transform (FT) which reveals the single dominant vibrational frequency.

Following cresyl violet, experiments on PC577 were done first with the OPA set to 590 nm at 25 T and 0 T. The 25 T results are shown in Figure 1b). For comparison with cresyl violet, the data shown for PC577 is an average of three separate scans, and oscillations can be seen in the kinetic traces. The FT of the residuals displays a clear oscillation around 300 cm^{-1} and some smaller amplitude features at higher frequency. This is consistent with prior results done without the presence of the magnetic field.[1] Unfortunately, data taken with the same excitation conditions at 0 T were significantly noisier and precluded comparative information.

The same experiment was attempted on PC645, which displays weaker oscillations in the spectral region of interest and no reproducible coherence was detected as a result.

Acknowledgements

This work was performed at the National High Magnetic Field Laboratory, which is supported by National Science Foundation Cooperative Agreement No. DMR-1157490, the State of Florida, and the U.S. Department of Energy. The authors gratefully acknowledge Dima Seminov for designing/building a stirring probe.

References

1. McClure, S. D.; Turner, D. B.; Arpin, P. C.; Mirkovic, T.; Scholes, G. D. J. Phys. Chem. B **2014**, 118, 1296-1308.

Figure 1

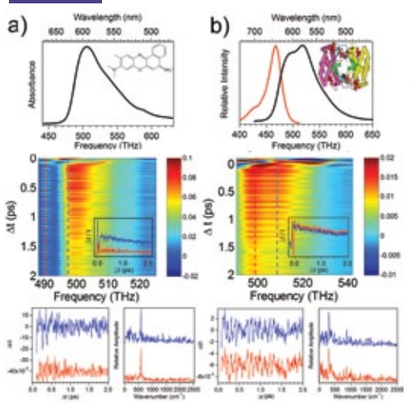

Steady-state (top) and pump-probe spectra (middle) of (a) cresyl violet and (b) PC577 at 25 T with kinetic traces (middle, inset) and residuals after subtraction of biexponential decay.

Biochemistry

This work uses NHMFL's 900MHz UWB to study prion protein fibrils related to Creutzfeldt-Jakob disease (humans), mad cow disease (bovines), and scrapie (sheep). The high sensitivity from the 900MHz field and efficient low-E probe allows them to dilute with 75% natural abundant protein to distinguish between intra- and inter-molecular contacts in the aggregated fibrils. The measured ^{13}C-^{13}C distances reveals a turn in the core region of the fibril structure.

Long Range DARR ^{13}C-^{13}C Correlation Experiments on HuPrP23-144 Fibrils

Aucoin, D.S.; Theint, T.; Jaroniec, C.P. (Ohio State U., Chemistry)

Introduction

Prion protein (PrP) is a member of a class of commonly misfolded proteins whose improper folding has been implicated in a variety of diseases ranging from dementia to heart disease. PrP can convert into β-sheet rich aggregate structures, the accumulation of which is associated with transmissible spongiform encephalopathies (TSEs), a group of fatal neurodegenerative disorders. TSEs affects both human and animals, resulting in fatal diseases such as Creutzfeldt-Jakob disease (humans), mad cow disease (bovines), and scrapie (sheep). The neurotoxic structures associated with TSE can be propagated in normally folded prion protein via contact with the misfolded protein, indicating that the ability to fold is associated with the structure of the prion protein aggregates. Understanding the detailed structures of these misfolded aggregates will play a vital role in determining how the neurotoxic folds can be transferred from protein to protein and may assist in designing novel drugs which prevent such misfolding. NMR provides a valuable tool for determining the structures of these proteins on an atomic level.

Experimental

Using the 900 MHz NMR system at the National High Magnetic Field Laboratory we acquired ^{13}C-^{13}C DARR correlation spectra of four selectively ^{13}C labeled truncated prion protein samples containing PrP residues 23-144 (HuPrP23-144). These samples were generated using 1,3 -^{13}C glycerol or 2 -13C glycerol and contain either 100% of the labeled protein, or a sample diluted with 75% natural abundance PrP in order to obtain only intra-molecular contacts.

The DARR 13C-13C correlation experiments were conducted using relatively long mixing times (500 ms and 100 ms) on the 900 MHz instrument equipped with the low electric field probe optimized for 13C detection. The experiments on the 2-13C glycerol labeled PrP sample and on both dilute samples were conducted with the probe set to double resonance, while our 900 MHz experiments on the 1,3 -13C glycerol sample were conducted with the probe in triple resonance mode. This setting resulted in approximately half the signal to noise for this sample.

Results and Discussion

Our DARR experiments provided numerous short and long range crosspeaks between different regions of the structured fibril core. A series of correlations between residues 117-119 and 134-137 indicates the possibility that the peptide contains a turn that puts these regions in proximity. These contacts were observed both in samples that were fully labeled and samples where the labels were diluted to 33% indicating that they arise from contacts within a single subunit of the fibril.

Conclusions

Our data provides new constraints for the structure of the core region of the human prion protein, and indicates the presence of a turn in the structured region.

Acknowledgements

A portion of this work was performed at the National High Magnetic Field Laboratory, which is supported by National Science Foundation Cooperative Agreement No. DMR-1157490, the State of Florida, and the U.S. Department of Energy.

In addition, funding was provided by National Institutes of Health NIGMS Award R01GM094357 and by National Science Foundation MCB Award 1243461

Figure 1

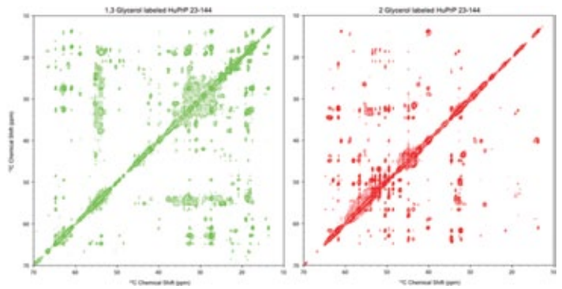

DARR ^{13}C-^{13}C correlation experiments of HuPrP23-144 fibrils generated using 1,3 -^{13}C glycerol (green, left) or 2 -^{13}C glycerol (red, right). These labels allowed for observation of numerous short and long range crosspeaks.

Biochemistry

NMR based metabolomics measurements are traditionally performed using 1D and 2D ^{1}H NMR methods with commercially available NMR probes. In this report, Edison et al extends these measurements to natural abundance ^{13}C measurements. In order to achieve this a custom made HTS probe constructed within the MagLab was utilized to overcome sensitivity limits associated with the low signal-to-noise associated ^{13}C measurements. Using synthetic mixtures of 20 common metabolites and biological samples (mice serum and fruit fly extracts), researchers were able to identify metabolites within a 40-200 nM concentration range and easily annotated metabolites within the ^{13}C spectra.

A Natural Abundance ^{13}C NMR Approach for Metabolomic Studies of Complex Mixtures

Clendinen, C.S. (UF, Biochemistry and Molecular biology); Lee-Mcmullen, B.A. (UF, Biochemistry and Molecular biology); Stupp, G.S. (UF, Biochemistry and Molecular biology); Williams, C. (UF, Department of Entomology and Nematology); Ramaswamy, V. (FSU, Maglab); Edison, A.S. (UF, Biochemistry and Molecular Biology)

Introduction

Usually with NMR-based metabolomics, 1D and 2D ^{1}H-detected methods are used to analyze the global response of a biological system to perturbation/stress. Though ^{1}H-detected methods are extremely useful, the advantages of ^{13}C NMR techniques over traditional ^{1}H NMR include the carbon spectral width and molecular backbone information. Here, we determine the potential of ^{13}C-detected NMR metabolomics at natural abundance. In order to develop and validate the approach, we first show results from synthetic mixtures of 20 common metabolites. We then applied the overall approach to mice serum and D. *melanogaster* extracts.

Experimental

1D ^{1}H and ^{13}C spectra were collected on an Agilent VNMRS-600 spectrometer using our custom 1.5-mm ^{13}C HTS probe (Ramaswamy, 2013). Synthetic mixture and fly extract ^{1}H data were collected with a simple pulse sequence with preset of residual water with a spectral width of 12 ppm (7183.9 Hz) at an observe frequency of 599.68 MHz. Synthetic mixture and fly ^{13}C spectra were collected on a total time of 2 hr 3 min, with a 212 ppm (32051.3 MHz) with an observe frequency of 150.79 MHz; 0.10 sec relax delay; 0.800 acquisition time. Both used a 60-degree pulse. All ^{1}H was decoupled at 599.68 MHZ with a power of 37 dB continuously on WALTZ-16

Results and Discussion

See Figure 1.

Conclusions

The HTS ^{13}C sensitive probe allows for minimized time and sample allowing for carbon metabolomics. The synthetic mixtures provided proof of concept that we would be able to identify metabolites within 40-200 nM. Unlike the ^{1}H spectra, the ^{13}C spectra were easily annotated. All results are published in Clendinen, 2014.

Acknowledgements

A portion of this work was performed at the National High Magnetic Field Laboratory, which is supported by National Science Foundation Cooperative Agreement No. DMR-1157490, the State of Florida, and the U.S. Department of Energy. In addition, this work is supported NIH/NIBIB grant R01EB009772-01

References

1. Clendinen, C., et al., AC, **86**, 9242-9250 (2014)
2. Ramaswamy,V., et al., eMagRes, **2**, 215-228 (2013).

Figure 1

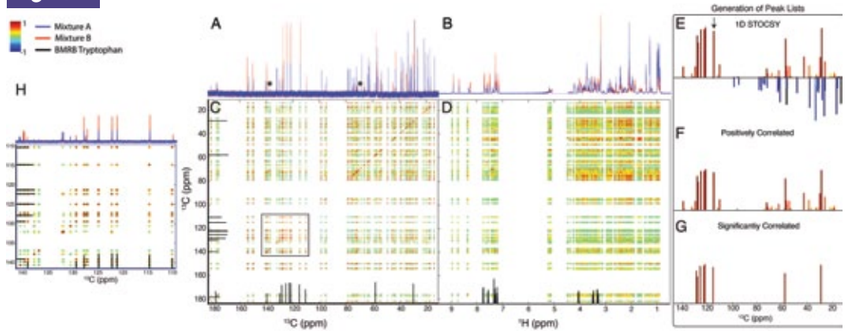

1D ^{1}H and ^{13}C NMR spectra were collected for each sample. Spectra for the synthetic compounds are shown in the above figure A and B, respectively. C and D displays the 2D ^{13}C-^{13}C STOCSY and ^{13}C-^{1}H SHY maps respectively. A closer look at the 110-150 ppm region in ^{13}C-^{1}H SHY is displayed in H. Generation of peak lists (E-G) were much more successful when using ^{13}C spectra that ^{1}H. This workflow was used for the mouse serum and fly extracts. Reprinted with permission from Clendinen, C., et al., AC, **86**, 9242-9250 (2014). Copyright 2014 American Chemical Society

Biochemistry

The research groups of Paravastu/FSU and Singh/FAMU report the use of ^{31}P NMR to monitor the penetration of cell penetrating peptides (CPPs) into skin. They have found that the ^{31}P NMR chemical shift of skin lipids changes with skin permeation depth and time, and as well as peptide type and concentration of CPPs. Their discovery can provide insight into how CPPs interact with the skin lipids deep layers and drug delivery through skins.

Solid-State NMR Based Monitoring of Permeation of Cell Penetrating Peptides into Skin

Desai, P.R.; Shah, P.P.; Patlolla, R.R.; Singh, M. (Florida A&M U., Pharmaceutical Sciences); Cormier, A.R.; Paravastu, A.K. (Florida State U., Chemical and Biomedical Engineering)

Introduction

Skin acts like a protective barrier against foreign agents penetrating into the body, making drug delivery into deep layers challenging. Cell penetrating peptides (CPPs) are known to effectively permeate into the skin, but tracking CPP penetration in deep skin layers is challenging. We have shown that CPP penetration can be detected using ^{31}P solid state NMR without the need for fluorescent tags required for fluorescence based methods.

Experimental

Hairless rat skin was used for the study. Four peptides were permeated into the skin at various concentrations and permeation time periods using Franz diffusion cells. The skin was then sectioned using a cryotome at different depths. For each skin sample, ^{31}P solid state NMR spectra were collected under magic angle spinning using the Ernst angle technique. Confocal laser scanning microscopy was used as a complementary tool to track these CPP's across the skin.

Results and Discussion

We observed ^{31}P NMR chemical shifts that depended systematically on peptide type, peptide concentration, skin depth, and permeation time **(Fig 1)**. Significant changes were observed for TAT, R11, R8, and YKA peptides. Furthermore, TAT, which is known to be a highly effective CPP, produced the largest shifts in the ^{31}P NMR signal. YKA, which is not a CPP, produced the smallest shift in the NMR spectra. Observed effects decreased with skin depth up to 200 µm, as confirmed by a decrease in observed fluorescence in confocal laser scanning microscopy images. Our results indicate that CPP permeation affects the local chemical environment experienced by skin lipids, suggesting that solid state NMR could be used to study mechanisms of CPP permeation.

Conclusions

Solid state NMR was shown to be capable of tracking the permeation of peptides into the deep layers of skin. Unlike established fluorescence based methods, the NMR data indicate effects on local organization of the lipids. The recorded NMR spectral shifts represent a novel basis for CPP tracking and the potential to attain insight into how CPPs interact with the skin lipids while permeating from the stratum corneum to the deep layers.

Acknowledgements

The authors acknowledge Dr. Geoffrey Strouse and Steve Hira, Department of Chemistry, Florida State University for their kind help in confocal microscopic studies and also the financial assistance provided by RCMI (NIH) Grant Number G12RR003020. A portion of this work was performed at the NHMFL, which is supported by National Science Foundation (DMR-0654118), the State of Florida, and the U.S. Department of Energy.

References

1. Desai, P.R., *et al.*, European Journal of Pharmaceutics and Biopharmaceutics, **86**,190–199 (2014).
2. Ernst, R.R., *et al.*, Review of Scientific Instruments, **37**, 93 (1966).
3. Afonin, S., *et al.*, Chemphyschem, 2134-2142 (2006).
4. Verly, R.M., *et al.*, Biophy, 2194-2203 (2009).

Figure 1

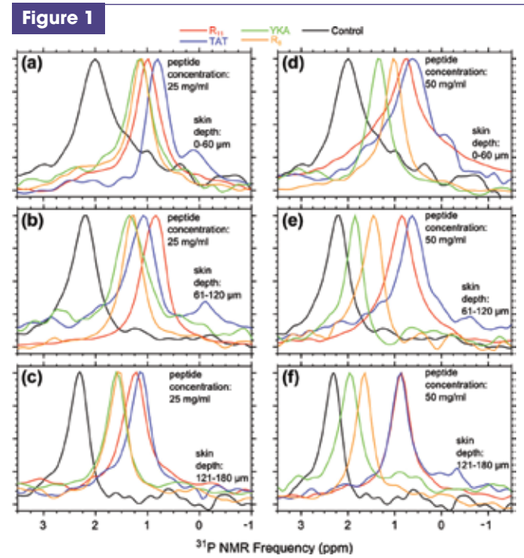

^{31}P NMR spectra from skin sections at different depths (a and d: 0-60 µm; b and e: 61-120 µm; c and f: 121-180 µm), for 16 hr permeation of solutions with different peptide concentrations (a, b, and c: 25 mg/ml; d, e, and f: 50 mg/ml).

Biochemistry

Understanding the structure and function of the cell division apparatus of *Mycobacterium tuberculosis* is crucial for advancing drug development against tuberculosis. In this work the collaborative team reports the solid-state NMR structure of a transmembrane protein, CrgA. CrgA is a central component of the *M. tuberculosis* cell division machinery. Since these types of proteins are very sensitive to the environment in which they exist, CrgA structure was determined in an environment that models well the biophysical properties of the native membrane. To determine this structure, solid state NMR data from liquid-crystalline lipid bilayer preparations were used to characterize an atomic resolution structure of the transmembrane domain of CrgA with refinement by restrained molecular dynamics simulations in the same lipid environment. This is the first multi-helix full-length membrane protein to be characterized in liquid crystalline lipid bilayers.

Structure and Disorder in the CrgA Cell Division Protein from *M. tuberculosis*

Das, N.; Dai, J. (Florida State U., Institute of Molecular Biophysics); Hung, I. (NHMFL); Rajagopalan, M. (U. of Texas, Health Science Center); Zhou, H.-X. (Florida State U., Physics); Cross, T.A. (Florida State U., Chemistry and Biochemistry/NHMFL)

Introduction

Understanding the structure and function of the cell division apparatus of *Mycobacterium tuberculosis* is crucial for advancing drug development against tuberculosis. Here, we report the solid-state NMR structure of a transmembrane protein, CrgA, that is a central component of the *tuberculosis* divisome. Small helical membrane protein structures are particularly sensitive to their environment and consequently we characterized CrgA in an environment that models well the biophysical properties of the native membrane. To determine the structure, both oriented sample and magic angle spinning NMR data from liquid-crystalline lipid bilayer preparations were used along with refinement by restrained molecular dynamics simulations in the same lipid environment. The structure suggests how CrgA serves as a platform for other proteins of the divisome. Intrinsically disordered regions (IDRs) have recently been recognized to serve important roles in protein –protein interactions, yet little is known about membrane protein IDRs. Here, we demonstrate that CrgA has an IDR.

Results & Discussion

Both Oriented Sample (OS) and Magic Angle Spinning (MAS) solid state NMR have been used to characterize the structure and disorder of CrgA, a 93-residue protein that is known to recruit 5 other proteins to the cell division apparatus. Here, the structure of CrgA was determined in a liquid-crystalline lipid bilayer environment. The ssNMR data define a complete structure for the transmembrane domain that was refined using restrained molecular dynamics simulations in an all-atom representation of the same lipid bilayer environment as in the NMR samples [1]. Uniquely, in this study the residual anisotropic restraints were used to evaluate the nascent structure in the 18 residues of the N-terminus.

Conclusions

This is the first multi-helix full length membrane protein to be characterized in liquid crystalline lipid bilayers. The structure provides insights into how other proteins bind. At least two binding sites in the transmembrane region of the protein were identified by the presence of conserved small residues (glycine & alanine). These sites maybe for binding two other transmembrane proteins, FtsQ and CwsA. Furthermore the characterization of the intrinsically disordered domain at the cytoplasmic N-terminus suggests that either FtsZ or FtsI bind to this site. The fifth protein to bind to CrgA is PbpA that is likely to bind to the interhelical loop.

Acknowledgements

This work was supported by NIH through AI-074805, AI-073891 & AI023007 performed at the National High Magnetic Field Laboratory, which is supported by National Science Foundation grant number DMR-1157490 and the State of Florida.

References

1. Das, N., *et al.*, PNAS, 112:E119-E126 (2015).

Figure 1

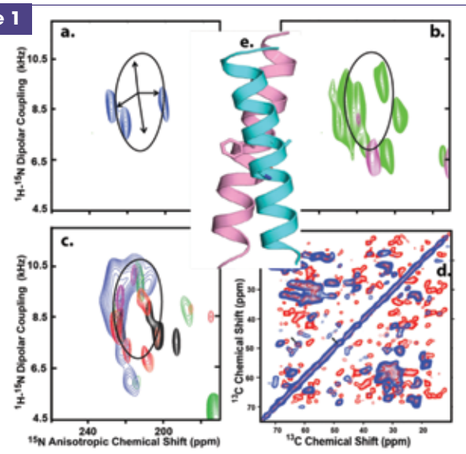

All spectra obtained in a NHMFL WB600 spectrometer with a NHMFL Low-E probe. **A,B,C)** OS ssNMR spectroscopy of full length CrgA. Different amino acid specific labeled samples are distinguished by color from which orientational restraints are obtained. **D)** MAS ssNMR of full length CrgA from which interhelical restraints were obtained. **E)** The combination of orientational and distance restraints led to the structure of the transmembrane domain of CrgA.

Biology

Apratoxins are cytotoxic natural products originally isolated from marine cyanobacteria. They decrease cell reproduction through a number of different mechanisms, including the downregulation of various receptors and inhibiting trafficking of secretory molecules that act on these receptors. This one –two punch system has proven to be a very powerful tool to fight cancers that rely on autocrine loops such as colorectal cancer. In this report, researchers through the rational design and total synthesis of apratoxin A/E hydrids, apratoxin S4 (1a) and apratoxins S7-S9 (1b-d), improved upon the antitumor activity and tolerability of this custom tailored apratoxin in vivo. In this study, NMR instrumentation within the AMRIS facility was used to characterize the newly designed apratoxins.

Total Synthesis and Biological Evaluation of Potent Apratoxin S4 Based Anticancer Agents

Chen, Q.-Y. (UF, Medicinal Chemistry); Liu, Y. (UF, Medicinal Chemistry); Cai, W. (UF, Medicinal Chemistry); Luesch, H. (UF, Medicinal Chemistry)

Introduction

Apratoxins are cytotoxic natural products originally isolated from marine cyanobacteria that act by preventing cotranslational translocation early in the secretory pathway to downregulate receptor levels and inhibit growth factor secretion, leading to potent antiproliferative activity. Through total synthesis of the apratoxin A/E hybrid apratoxin S4 (**1a**) we have previously improved the antitumor activity and tolerability in vivo and demonstrated the therapeutic potential of this mechanism of action.

Experimental

NMR spectra were recorded on a Varian Mercury 400 MHz, Bruker Avance III 600 MHz or Agilent VNMR 600 MHz spectrometers. 600 MHz spectrometers were equipped with a 5 mm TXI cryogenic probe.

Results and Discussion

Apratoxin S4 (**1a**) and newly designed analogues apratoxins S7-S9 (**1b-d**) with various degrees of methylation at C34 (**1b,c**) or epimeric configuration at C30 (**1d**) were efficiently synthesized utilizing improved procedures (Figure 1). Apratoxins S7 (**1b**) and S8 (**1c**) lack the C34 stereocenter and this reduction of structural complexity did not affect the mutidimensional assay profile, viz. antiproliferative activity against HCT116 colorectal cancer cell growth in vitro, downregulation of receptor tyrosine kinase MET and inhibition of VEGF-A secretion as an indicator of target engagement (Figure 2). Apratoxin S9 (**1d**) – the C30 epimer of apratoxin S4 (**1a**) – exhibited increased activity in all three assays with sub-nanomolar activity and represents the most potent compound of this class to date. Compounds **1a-d** showed excellent aqueous, plasma and cellular stability, but were rapidly metabolized by microsomes to uncharacterized biotransformation products that potentially retain activity. Dehydration is hypothesized to be a deactivation pathway of the apratoxins. Unlike other apratoxins, apratoxin S8 (**1c**) lacks the propensity to dehydrate. Compound 1c showed efficacy in a dose-dependent manner using a HCT116 xenograft mouse model (Figure 3).

Conclusions

SAR studies demonstrated that **1b** and **1c** retain activity compared with 1a and identified apratoxin S9 (**1d**) as the most potent apratoxin to date, exhibiting 2-3 fold improved in vitro activity. Overall our study further corroborates that the development of this class of anticancer agents is warranted.

Acknowledgements

Bankhead-Coley Cancer Research Program, grants 1BG07 and 4BB07; NIH, grant R01CA172310; and J.R. Rocca.

References

1. Chen, Q.-Y., *et al.*, Journal of Medicinal Chemistry, **57**, 3011-3029 (2014).

Figures

1

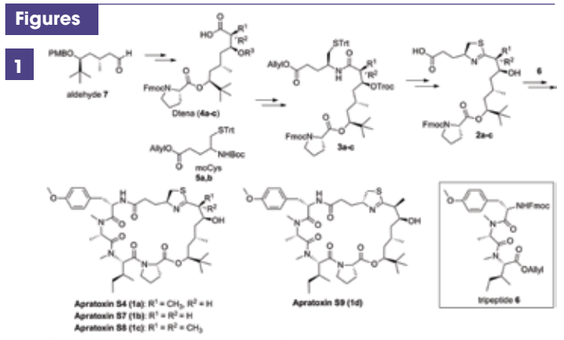

General synthetic route for apratoxin S4 and analogues.

2

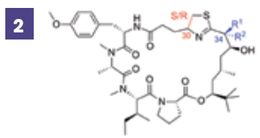

Apratoxin	IC_{50} (nM) cell viability	IC_{50} (nM) VEGF-A secretion
S4 (30*S*,34-Me)	1.43	0.32
S7 (30*S*,34-H_2)	1.25	0.30
S8 (30*S*,34-Me_2)	1.99	0.47
S9 (30*R*,34-Me)	0.69	0.12

Activities of synthetic apratoxins on HCT116 cell viability and VEGF-A secretion.

3

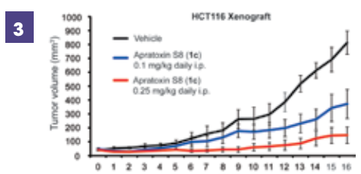

In vivo efficacy of apratoxin S8 **(1c).**

Biology

Membrane proteins comprise approximately a third of cellular proteins and perform many vital functions. The structures of membrane proteins are highly dependent on their local environment, which calls into question the validity of studying them in artificially made model systems designed to mimic the cell's membrane and simplify experiments. In this report, external users used the 900 MHz solid-state NMR spectrometer, equipped with a low-E $^{1}H/^{13}C/^{15}N$ MAS probe, to characterize the conformation of a microbial photosensor (*Anabaena* Sensory Rhodopsin) in the complex environment of the *E. coli* membrane. Overall, this analysis revealed that the structure of the photosensor is largely conserved between the cell membrane and the simplified synthetic liposomes more commonly used for studies of membrane proteins. The authors conclude that small, site-specific perturbations allow this protein to subtly adapt to its environment without large structural rearrangement.

Published in: Biophys J. 2015 Apr 7;108(7):1683-96. doi: 10.1016/j.bpj.2015.02.018

In Situ Structural Studies of *Anabaena* Sensory Rhodopsin in the *E.coli* Membrane

Ward, M. E.; Wang, S.; Munro, R.; Ritz, E.; (U. of Guelph, Physics and Biophysics); Hung, I.; Gor'kov, P.L. (NHMFL); Jiang, Y.; Liang, H. (Colorado School of Mines, Metallurgical and Materials Engineering); Brown, L. S.; Ladizhansky, V. (U. of Guelph, Physics and Biophysics)

Introduction

Membrane proteins comprise approximately a third of cellular proteins and perform many vital functions. Interactions with the membrane environment, e.g., lipids, other proteins, etc., are important factors which often influence both the conformation and function of membrane proteins [1,2]. While the lipid bilayer represents a good, experimentally tractable model for structural and functional studies of membrane proteins, the natural cellular membrane includes a diverse array of lipids and other transmembrane (TM) proteins, and is invariably more complex. Here, we applied 2D and 3D solid-state NMR to characterize the conformation of a 7TM microbial photosensor, *Anabaena* Sensory Rhodopsin (ASR), in the inner membrane environment of *E. coli.*

Experimental

The 900 MHz solid-state NMR spectrometer equipped with a low-E $^{1}H/^{13}C/^{15}N$ MAS probe at the NHMFL was used to perform 3D NCACB and CANCO experiments on a uniformly $^{15}N,^{13}C$-labeled sample of ASR in the native *E.coli* membrane environment (EM-ASR). Spectra have been processed with NMRpipe and analyzed using CARA software.

Results and Discussion

We have found that ASR is organized into trimers in the *E.coli* membrane, similar to those found in the proteoliposome environment (PL-ASR) [3,4]. Site-specific analysis of chemical shifts for approximately 40% of residues reveals that the overall structure of ASR is largely conserved in the *E. coli* membrane, with many of the important structural features of rhodopsins remaining intact. Specifically, the retinal binding pocket and the trimeric interface look very similar in both environments (Fig. 1). Subtle changes, corresponding to chemical shift perturbations of up to 0.5 ppm and 1 ppm in ^{13}C and ^{15}N dimensions, respectively, are mostly detected on the faces of helices which are oriented towards the interior of a monomer or the bilayer (Fig 1).

Conclusions

SSNMR can be used to detect small, site-specific perturbations in large proteins which occur as a result of changes in the membrane environment. Our results indicate that ASR subtly adapts to its environment without large structural rearrangement.

Acknowledgements

This work was supported by the Natural Science and Engineering Research Council of Canada (NSERC). A portion of this work was performed at the National High Magnetic Field Laboratory, which is supported by National Science Foundation Cooperative Agreement No. DMR-1157490, the State of Florida, and the U.S. Department of Energy. M.W. is a recipient of an NSERC Postgraduate Fellowship.

References

1. Andersen, O.S., *et al.*, Annu. Rev. Biophys. Biomol. Struct., 36, 107–30 (2007).
2. Lee, A.G., Biochim. Biophys. Acta - Biomembr., 1666, 62–87 (2004).
3. Wang, S., *et al.*, J. Am. Chem. Soc., 17, 16995-16998 (2012).
4. Wang, S., *et al.*, Nature Methods, 10, 1007-1012 (2013).

Figure 1

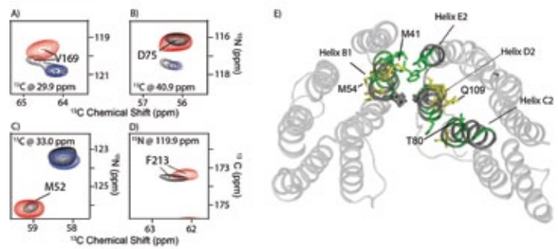

2D planes of **A-C)** NCACB and **D)** CANCO experiments performed on PL-ASR (red), EM-ASR (black), and on a control *E.coli* membrane sample without ASR (EM-NIC, blue). PL-ASR and EM-NIC spectra were recorded on a 800 MHz spectrometer at Guelph, while EM-ASR spectra were recorded on the 900 MHz spectrometer at NHMFL. **E)** Extracellular view of the intermonomer interface. Green and yellow represent unperturbed and perturbed residues, respectively.

Biology

This work uses a special NMR sequence to obtain in vivo spectra from localized regions of the brain. This sequence has been shown to specifically benefit from the high signal-to-noise, spectral resolution, and nuclear relaxation properties that are achieved at 900MHz. In this report the investigators measure metabolites brain metabolites (ATP, NAA, PCR, Gln, GSH) from a part of the NMR spectrum (the downfield resonances at chemical shifts > 4.7 ppm) rarely studied in vivo. This is the first time that in vivo quantitative NMR of this downfield spectral region has been determined at 21.1 T. The authors also demonstrate quantitative changes in the down field metabolite concentrations (ie ATP, NAA, PCr) agreeing with what has been previously determined using the standard up field resonances of these metabolites.

In vivo Quantitative MR Spectroscopy Using Relaxation Enhancement: Unassigned Downfield Brain Metabolite Resonances at 21.1 T under Ischemic Conditions

Roussel, T. (Weizmann Institute, Chemical Physics); Rosenberg, J.T. (NHMFL); Grant, S.C. (Florida State U., Engineering/NHMFL); Frydman, L. (Weizmann Institute, Chemical Physics, NHMFL)

Introduction

The effective T_1 of macromolecular resonances may be shortened significantly using spectrally selective excitations [1]. By exciting only specific resonances, a large reservoir of magnetization remains unperturbed and can enhance MRS sensitivity by magnetization and chemical exchange [2]. Relaxation Enhanced (RE) ^{1}H MRS exploits these benefits for in vivo studies, revealing apparent T_1 reductions even for methyl resonances [3,4]. This work presents spatially localized RE spin-echo sequences to investigate *in vivo* quantitative MRS of metabolic resonating downfield from the water peak at 21.1 T, a spectral region studied previously but still lacking full assignment [5]. We quantified ATP, Gln, GSH, NAA and PCr, and estimated concentration changes with ischemia.

Experimental

All experiments were performed at the National High Magnetic Field Laboratory using the 21.1-T, 900-MHz ultra-widebore magnet equipped. Sprague-Dawley rats were scanned 12-h post ischemia. 1H MRS were acquired from a 4.8x4.8x5.2-mm voxel placed in the contra- and ipsilateral (ischemic) sides of the brain using a RE spin-echo sequence, which targeted the 6-10 ppm spectral region by means of 90° sinc pulse and SLR-designed11 180° pulses, respectively 5 and 4 ms (TR=1.5s, NA=1024). Spatial localization was achieved using 3D LASER (Fig.1). Metabolites were quantified using an algorithm based on GAMMA [6]. The metabolite basis set contained only ATP, Gln, GSH, NAA and PCr, present at ≥ 1mM concentrations, plus four broad Gaussian resonances to model the baseline.

Results and Discussion

Downfield spectra acquired on the ipsi- and contralateral hemispheres of stroked brains show rich *in vivo* metabolic information (Fig.2). The estimated spectra fit the acquired data, showing intense macromolecular contributions, especially around 8 ppm. Resonances show substantial linewidths, presumably due to water chemical exchange, leading to spectral overlapping even at 900 MHz. All metabolites exhibit lower concentrations in the ipsi- than in the contralateral side (Fig.3) with NAA affected by a 5-fold difference (also observed upfield).

Conclusions

For the first time, *in vivo* quantitative MRS of the downfield spectral region was performed successfully at 21.1 T. RE significantly enhanced the global spectral quality while providing a commensurate increase in SNR per unit time, allowing for the characterization of hitherto poorly assigned resonances. This technique provides an alternative to conventional *in vivo* ^{1}H MRS by exploring downfield biomarkers.

Acknowledgements

Funding provided by the NSF (DMR-1157490) and NHMFL (UCGP and VSP), the Israel Science Foundation grant 795/13, by ERC Advanced Grant #246754, and the generosity of the Perlman Family Foundation.

References

1. Pervushin, K., *et al.*, J Am Chem Soc., 124, 12898 (2002).
2. Schanda, P., Prog Nucl Magn Reson Spectrosc., 55, 238 (2009).
3. Shemesh, N., *et al.*, Chem Eur J., 19, 13002 (2013).
4. Shemesh, N., *et al.*, Nat. Comm., 5, 4958 (2014).
5. Henning, A., *et al.*, Proc Intl Soc Mag Reson Med., 16, 777 (2008).
6. Smith, S.A., et al., J Magn Reson., A106, 75 (1994).

CONTINUED ON NEXT PAGE

Figures

1

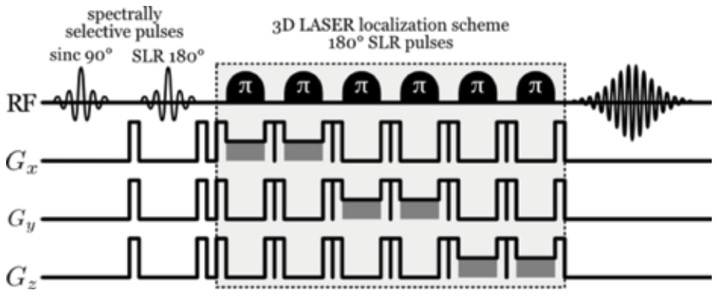

Spatially localized RE spin-echo using 3D LASER and spectrally selective pulses.

2

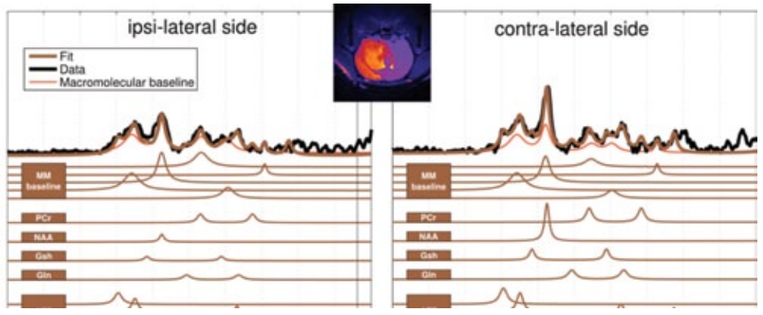

Acquired and estimated spectra from the ipsilateral and the contralateral side of the rat brain (water image on top).

3

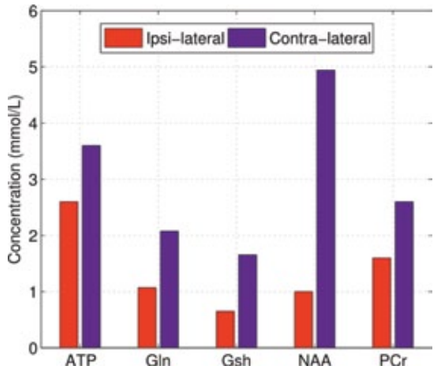

Estimated concentrations for each metabolite.

Biology

One strategy to generate a vaccine to be used to fight AIDS is to target a surface protein on HIV (gp41) with a neutralizing antibody to prevent HIV fusion with host T cells. In this report researchers use EPR instrumentation at the NHMFL to define the manner in which these antibodies recognize the ectodomain region of gp41. Based on the authors' findings they propose that anti-HIV antibodies disrupt virus entry into human T cells by perturbing the required facile hinge function in the proximal ectodomain region during membrane fusion.

Antibody-Mediated Mechanics on HIV-1 Envelope Protein gp41 at the Membrane Interface Defined by EPR Spectroscopy

Kaur, P.; Song, L. (NHMFL); Kwong, P.D. (National Institute of Health); Reinherz, E.L. (Dana-Farber Cancer Institute)

Introduction

A vaccine capable of stimulating protective anti-viral antibodies is needed to curtail the global AIDS epidemic. HIV enters human T cells through the fusion of viral and host-cell membranes. This fusion process is mediated by a surface protein, gp41, and the platform provided by the cholesterol-rich viral membrane. The membrane proximal ectodomain region (MPER) of gp41 plays a critical role in this fusion process and is a major target of vaccine design and anti-gp41 antibodies, including a newly identified potent antibody - 10E8 [1] . How these antibodies bind to the MPER segment and mediate anti-viral activity are unclear. Here, electron paramagnetic resonance (EPR) techniques were used to define the manner in which these antibodies recognize the L-shaped helix-hinge-helix MPER segment.

Experimental

The MPER peptides with a single cysteine substitution at various positions were synthesized at the Tufts Core Facility, and subsequently labeled with MTSL spin labels (R1). EPR experiments were performed on a Bruker E680 spectrometer at the NHMFL. MPER residues 1 to 22 are corresponding to 662 to 683 in the HxB2 gp41 sequence.

Results and Discussion

10E8-induced MPER conformational changes at the membrane interface were determined by EPR solvent accessibility and immersion depth measurements. Membrane immersion depths of MPER R1 residues were determined by the ratio of the collision accessibility values of relaxant reagents, oxygen and NiEDDA, measured via power saturation techniques. Upon 10E8 binding, residues 5R1 and 13R1 were lifted out of the membrane surface and exposed to the aqueous phase **(Fig. 1A)**. 10E8 also moves residues 8R1, 9R1, 17R1 and 20R1 towards the membrane surface. Taken together, 10E8 lifts up MPER N-helix and hinge region as indicated by the model built based on x-ray crystallography structure and EPR immersion depth data **(Fig. 1B).**

Conclusions

10E8 induces large conformational changes in the MPER relative to the membrane, lifting up the hinge region and extracting buried residues from the lipids. Thus, anti-HIV antibodies disrupt virus entry into human T cells by perturbing a facile MPER hinge function during membrane fusion. These findings have revealed important features for targeted vaccine design, the implications of which extend to antibody targets on other infectious diseases.

Acknowledgements

This work was supported by NIH grants RO1AI84785 / U19AI91693 (to E.L.R.), a grant from the Gates Foundation (to E.L.R.), and an UCGP grant 5080 (to L.S.).

References

1. Huang, J., *et al.*, Nature, **491**, 406-412 (2012).

Figure 1

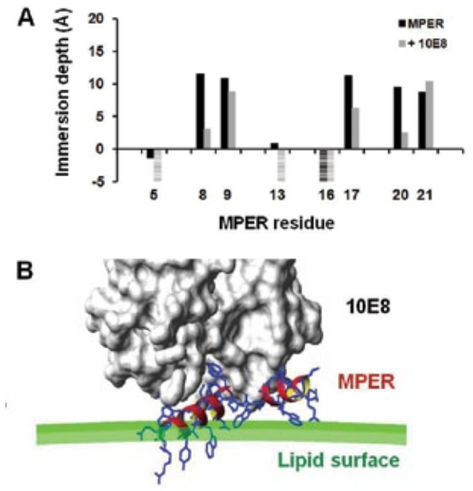

(A) Immersion depth changes of MPER R1 residues upon 10E8 binding. Depth values between -5 Å to 0 Å and larger than 0 Å correspond to lipid headgroup region and acyl chain region, respectively. Lipid surface exposed residues are indicated by stripped bars. **(B)** Model of MPER segment in complex with 10E8 antibody as viewed from the side.

Biology

Schepkin has been a key researcher in the demonstration that ultrahigh MRI can be used to detect alterations in tumor biology based on 23Na accumulation. The direct imaging of sodium content can be used to draw non-invasively a valuable conclusion on changes in tumor resistance to chemotherapy before therapy. Schepkin and Levenson hypothesize that sodium/diffusion imaging can be used as a marker of multidrug resistance in tumors and cancer drug development.

Tumor Resistance to Therapy & Sodium-Diffusion MRI

Schepkin, V.D. (NHMFL); Levenson, C.W. (Florida State U., College of Medicine)

Introduction

Ultra-high magnetic fields augment our capability to perform *in vivo* sodium MRI which is becoming a valuable tool in research and biomedical applications. Chemo-resistance, the ability of cancer cells to repel the treatment, is a common problem that significantly limits our capability to treat cancer and reduce life expectancy in patients with a wide variety of cancers. Tumor progression especially due to unsuccessful therapy can dramatically increase tumor resistance to therapy.

Results and Discussion

Using *in vivo* sodium/diffusion MRI at the 21.1T magnet, it was found that initial sodium concentration in rat glioma has a large variation, even for the same type of tumor. The analysis of this situation revealed a close relationship of sodium in glioma with glioma chemo-resistance (1). Sodium concentration in tumors has a unique capability to be an *in vivo* energy biomarker. To maintain low intracellular sodium concentration, cells consume up to 60% of the total energy produced by the cell. Thus, the capability of cells to maintain intracellular sodium gradient could be a natural indicator of the major energy balance in tumor cells. It is known that excessive glycolysis (Warburg effect) is an essential indicator of cancer metabolism. However, glycolysis is responsible only for a part of the total cellular energy metabolism. In comparison, sodium homeostasis is a more general metabolic energy indicator by including other sources of energy metabolism, such as lipid metabolism and being a driving force of the multiple transmembrane cellular fluxes.

Conclusions

Reflecting metabolic energy status and, partly, tumor cell density, sodium MRI has the potential to reveal tumor chemotherapy resistance both non-invasively and, most importantly, prior to treatment. Application of sodium MRI may lead to individualized cancer treatment strategies, avoiding unsuccessful interventions. Sodium MRI of tumors can also serve as a marker for multidrug resistance and as a valued tool for cancer drug development. It was found that sodium shares this capability with diffusion MRI. However, sodium MRI has the advantage of being several times more sensitive. During therapy, sodium detects the effects of therapy well ahead of diffusion, and, notably, responses to therapy can be seen even when there are no changes in tumor diffusion.

Acknowledgements

A portion of this work was performed at the National High Magnetic Field Laboratory, which is supported by National Science Foundation Cooperative Agreement No. DMR-1157490, the State of Florida, and the U.S. Department of Energy.

References

1. Schepkin, V.D., *et al.*, US Patent 8,880,146 (Nov 4, 2014).

Figure 1

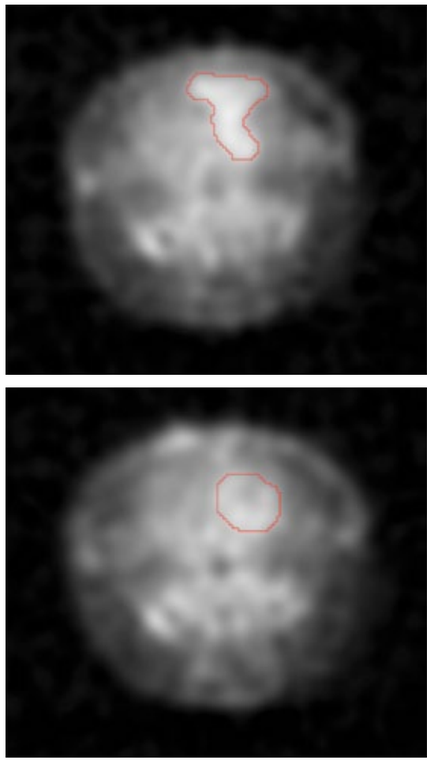

Sodium MRI of glioma in rat brain: naïve or sensitive to therapy glioma (top) has much more sodium concentration than and resistant glioma (bottom).

Magnets & Magnet Materials

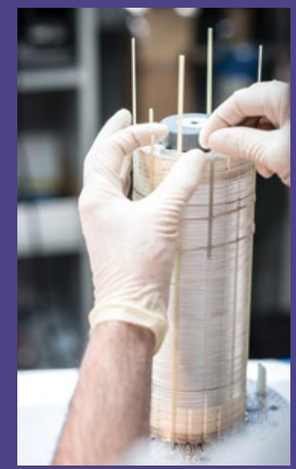

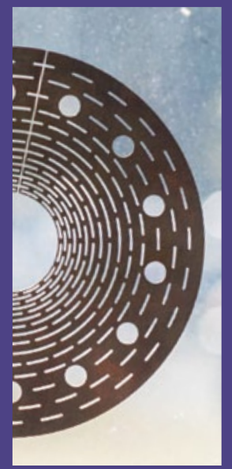

Photos by: Dave Barfield

Engineering Materials

This work illustrates that the range of opportunities for high magnetic field processing extends to high-strength high-conductivity materials.

High-magnetic-field annealing on Microstructure and Mechanical Properties of Cu-Fe and Cu-Ag composites

Zhao, C.C. (Northeastern University [NEU], PR China and NHMFL); Zuo, X.W. (NEU, PR China); Wang, E.G. (NEU, PR China); Han, K. (NHMFL/FSU)

Introduction

Cu-based in-situ composites have attracted considerable attentions due to their achievable high strength and conductivity [1]. Numerous investigations have indicated that annealing or aging played an important role in the microstructure redistribution and enhancement of properties [2]. Magnetic field annealing might affect the nucleation and growth of precipitate because magnetic field can affect convection and phase transformation in these systems.

Experimental

Cu-Ag was casted with and without high magnetic field (HMF) and then cold drawn. Cold-rolled Cu-Fe composites were heat treated at 285°C, 400°C, and 500°C for 2 hours with and without 25T HMF at NHMFL cell 7 DC resistive magnet. Post-magnetic field annealed samples were further cold-rolled to 99.2% reduction in area. Microstructure and hardness were examined using the facilities at NHMFL.

Results and Discussion

The hardness of rolled Cu-Fe samples is shown in Fig. 1 as a function of annealing temperatures. With increasing annealing temperatures, the hardness decreased in most of the rolled Cu-Fe composite. This might be related to the coarsening of α-Fe fibers. At deformation reduction of 95.6%, the hardness of samples treated under 25 T was lower than that under 0 T. At further reduction of 99.2%, the hardness of samples under 25 T was much higher than that under 0 T. These changes in trend might be a result of the impacts of HMF annealing on strain-hardening. In Cu28wt%Ag composites, we found that an external 12 T HMF decreased the spacing of nano-sized Ag precipitates by 24% because of the increased growth velocity of Ag precipitates during the subsequent solid reaction after casting [3].

Conclusions

Hardness of as-rolled Cu-Fe composite is related to the annealing temperatures and magnetic fields. The 25-T magnetic field annealing appears to influence strain-hardening rate in Cu-Fe composite. In Cu28 wt%Ag composites, magnetic field decreased the spacing of nano-sized Ag precipitates.

Acknowledgements

This work was supported by the National Natural Science Foundation of China (Nos. 51474066 and 51004038), the Research Fund for the Doctoral Program of Higher Education (No. 2012004211008), the 111 Project of China (No. B07015), US NSF (Cooperative Agreement No. 1157490), the State of Florida and the US Department of Energy.

References

1. Biselli C., *et al.* Acta mater., **44**, 493-504 (1996).
2. Qu L., *et al.* Mat. Sci. Eng. A, **528,** 2532-2537 (2001).
3. Zuo X. W., *et al.* Mat. Sci. Eng. A, **619**, 319-327 (2014).

Figures

1

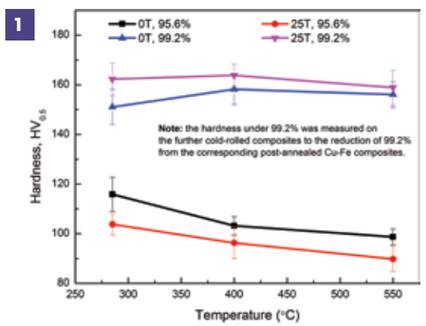

2

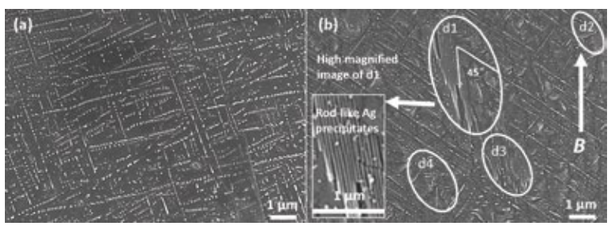

Fig. 1 The hardness of Cu-Fe composite with and without 25T high magnetic field.

Fig. 2 Nano precipitates of Ag in Cu28%Ag alloy (a) without a magnetic field, (b) with a 12 T high magnetic field

Magnet Technology

HTS cables hold a promise of enabling the next generation of large high-field high-current magnets for applications ranging from fusion, particle accelerators and other high-energy physics applications to research magnets that could be employed at the NHMFL. Cables based on the CORC concept have demonstrated practical features like tolerance to small bending radii, tolerance to axial and transverse forces and simple terminals, coupled with a rapid development to current density levels suitable for applications, as reported here, placing CORC cables amongst others at the forefront of a rapidly developing field with a healthy level of competition.

Record Current Density in High-Temperature Superconducting CORC Cables at 17 T

van der Laan, D.C. (Advanced Conductor Technologies and the University of Colorado); Trociewitz, U. ; Noyes, P.; Godeke, A. (FSU-NHMFL)

Introduction

The next generation of high-field superconducting magnets requires operating fields exceeding 20 T and that cannot be reached with low-temperature superconductors, such as NbTi or Nb_3Sn and high-temperature superconductors (HTS), such as $REBa_2Cu_3O_7$-δ (REBCO) coated conductors, are the only option. The measurements performed at the user facility of the NHMFL are in support of Conductor on Round Core (CORC) cable development [1-3]. This year we've reached a new record engineering current density J_e of 213 A/mm^2 at 4.2 K and 20 T (projected), making CORC cables the most promising HTS cables for high-field magnets.

Experimental

A 6 mm diameter CORC cable was wound from 50 superconducting tapes. The tapes were purchased from SuperPower and contained extra thin substrates of 38 μm thickness to help increase the cable current density. Figure 1a shows the cable wound in a 10-cm diameter loop onto the bottom part of the sample holder before testing at 17 T.

Results and Discussion

The CORC cable shown in Fig. 1a had a critical current I_c of 6,966 A in a field of 17 T. The superconducting transition is shown in Fig. 1b, together with a fit to determine I_c. The current density of the 6 mm diameter CORC cable at 17 T was 246 A/mm2. Based on the field dependence of I_c of CORC cables, Je at 20 T is expected to be a record 213 A/mm^2, almost twice the old record of 114 A/mm^2.

Conclusions

The results obtained at the user facility of the NHMFL in 2014 clearly show the potential of CORC cables for use in high-field magnets. The record engineering current density at 20 T of 213 A/mm^2 confirms that CORC cables are suitable for use in magnets ranging from large fusion magnets operating at high currents to accelerator magnets operating at very high current densities.

Acknowledgements

This work was supported in part by the U.S. Department of Energy, under award numbers DE-AI05-98OR22652, DE-SC0009545, and DE-SC0007660. A portion of this work was performed at the National High Magnetic Field Laboratory, which is supported by National Science Foundation Cooperative Agreement No. DMR-1157490, the State of Florida, and the U.S. Department of Energy.

References

1. van der Laan, D.C., *et al.*, Supercond. Sci. Technol. 24, 042001 (2011).
2. van der Laan, D.C., *et al.*, Supercond. Sci. Technol. 25, 014003 (2012).
3. van der Laan, D.C., *et al.*, Supercond. Sci. Technol. 26, 045005 (2013).

Figure 1

A

B

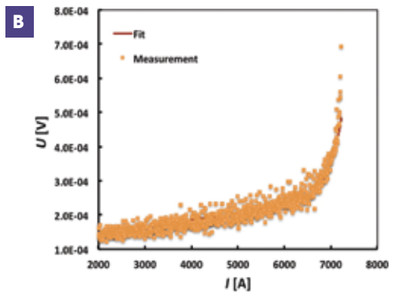

A) CORC cable wound at a diameter of 10 cm.
B) Voltage vs. current at 4.2 K the CORC cable at 17 T.

Magnet Technology

One of the great assets of high-temperature superconductors (HTS) is their ability to carry large current densities at temperatures well above 4 K, making them much more stable than their well-established low-temperature lower-field counterparts that can go into fault mode (quench) very easily. However, if an outer LTS coil accidentally quenches for example, it is necessary to protect the inner HTS coils by pro-actively quenching the HTS coils, resulting in a complex interaction between all coils. A comprehensive numerical code, benchmarked against experimental data that can model that complex process is a highly desirable tool for magnet design that is now becoming available.

Quench Analysis of the NHMFL 32 T All-superconducting Magnet

Gavrilin, A.V.; Hilton, D.K.; Markiewicz, W.D.; Noyes, P.D.; Weijers, H.W. (NHMFL)

Introduction

The development of a 32 T, 32 mm cold bore all-superconducting magnet with high temperature superconducting (HTS) REBCO inner high field coils (insert) is underway at the NHMFL (**Fig. 1**). In order to develop a quench protection system for the magnet, and especially that of its innovative 2-coil HTS insert, a sophisticated quench simulation is required. A quench code has been developed at the NHMFL to perform the necessary computer simulations of the magnet quench behavior in a number of case scenarios, which may take place in reality.

The quench code

The quench code, which development is practically completed, takes into account the actual layout and discrete structure of the REBCO coil windings with due regard for the measured current-carrying capacity and other properties of the REBCO tapes supplied by SuperPower, Inc. and used to wind the coils. Such a comprehensive quench analysis provides a detailed picture of the magnet quench behavior with a view to adjusting the quench protection system parameters and checking its serviceability. The active quench protection system of the insert includes tailor-made quench heaters to normalize the insert coils promptly in the event of quench. The heaters' operation is simulated appropriately by the quench code. Small HTS prototype coils (shown in Fig. 1) were tested to study the heaters efficiency and quench propagation process. A comparison of the measured voltages in the coils and other parameters with the calculation results is made to improve the quench code. **Fig. 2** shows an example of good agreement between the calculations and measurements. The final, full version of the quench code includes both the HTS insert and multi-coil LTS outsert with due regard for all relevant elements of the entire magnet quench protection system.

Acknowledgement

This work is supported by the U.S. National Science Foundation under Grants # DMR-0654118, DMR-1157490, DMR-0923070 and the State of Florida.

References

1. Gavrilin, A.V., *et al.*, presented at the Applied Superconductivity Conference of 2014, Charlotte, NC, August 2014

Figures

1

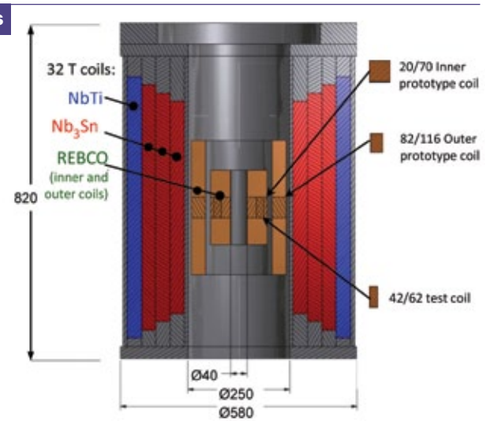

Cross-section of the 32T magnet with the LTS outsert (schematic) and the HTS insert REBCO coils. The prototype coils are shown, too. The LTS outsert is built by Oxford Instruments, Ltd

2

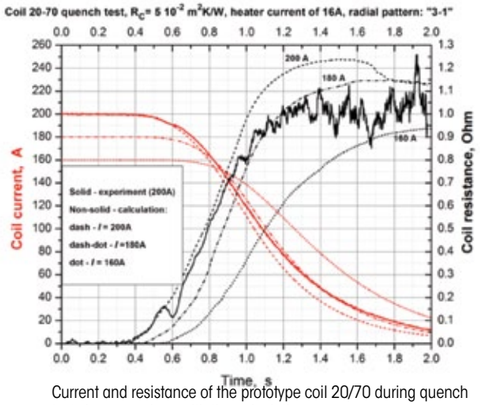

Current and resistance of the prototype coil 20/70 during quench tests in comparison with the calculations.

Magnet Technology

The availability of high magnetic fields and suitable measurement techniques at the NHMFL, coupled with access to both commercial and research grade HTS conductors from across the planet, allow a unique comparison of state-of-the-art high-field superconductors. This showcases both the differences between the various BSCCO and (RE)BCO conductors and the large increases in performance that make applications at 4 K, and at higher temperatures, that were unrealistic just a few years ago now viable.

Comparative Study of I_c(B, 4K) for (Re)BCO, Bi-2223, and Bi-2212 Conductors from Various Sources

Abraimov, D.; Jaroszynski, J.; Santos, M.; Jiang, J.; Francis, A.; McCallister, J.; Dickey, J.; Viouchkov, L.; Weijers, H.W.; Markiewicz, M.D.; Larbalestier, D.C. (NHMFL)

Introduction

Recent success in engineering pinning centers made it possible for commercially available IBAD- MOCVD (Re)BCO to exhibit very high J_c in fields beyond 30T in high Ic conductors suitable for making user magnets. Practical implementation of overpressure process (OP) to Bi-2212 round wires led to large J_c and I_c increases in a round, isotropic wire, making it a potentially competitive technology. In order to successfully design high-field, all-superconducting magnets, it is necessary to know the Ic and engineering current density (J_e) of the conductor in a broad range of fields and field orientations.

Experimental

We tested the I_c(B, 4.2K) dependencies up to 13.5T at fixed field orientations for the (Re)BCO tapes, overpressure processed round wire Bi-2212 made by Oxford Superconducting Technology and flat tape Sumitomo Bi-2223. I_c was measured on full width conductors at currents up to 1.4kA immersed in LHe. (Re)BCO samples were measured at BIIc and 18° to tape plane, the critical angle for the 32 T magnet now in construction. I_c(B) values were measured in increasing and decreasing fields to detect possible magnetic hysteresis indicative of damage or weakly coupled regions in the tape.

Results and Discussion

The J_e(B) dependencies for selected samples are shown in Fig.1. Magnetic flux is clearly trapped in the 2223 tape due to weak links, making J_c dependent on magnetic history, unlike 2212 and REBCO which do not show this weakness. Most conductors show a good power law fit $I_c \sim B^{-\alpha}$. Calculated α values are shown in **Table I**.

Conclusions

Among (Re)BCO tapes at BIIc the largest J_e values were detected for SuperPower and Bruker. Bi-conductors have smaller α values than (Re)BCO. Among the (Re)BCO conductors SuperOx tapes have the smallest α. Lower α generally means weaker vortex pinning. Bi-2212 round wires outperform (Re)BCO tapes in J_e at B>17T.

Acknowledgements

This work was supported in part by the U.S. National Science Foundation under Grant No. DMR-0654118, DMR-0923070 and the State of Florida.

Table 1

Manufacturer	Material	α at BIIc	α at 18°
SuperPower	(Re)BCO	0.67-0.76	0.7-0.9
SuNAM		0.6	0.69-0.68
SuperOx		0.54	0.59
Fujikura		0.64-0.69	0.7
AMSC		0.74	-
Bruker		0.88	-
Sumitomo	Bi-2223	0.16-0.18	-
OP processed	Bi-2212	0.26-0.33	

Figure 1

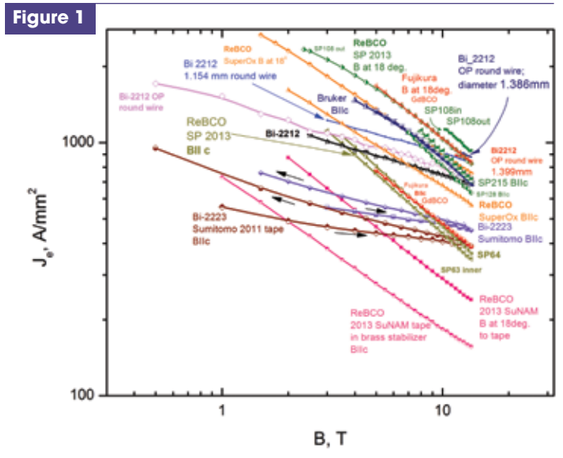

J_e(B) measured at LHe temperature for (Re)BCO tapes manufactured by Bruker, Fujikura, SuperPower Inc., SuperOx, SuNAM; Bi-2223 tape from Sumitomo, and variable diameter Bi-2212 round wire passed OP process. Arrors mark B direction.

Superconductivity – Applied

This is the very 1st experiment that has addressed the crucial question of whether the grain boundaries in very well made iron – based superconductors are intrinsic obstacles to supercurrent flow or whether they act as obstacles because the grain boundaries have markedly different compositions from the bulk or are indeed decorated by impurities. In principle this experiment can be done by analytical electron microscopy but in practice TEM samples are so thin that they are subject to atmospheric contamination in the preparation procedure. The advantage of atom probe microscopy is that the sample is ripped apart within the microscope itself and the data obtained is thus genuinely characteristic of the interior of the bulk sample. The experiment yielded the very important result that significant impurity contamination and significant non-stoichiometry existed in these high current density samples, making refinement of the processing therefore highly recommended.

Evidence for Extrinsic, Impurity Segregation at Grain Boundaries in High Current-Density K- and Co-Doped $BaFe_2As_2$ Superconductors

Weiss, J.D.; Hellstrom E.E.; Larbalestier D.C. (FSU, ASC); Kim, Y.; Seidman, D.N. (Northwestern University)

Introduction

The problem of supercurrent blocking at grain boundaries (GBs) of complex superconductors is central to their use, and understanding whether the blocking is intrinsic to their structure or induced by impurities or other artefacts is vital. We have shown that some Fe-based superconductors are very close to achieving the highly desirable critical current density of 10^5 A cm^{-2} in strong fields [1], but we do not yet know whether grain boundary blocking is an intrinsic or an extrinsic problem. Atom Probe Tomography (APT) enables high resolution, spatially resolved, mass spectrometry of GBs without the atmospheric contamination that is common in thin TEM samples [2]. Our hope was that APT would allow us characterize GBs in their native state so as to understand whether there were either strong non-stoichiometries at the GBs or impurities segregations. We found that the APT could indeed make such characterization.

Experimental

The samples were synthesized at the NHMFL's Applied Superconductivity Center (ASC) and then characterized using a 14 T superconducting vibrating sample magnetometer. Atom probe tomography was performed in David Seidman's group at the Northwestern University Center for Atom Probe Tomography (NUCAPT).

Results and Discussion

We turned to the APT because it allows a 3-D reconstruction of a bulk sample on an atom-by-atom basis, thus avoiding the strong degradation seen in thin samples made for analytical TEM. **Fig. 1** shows critical current density as a function of applied magnetic field for three bulk samples. APT data presented in **Fig. 2** shows that these high current density superconducting $BaFe_2As_2$ polycrystals have significant GB compositional variations *and* oxygen impurities, leading us to infer that the GBs act as extrinsic barriers for supercurrent flow. Since high field measurements revealed that samples with cleaner GBs carried significantly more current than samples with dirtier GBs, further refinements of our synthesis techniques are being carried out so as to make impurity-free GBs for use in future superconducting magnets.

Acknowledgements

We would like to thank J. Jiang, F. Kametani, and C. Tarantini for thoughtful discussions and W. L. Starch, V. S. Griffin, and B. H. Hainsey for technical support. The work at the National High Magnetic Field Laboratory was supported by NSF (No. DMR-1306785), the State of Florida, and by the NHMFL, which is supported by NSF (No. DMR-1157490). Atom-probe tomography measurements were performed at the NUCAPT and the LEAP tomograph was purchased and upgraded with funding from the National Science Foundation (NSF)-MRI (No. DMR-0420532) and Office of Naval Research (ONR)-DURIP (Nos. N00014-0400798, N00014-0610539, and N00014-0910781) programs. NUCAPT is a Shared Facility of the Materials Research Center of Northwestern University, supported by NSF-MRSEC Program (No. DMR-1121262). We are also grateful to the Initiative for Sustainability and Energy at Northwestern for upgrading NUCAPT's capabilities.

References

1. Weiss, J.D., *et al.*, Nature Materials, **11**, 682-685 (2012)
2. Kim, Y., *et al.*, Applied Physics Letters, **105**, 162604 (2014)

CONTINUED ON NEXT PAGE

Figures

1

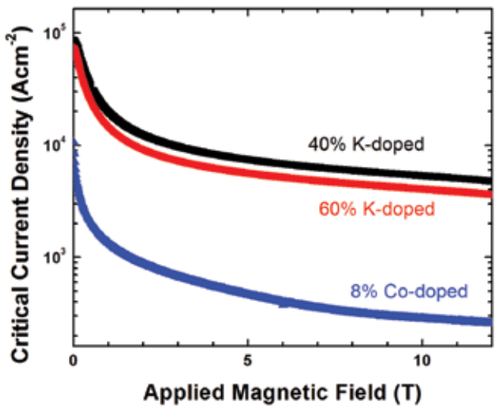

Critical current density as a function of applied magnetic field for three superconducting samples with different dopants and dopant levels at 4.2 K. [2]

2

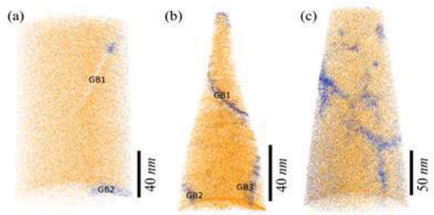

APT reconstructions of polycrystals showing oxygen (purple) segregating at grain boundaries in (a) 40% K-, (b) 60% K-, and (c) 8% Co-doped $BaFe_2As_2$ samples. [2]

Superconductivity – Applied

This work is a triumph of deductive failure analysis on the full-scale cables being manufactured for ITER which had been showing strong degradation under cyclic loading conditions and for explaining the very unusual behavior of some toroidal field cables which had avoided such degradation. The work showed how strong redistribution of the voids occurs under cyclic Lorenz force loading in these CICC and the strong reduction of the degradation in short twist pitch cables that effectively prevent single strand motions which can give rise to bend-strain-induced Nb3Sn filament fracture. Locking of the strands can also occur in longer twist pitch cables when very rough Cr plate is present on the strand surface, again preventing single strand motions that can lead to filament fracture. This work was both elegant itself and of significant impact for the ITER project.

Published: Sanabria C, Lee P J, Starch W, Blum T, Devred A, Jewell M C, Pong I, Martovetsky N and Larbalestier D C 2015 Metallographic autopsies of full-scale ITER prototype cable-in-conduit conductors after full testing in SULTAN: 1. The mechanical role of copper strands in a CICC *Superconductor Science and Technology* **28** 085005

Metallographic Analysis of SULTAN-Tested ITER Cable-in-Conduit-Conductors

Lee. P.J.; Sanabria, C.; Blum, T.; Starch, W.; Larbalestier, D.C. (FSU, Applied Superconductivity Center); Devred, A.; Mitchell, N. (ITER International Organization); Martovetsky, N. (ORNL-US ITER)

Introduction

In the International Thermonuclear Experimental Reactor (ITER) being built in Cadarache in the south of France, the Central Solenoid (CS) coils are required to provide a 13 T peak magnetic field and maintain specified critical current performance over 30,000 plasma pulses; the severe cyclic Lorentz force loading of the brittle Nb_3Sn superconductor can result in degradation of the cable-in-conduit-conductor (CICC) and loss of magnet performance. For this reason prototype cables have been tested electromagnetically and thermally in the SULTAN facility at CRPP Villigen CH. Key CICCs were sent to the Applied Superconductivity Center (ASC) at NHMFL for comprehensive macrostructural and microstructural analysis.

Experimental

Typically, full SULTAN sample legs (~3.5m) were supplied to the NHMFL which allowed us to compare parts of the CICC that experienced full Lorentz force loading ("HFZ") with regions subjected to less than 1 T ("LFZ") where Lorentz forces were small [1]. Both CS Toroidal Field (TF) CICCs were exam-

ined. Sections were cut from the full lengths and either disassembled for individual component analysis or impregnated with epoxy resin to fix the strands in place for cross-sectional analysis. Fully impregnated strand cross-sections were metallographically polished and then imaged using the Scanning Laser Confocal Microscope (SLCM) facility at ASC. The integrated digital stage of the SLCM allows us to create massive high resolution mosaics of conductor cross-sections with sufficient resolution to accurately determine the locations and sizes of all conductor components, allowing us to quantify their movement due to the Lorentz force loading [1]. In addition extracted strands of the disassembled sections were metallographically polished in longitudinal cross-section and analyzed for the level of Nb_3Sn filament breakage caused by the loading using high resolution FESEM images taken along long lengths of extracted strands [1].

Results and Discussion

ASC fully analyzed six CS prototypes and two TF prototypes after their full tests at SULTAN. The CS [1] analyses showed that severe filament cracking during cyclic testing is usually associated with excessive bending of the strands around strand cross-over pivot points. In response to such analyses, a redesign of the CS cables was made to minimize such movement resulted in cables without degradation.[2] However, although the redesign approach was successful, further study of a TF CICC with very rough Cr plated wire surfaces, which showed no degradation despite having damaged strands **(Fig. 1)**, suggests that controlling strand-to-strand friction may provide an alternative method for reducing CICC degradation.[3] In this case the rough surface locked the strands effectively, inhibiting motion under the cyclic Lorentz loading of the SULTAN test.

Conclusions

Post-mortem analysis of SULTAN-tested ITER CICCs has provided an essential tool for the successful conclusion of the ITER cable development program and has shown the possibility of decreasing cable degradation through the enhancement of inter-strand friction.

Acknowledgements

A portion of this work was performed at the National High Magnetic Field Laboratory, which is supported by National Science Foundation Cooperative Agreement No. DMR-1157490, the State of Florida, and the U.S. Department of Energy. The CICCs were provided by courtesy of Pierluigi Bruzzone (CRPP) with agreement from JAEA, ITER RF and US-ITER. This work was primarily supported by the ITER Organization under purchase order ITER/CT/11/4300000511, US –ITER under contract 6400011187, and the US Department of Energy Office of Fusion Energy Sciences under award DE-FG02-06ER54881.

References

1. C. Sanabria *et al., Superconductor Science and Technology* **28** 085005 (2015).
2. A. Devred *et al., Superconductor Science and Technology* **27**, 044001 (2014).
3. C. Sanabria et al. Manuscript in preparation.

Figures

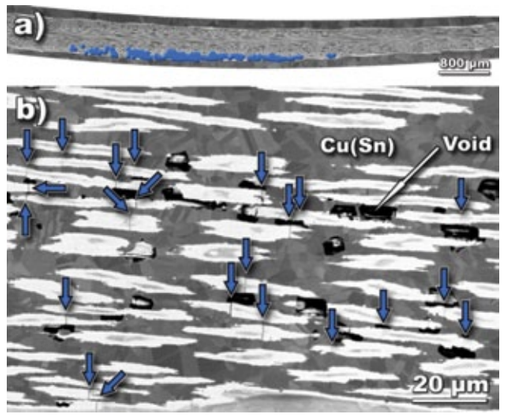

(A) Longitudinal cross-section of a strand extracted from the HFZ of a TF CICC that showed no T_{cs} degradation under cyclic loading. Filament fractures are highlighted by blue artificial markers. **(B)** A detail showing some of the filament fractures.

Superconductivity – Applied

This paper describes the world record trapped field of 17.6 T, the largest reported to date, in a stack of two silver-doped GdBCO superconducting bulk samples, each 25 mm in diameter, fabricated by top-seeded melt growth and reinforced with shrink-fit stainless steel. This sample preparation technique has the advantage of being relatively straightforward and inexpensive to implement, and offers the prospect of easy access to portable, high magnetic fields without any requirement for a sustaining current source.

A Trapped Field of 17.6 T in a $GdBa_2Cu_3O_7$ Bulk Superconductor

Durrell, J.H.; Dennis A.R.; Ainslie, M.D.; Palmer, K.G.B.; Shi Y.-H.; Campbell, A.M.; Cardwell, D.A. (University of Cambridge); Jaroszynski J.; Hellstrom, E. (NHMFL); Hull, J.; Strasik, M.(The Boeing Company)

Introduction

Bulk superconductors fabricated from $GdBa_2Cu_3O_7$ have potential applications as replacements for permanent magnets where fields far in excess of the ~1T achievable with NdFeB are required. The larger the field that can be trapped the more compelling the technical case since bulk superconductors do require cryogenic cooling. For many years the peak magnetic field that can be trapped in a bulk superconductor has been the 17.2 T result achieved by Tomita *et al.* [1]. The limiting factor to the high field performance of such bulks is the tensile strength of the superconductor with the strain scaling as B^2 [2]. As the superconductors in question are brittle ceramics this is a challenging materials problem.

Experimental

To achieve high trapped fields mechanical reinforcement of the sample is required. Two classes of techniques have been exploited, steel banding [2] and reinforcement with carbon fibre epoxy [1]. With steel banding the pre-stress introduced by differential thermal expansion is relatively modest. We employed a "shrink fitting" method to address this. We carefully machined perfectly cylindrical bulks and prepared slightly under size stainless steel (304L) rings. When heated the rings could be slipped over the bulks. As the rings cooled they contracted applying pre-stress.

The actual measurement itself is quite simple. A pair of reinforced superconducting bulks are sandwiched around hall effect magnetic field sensors. The bulks are then cooled in a large magnetic field, in these experiments provided by the SCM-2 system at the NHMFL DC Field facility, to around 25 K and subsequently the external field is slowly removed. The remnant field trapped in the bulks can then be measured.

Results and Discussion

The experiment described in the previous section resulted in the 17.6 T trapped field shown in Fig.1 and fully described by the present authors in an article published in Superconductor Science and Technology [3]. We suspect that, since the steel we are using is near its yield point, we are near the limit of trapped field performance obtainable with this technique. Attempts to trap larger fields using the maximum 18 T field available in SCM-2 resulted in the failure of the samples.

Conclusions

Stainless steel band reinforcement combined with a "heat-shrinking" technique is a relatively straightforward way to reinforce superconducting bulks. We believe this technique has promise given that using it we have been able achieve the largest trapped magnetic field yet reported in a bulk superconductor.

Acknowledgements

A portion of this work was performed at the National High Magnetic Field Laboratory, which is supported by National Science Foundation Cooperative Agreement No. DMR-1157490, the State of Florida, and the U.S. Department of Energy. This work was additionally supported by The Boeing Company and by the Engineering and Physical Sciences Research Council (Grant number EP/K02910X/1).

References

1. Tomita M. *et al.*, Nature, **421**, 517-520 (2003).
2. Fuchs G. *et al.*, Applied Physics Letters, **76,** 2107-2109 (2000).
3. Durrell J. H. *et al.*, Superconductor Science and Technology, **27,** 082001 (2014)

Figure 1

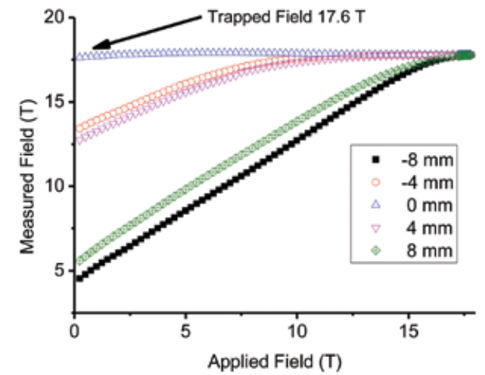

The field measured at the interface between the two samples in the stack by an array of Hall probes (distances indicated are from the centre of the sample) as the magnetising field was ramped down. [Reproduced from [1] under the CC-BY license]

MagLab's Worldwide User Community

In 2014, the MagLab worked with more than 1,442 scientists from 280 institutions across the globe.

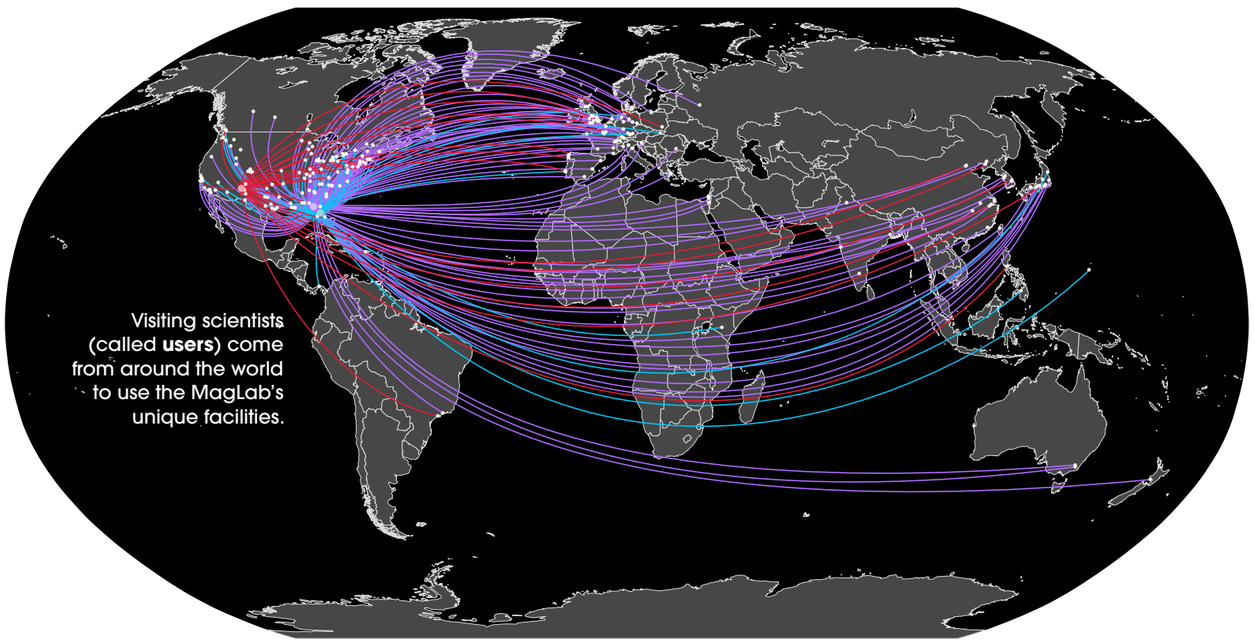

Aarhus University
Ben-Gurion University of the Negev
Centre National de la Recherche Scientifique (CNRS)
CNR-Istituto Nanoscienze
Commissariat à l'Energie Atomique
Dresden High Magnetic Field Laboratory
Environment Canada
École Polytechnique (EPFL)
ESPCI ParisTech
ETH Zurich
Ewha Womans University
FOM Institute AMOLF
Fudan University
Gdansk University of Technology
Geoscience Australia
German Cancer Research Center (DKFZ)
Haldor Topsoe
Hefei National Laboratory for Physical Sciences
Hosei University
Huazhong University of Science & Technology
Imperial College London
IFP Energies Nouvelles
Institut Materiaux Microelectronique Nanosciences De Provence
Institute of Physics, Chinese Academy of Sciences
Instituto Superior Técnico
International Potato Center
Ioffe Physical-Technical Institute
Japan Agency for Marine Earth Science & Technology (JAMSTEC)
Jozef Stefan Institute
Kemwell Biopharma Pvt Ltd
Korea Basic Science Institute
Kyoto University
Kyungpook National University
Leibniz Institute for Solid State & Materials Research (IFD Dresden)
Laboratoire National des Champs Magnétiques Intenses, Grenoble
Laboratoire National des Champs Magnétiques Intenses, Toulouse
Massey University/ University of New Zealand
Max Planck Institute for Solid State Research
Max Planck Institute of Psychiatry
McGill University
Mindanao State University-Iligan Institute of Technology
Nagoya University
National & Kapodistrian University of Athens
National Chung-Hsing University
National Institute for Materials Science, Japan
National Taiwan University
National University of Science & Technology (MISiS)
Nexans SuperConductors
Northeastern University
Okayama University
Osaka Prefecture University
Otto-von-Guericke University
P.J. Safarik University
Panjab University
Paul Scherrer Institute
Petrobras
Philipps University Marburg
Polytechnic University of Valencia
POSTECH
Queen's University
Reliance Oil
RIKEN
Russian Academy of Science (RAS)
Schlumberger
Seoul National University
Shizuoka University
Smithsonian Tropical Research Institute
Sungkyunkwan University
Tel Aviv University
Tsinghua University
The Australian National University
The University of Warwick
Tohoku University
Tokyo Institute of Technology
Technische Universität München
University College London
Universidad de Granada
Universidade de Lisboa
Universidade de Sao Paulo
Università di Pavia
Universitat de València
Universitat Rovira i Virgili
Universite de Nantes
Université de Sherbrooke
Université des Sciences et Technologies de Lille
Université Paris Sud XI
University Bern
University Bremen
University of Athens
University of Augsburg
University of Birmingham
University of Bristol
University of British Columbia
University of Bucharest
University of Calcutta, India
University of Cambridge
University of Coruna
UniVersity of Edinburgh
University of Ferrara
University of Geneva
University of Glasgow
University of Guelph
University of Manitoba
University of Oxford
University of Rzeszow
University of Santiago de Compostela
University of Science and Technology of China
University of Toronto
University of Windsor
University of Winnipeg
University of Wroclaw
Weizmann Institute of Science
Wuhan Institute of Physics & Mathematics, Chinese Academy of Sciences
Xiamen University
Zhejiang University

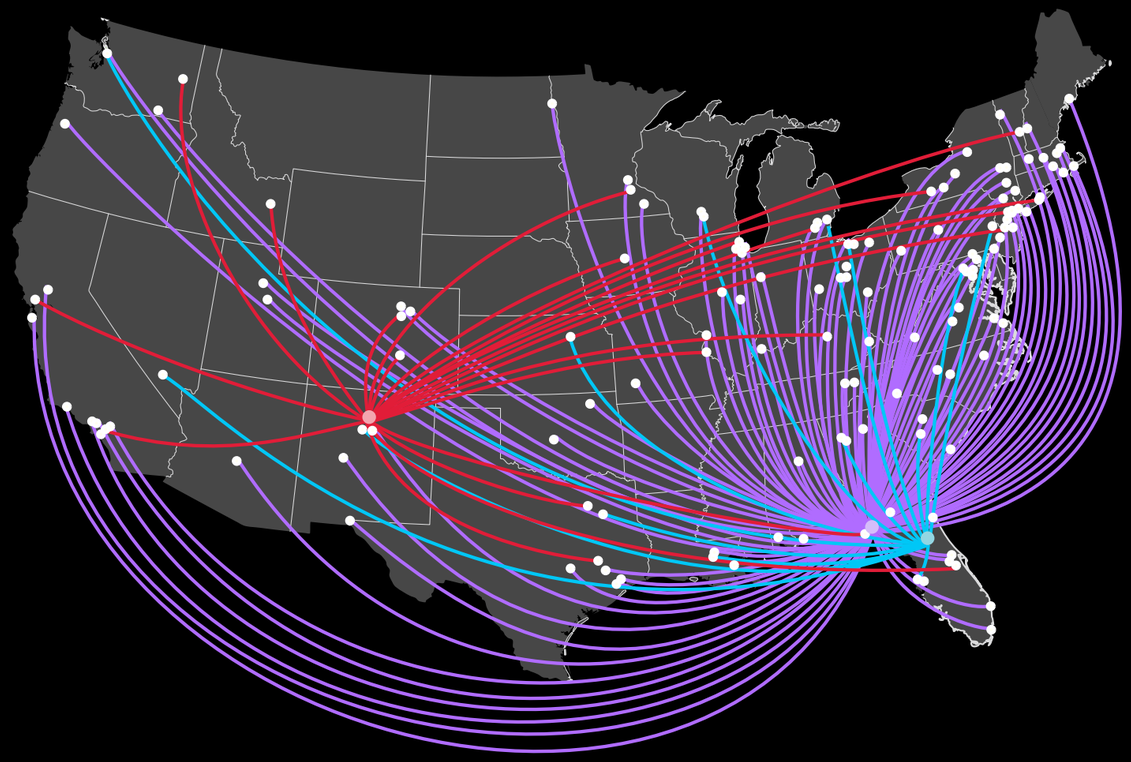

Advanced Conductor Technologies
Air Force Research Lab
Alfred University
Ames Laboratory
Applied Materials
Argonne National Laboratory
Arizona State University
Baker Hughes Inc.
Bard College
Beckman Institute
Bell Labs
Brandeis University
Brigham Young University
Brookhaven National Laboratory
Brown University
Bruker Biospin
California Institute of Technology
Carleton College
Case Western Reserve University
Christopher Newport University
City College of New York
Claflin University
Colorado School of Mines
Columbia University
ConocoPhillips Company
Cornell University
Corning Incorporated
Dana-Farber Cancer Institute
Dartmouth Medical School
Duke University
East Carolina University
Eastern Washington University
Florado Entek, Inc.
Florida State University
Food and Drug Administration
Future Fuels Institute
Gardner-Webb University
Georgia Institute of Technology
Georgia State University
Hamilton College
Harvard University
HK Petroleum, LTD
IBM T. J. Watson Research Center
Idaho National Laboratory
Illinois Wesleyan University
Institute for Corrosion and Multiphase Technology at Ohio University
Iowa State University
Johns Hopkins University
Kansas State University
Kent State University
Lake Shore Cryotronics
Lawrence Berkeley National Laboratory
Los Alamos National Laboratory
Louisiana State University
Massachusetts Institute of Technology
Maxim Integrated
Mayo Clinic College of Medicine
Mayo Clinic Jacksonville
MD Anderson Cancer Center
Medical University of South Carolina
Merck Research Laboratories
Missouri State University
Nalco Energy Services
NASA Ames Research Center
National Institute of Diabetes & Digestive & Kidney Diseases
The National Institutes of Health
National Institute of Standards & Technology
National Renewable Energy Lab
NAVSEA Division Newport
New Mexico Tech
North Carolina State University
Northeastern University
Northwestern University
Oak Ridge National Laboratory
Oberlin College
Occidental College
Ohio State University
Ohio University Medical Center
Old Dominion University
Oregon State University
Out of the Fog Research
Pacific Northwest National Laboratory
Pennsylvania State University
Prairie View A&M University
Princeton University
Purdue University
Queens College of CUNY
Ramapo College of New Jersey
Rensselaer Polytechnic Institute
Rice University
Roosevelt University
Rutgers University
Saint Louis University
Sandia National Laboratories
Scripps Research Institute - Florida
Shell Global Solutions (US) Inc.
Smith College
Stanford University
Stony Brook University
Texas A&M University
Thermo Fisher Scientific
Transportation Technology Center
Tufts University
U.S. Geological Survey
UC Davis
UC Santa Barbara
United States Department of Agriculture
University at Albany, SUNY
University of Alabama
University of Alabama at Birmingham
University of Alaska Anchorage
University of California, Irvine
University of California, Berkeley
University of California, Davis
University of California, Los Angeles
University of California, Riverside
University of Central Florida
University of Chicago
University of Colorado
University of Delaware
University of Florida
University of Georgia
University of Guam
University of Houston
University of Illinois at Chicago
University of Illinois at Urbana-Champaign
University of Kentucky
University of Maryland
University of Miami
University of Michigan
University of Minnestoa
University of Missouri
University of Nevada at Las Vegas
University of New Orleans
University of North Dakota
University of North Florida
University of Notre Dame
University of Oklahoma
University of Pennsylvania
University of Pikeville
University of Pittsburgh
University of Puerto Rico
University of South Alabama
University of South Carolina
University of South Florida
University of Southern Indiana
University of Tampa
University of Tennessee
University of Texas at Austin
University of Texas at Dallas
University of Texas at El Paso
University of Texas Health and Science Center
University of Texas-Houston Medical School
University of Utah
University of Vermont
University of Virginia
University of Washington
University of West Florida
University of Wisconsin-Madison
Valdosta State University
Virginia Tech.
Washington University in St. Louis
Wayne State University
Woods Hole Oceanographic Institution
Worcester Polytechnic Institute

NEWS BRIEFS

AROUND THE LAB

10th Mass Spec Conference

The **biennial North American Fourier Transform Mass Spectrometry Conference** was held in Key West, FL, April 12-15, 2015. Attended by 70 participants, the Conference featured 22 invited talks and 28 posters, concluding with a plenary presentation by Dr. Jean Futrell (PNNL), "Six Decades of Invention in Sixty Minutes." This year's Conference also introduced the first results from NHMFL's 21 T Fourier transform ion cyclotron resonance mass spectrometer, including mass resolving power of 2,000,000 for bovince serum albumin (66 kDalton).

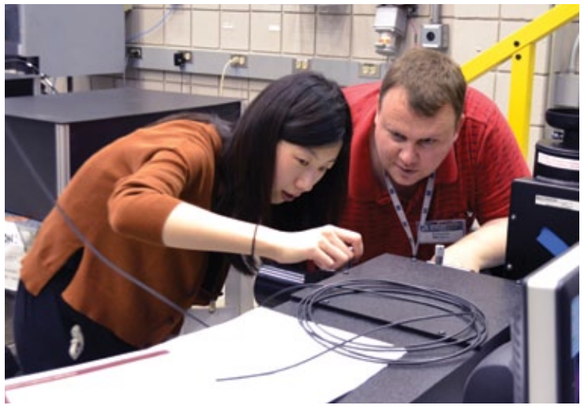

Summer School Around the Lab

This year, another spectacular group of **User Summer School** participants trekked to the MagLab's headquarters for a week of expert talks, hands-on tutorials and fun. Twenty-eight students from around the world gained experience with noise suppression techniques, measurements at ultra-low temperatures, infrared and terahertz spectroscopy, and the nuts and bolts of data acquisition. This year's class featured students from Iowa State, Rice University, University of Tennessee, Carnegie Mellon, University of Wisconsin, University of Michigan, University of Florida, Florida State University, UC Santa Barbara, University of Edinburgh-Scotland and the Max-Planck Institute in Dresden, Germany. For more information on next year's User Summer School, visit **NationalMagLab.org/news-events/events/for-scientists/user-summer-school.**

Middle school students have also been playing and learning at the **MagLab Summer Camp.** Two weeklong sessions were held in June 2015. More than 30 students participated in STEM activities including calculating the acceleration of a rollercoaster, building their own speakers and competing in a robotic soccer tournament. The Summer Camp is coordinated by the MagLab's educational arm, the Center for Integrating Research and Learning, and provides children a chance to have fun while investigating scientifically. For more information on next year's camp, visit **NationalMagLab.org/education/k12-students/summer-camps.**

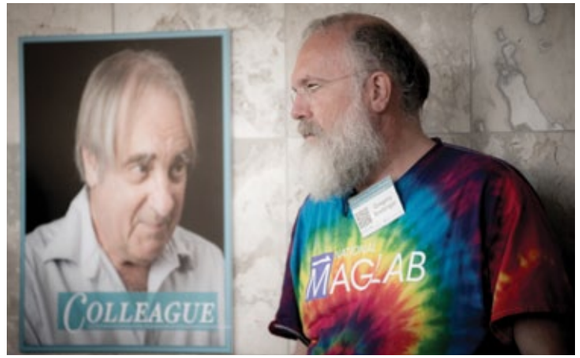

Memorial Symposium

In May 2015, 80 attendees came to the National MagLab to celebrate the life and legacy of Jim Brooks. Brooks, a professor and Chairman of the Florida State University Physics Department, passed away on September 27, 2014. As one of the early experimental faculty members to join the MagLab in Tallahassee, he carried out prolific research with colleagues both in the U.S. and around the world. During this one-day event, colleagues and friends gathered to share research performed in collaboration with Dr. Brooks and memories from their life experiences. Known for his passion for science and mentorship, a graduate student award in materials science and engineering has been established in his honor. To donate, visit **http://ow.ly/m26kn.**

ICR Facility Director Named

Chris Hendrickson has been named director of the MagLab's Ion Cyclotron Resonance Facility. Nearly 150 scientists a year travel from across the globe to access the facility's world-record magnets — and the world-class expertise that goes with them — located in Tallahassee, Florida.

"Chris Hendrickson is the leading world authority on FT-ICR MS instrumentation, and is the chief designer for the MagLab's 21 tesla FT-ICR mass spectrometer, which has already set new benchmarks for mass resolution and accuracy," said Alan Marshall, chief scientist for ICR at the lab and co-inventor of the field.

The ICR facility is making final modifications to this new 21 T system, which will become available for scientists, and groundbreaking discoveries, later this year.

NEWS BRIEFS CONTINUED

MARK YOUR CALENDAR

PPHMF Registration Open Now

Registration is now open for the Physical Phenomena at High Magnetic Fields (PPHMF) Conference on January 6 – 10, 2016. This conference will bring experts from around the world to the National High Magnetic Field Laboratory's headquarters in Tallahassee, Florida to discuss recent advances in areas of science and technology in which high magnetic fields plan — or could play — an important role. Register now or learn more about the conference at **NationalMagLab.org/PPHMF**

44th Southeast Magnetic Resonance Conference (SEMRC)

Registration is now open for SEMRC, which will be held October 9 – 11 at the Plaza Report and Spa in Daytona Beach, Florida. This conference brings together leading scientists to exchange ideas, share new research, explore applications and techniques, and discuss the latest developments in NMR, EPR and MRI. For more information or to register, please visit **NationalMagLab.org/semrc**

HONORS & AWARDS

World Record

A MagLab-made magnet made a loud splash this summer when it broke the world record for an all-superconducting magnet.

Built with both traditional and novel superconducting materials, the magnet reached a field of 27 teslas on June 5 in a test that exceeded designers' expectations. The magnet is a smaller version of an even more powerful magnet due for completion next year — a 32 tesla all-superconducting magnet that will be substantially stronger than any such magnet built to date.

The **27 T** record field was 3.5 T stronger than the strongest superconducting magnet currently in operation (in Lyon, France) and 1 T stronger than a superconducting test magnet built earlier this year in South Korea. The new record magnet embodies the collaborative nature of the project which features YBCO tape constructed by SuperPower Inc, LTS coils made by Oxford Instruments and HTS coils and other key technologies developed and constructed at the MagLab.

The completed 32 T magnet is projected to be ready for scientists in the first half of 2016.

MagLab-er Named FSU Distinguished University Scholar

Research Faculty member of the lab's Magnet Science & Technology department, **Ke Han**, was presented with the FSU Distinguished University Scholar Award during an annual Faculty Award Dinner on April 27th. This award recognizes Han's outstanding performance and longstanding record of research.

Multiple Awards for ICR Undergrad

Tessa E. Bartges, a Florida State University undergraduate and research assistant in the MagLab's Ion Cyclotron Resonance Facility, was awarded the Charles A. and Louis I. Brautlecht Scholarship from the FSU Department of Chemistry & Biochemistry. Bartges also received the DAAD RISE fellowship to conduct scientific research this summer in Germany.

MAGLAB REPORTS

1800 E. Paul Dirac Drive
Tallahassee, FL 32310

Non-profit
Organization
U.S. Postage
PAID
Tallahassee, FL
Permit No. 55

Keep up with new discoveries, upcoming events and exclusive articles on our new website and social media:

NationalMagLab.org

@NationalMagLab

The National MagLab is supported by the National Science Foundation and the State of Florida.